1

WL-TM-91-303~~-FIMG~~

The Effects on Aerodynamic Performance of Designing Supersonic Wings for Laminar Flow Control

Carl P. Tilmann
WL/FIMG

January 1991

Approved for Public Release : Distribution Unlimited

Flight Dynamics Directorate
Wright Laboratory
Wright-Patterson Air Force Base, OH 45433-6553

Foreward

The research documented in this report was started by the author while under a graduate stipend at the George Washington University / NASA Langley Joint Institute for Advancement of Flight Sciences. Mr. Samuel Dollyhigh, Head of the Vehicle Integration Branch of the Advanced Vehicles Division, provided critical guidance during this peroid. The analysis and report were completed at the High Speed Aero Performance Branch, Aeromechanics Division, Flight Dynamics Directorate of the Wright Laboratory at Wright-Patterson Air Force Base, Ohio. The author is indebted to the High Speed Aero Performance Branch for allowing him the time to complete and document this effort.

Carl P. Tilmann
Aerospace Engineer
Flight Performance Group

David T. Johnson

David T. Johnson
Technical Manager
Flight Performance Group
High Speed Aero Performance Branch

Valentine Dahlem

Valentine Dahlem
Chief
High Speed Aero Performance Branch
Aeromechanics Division

Report Documentation Page

1. Agency Use Only (leave blank)

2. Report Date
30 January 1991

3. Report Type and Dates Covered
Interim Report

4. Title and Subtitle
The Effects on Aerodynamic Performance of Designing Supersonic Wings for Laminar Flow Control

5. Funding Numbers
WU 24040797 In-house

6. Author(s)
Carl P. Tilmann

7. Performing Organization Name(s) and Address(es)
WL/FIMG
Wright-Patterson Air Force Base, OH 45433-6553

8. Performing Organization Report No.
WL-TM-91-303

9. Sponsoring / Monitoring Agency Name(s) and Address(es)
Same as Block 7.

10. Sponsoring / Monitoring Agency Report No.
WL-TM-91-303

11. Supplementary Notes

12a. Distribution / Availability Statement
Approved for Public Release : Distribution Unlimited

12b. Distribution Code

This method

13. Abstract *(maximum 200 words)*

A preliminary technique has been developed for the design of wings to be used with supersonic hybrid laminar flow control systems. This technique has been used to evaluate the effects on aerodynamic performance of designing supersonic wings for laminar flow control. In this design method, a wing is cambered such that it produces an upper-surface streamwise pressure distribution which is favorable for use in a hybrid laminar flow control (HLFC) system, while maintaining a spanwise lifting distribution which will minimize drag-due-to-lift. An existing linear-theory computer program is used to calculate the wing camber definition that produces a desired pressure distribution on the upper surface of the given wing with a specified thickness profile. In an attempt to quantify this design method's impact on performance, it was applied to an array of arrow-wings varying in aspect ratio and taper ratio. Each of the wing planforms was then camber-optimized for minimum cruise drag-due-to-lift using current preliminary wing design ~~methods,~~ which optimize the wing's camber or lifting load distribution without regard to the boundary layer type (which is generally assumed to be fully turbulent). The total drag of each wing was then estimated by the superposition of zero-lift wave drag, skin friction drag, and drag-due-to-lift. The true effectiveness of laminar flow control wings could then be evaluated by weighing the benefit of the reduced friction drag against the penalty of increased drag-due-to-lift which would be displayed by a wing designed for a laminar flow control system. The primary goal of this study was to quantify these differences and determine their impact on the potential aerodynamic benefits of HLFC wings.

14. Subject Terms
Laminar Flow Control, Supersonic Laminar Flow, Supersonic Wing Design, Supersonic Aircraft Design.

15. Number of Pages
80

16. Price Code

17. Security Classification of Report
Unclassified

18. Security Classification of page
Unclassified

19. Security Classification of Abstract
Unclassified

20. Limitation of Abstract
Unlimited

NSN 7540-01-280-5500

Standard Form 298 (Rev. 2-89)
Prescribed by ANSI Std. Z39-18
298-102

Contents

List of Tables v

List of Figures vi

List of Symbols viii

1 Introduction 1

2 Prelimenary Evaluation of Supersonic Wings 3
- 2.1 Zero-Lift Wave Drag . . . 3
  - 2.1.1 Far-Field Wave Drag . . . 3
  - 2.1.2 Near-Field Wave Drag . . . 4
- 2.2 Drag-Due-to-Lift . . . 5
- 2.3 Friction Drag . . . 6
  - 2.3.1 Turbulent Boundary Layer Friction Drag . . . 7
  - 2.3.2 Laminar Boundary Layer Friction Drag . . . 9
  - 2.3.3 Mixed Boundary Layer Friction Drag . . . 10
- 2.4 Validation of Pressure Distribution Estimates . . . 11

3 Designing Wings for Minimum Drag-Due-to-Lift 13
- 3.1 Lifting Load Optimization Theory . . . 13
- 3.2 Definition of the Camber Surface . . . 16
- 3.3 Application to a Sample Wing . . . 17

4 An Inverse Design Method for HLFC Wings 19
- 4.1 Design Goals . . . 19

4.2 Inverse Design Procedure . . . 20
  4.2.1 Determination of the Flat-Roof-Top Loading Distribution . . . 20
  4.2.2 Determination of the Span- Optimized Loading and Camber Surface . . . 22
  4.2.3 Determination of the Flat-Roof-Top Camber Surface . . . 23
  4.2.4 Total Camber Surface . . . 23
  4.2.5 Summary of Inverse Design Procedure for HLFC Wings . . . 24
4.3 Application to a Sample Wing . . . 25

5 Parametric Study of the Wing Design Methods **28**
5.1 Zero Lift Wave Drag . . . 28
5.2 Skin Friction Drag . . . 30
  5.2.1 C_{D_f} Based on Critical $\frac{x}{c}$ . . . 31
  5.2.2 C_{D_f} Based on Critical Re . . . 32
5.3 Drag-Due-to-Lift . . . 33
5.4 Total Drag . . . 34

6 Concluding Remarks **36**

7 References **38**

List of Tables

3.1 Candidate Loadings Considered in Wing Designs 14

4.1 Lift Contributions of Surface Portions for Wings in Parametric Study 26

5.1 Dimensions of Planforms in Parametric Study 29

5.2 Drag-Due-to-Lift at Cruise of Wings in Parametric Study 34

List of Figures

2.1 Superposition Method of Drag Analysis 41

2.2 Far-Field Wave Drag Calculations 42

2.3 Mach Box Computational Grid for Supersonic Aerodynamics 43

2.4 Theory of Attainable Vortex Thrust 44

2.5 Mixed Boundary Layer Schematic 44

2.6 Test Wing Planform Description 45

2.7 Airfoil Sections for Test Wing 46

2.8 Comparison of Theoretical and Experimental Pressure Distributions . . 47

3.1 NACA 64-004 Airfoil Thickness Profile 54

3.2 Baseline Wing Designed for Minimum Drag-Due-to-Lift 55

3.3 Pressure Distribution on Baseline Wing Designed for Minimum Drag-Due-to-Lift 56

3.4 Baseline Wing Designed for Minimum Drag-Due-to-Lift with Modified Root 57

3.5 Airfoil Sections for Baseline Wing Designed for Minimum D-D-T-L . . 58

3.6 Pressure Distribution on Baseline Minimum D-D-T-L Wing with Modified Root 59

4.1 Lifting Pressure Distribution on Flat-Roof-Top Camber Surface 60

4.2 Lifting Pressure Distribution on Span-Optimized Camber Surface . . . 60

4.3 Pressure Distributions on Inverse Design Portions and on the Final Flat-Roof-Top Wing 61

4.4 Pressure Distribution on Uncambered Baseline Wing at Design Lift . . 62

4.5 Pressure Distribution on Span Optimized Portion of Baseline Wing . . 63

4.6 Pressure Distribution on Flat-Roof-Top Portion of Baseline Wing . . . 64

4.7 Baseline Wing Designed by Inverse HLFC Method 65

4.8 Flat-Roof-Top Baseline Wing with Spanwise Loading Distribution Optimized 66

4.9 Inverse HLFC Design of Baseline Wing After Root Modification 67

4.10 Airfoil Sections for Baseline Inverse HLFC Design 68

4.11 Pressure Distribution on Baseline HLFC Wing with Root Section Rotated 69

5.1 Set of Planforms Used in Parametric Study 70

5.2 Effect of AR and taper ratio on Near-Field Wave Drag at Cruise 71

5.3 Effect of AR and taper ratio on Far-Field Wave Drag at Cruise 71

5.4 Effect of Laminar Flow on Friction Drag of Baseline Wing 72

5.5 Effect of AR and taper ratio on Skin Friction Drag of Fully Turbulent Wing 73

5.6 Effect of AR and taper ratio on Skin Frictione Drag of Fully Laminar Wing 73

5.7 Effect of Turbulent Wedge at Root on Friction Drag 74

5.8 Effect of Critical Reynolds Number on Friction Drag of Baseline Wing 75

5.9 Effect of Critical Reynolds Number Assumption on Calculated Skin Friction Drag 76

5.10 Near-Field Wave Drag Plus Drag-Due-to-Lift on Baseline Planform . . 77

5.11 Cruise Drag-Due-to-Lift of Parametric Wings 78

5.12 Total Drag of Parametric Wings 79

5.13 Total Drag Benefit of HLFC Wings 80

List of Symbols

AR	wing aspect ratio = $\frac{b^2}{S}$
b	wing span, ft
c or c_{sw}	streamwise local chord length, ft
$\bar{c}$	mean aerodynamic chord, ft
c_a	section axial force coefficient
C_D	drag coefficient = $\frac{D}{qS}$
C_{D_0}	zero lift drag coefficient
C_{D_f}	skin friction drag coefficient = $C_f \frac{S_{wet}}{S_{ref}}$
C_{D_i}	lift induced drag coefficient
C_{D_w}	wave drag coefficient
c_f	local skin-friction coefficient
C_f	average skin-friction coefficient
c_ℓ	section lift force coefficient
C_L	lift coefficient = $\frac{L}{qS}$
C_M	pitching moment coefficient = $\frac{M}{qS\bar{c}}$
c_n	section normal force coefficient
C_N	normal force coefficient
C_p	wing surface pressure coefficient
C_{p_l}	lower surface pressure coefficient
C_{p_u}	upper surface pressure coefficient
c_r	wing chord at root, ft
c_t	wing chord at tip, ft
C_t	section theoretical leading-edge thrust coefficient
h	altitude, ft
K_T	attainable thrust factor
k	constant of proportionality
L/D	lift to drag ratio
M	Mach number
M_∞	free stream Mach number
q	dynamic pressure = $\frac{1}{2}\rho V^2$, $\frac{lb}{ft^2}$
r	one-dimensional adiabatic wall recovery factor
$\frac{r}{c}$	leading edge radius ratio
R	Reynolds number = $\frac{\rho V \ell}{\mu}$
S	wing reference area, ft^2

S_{wet}	wetted area of component, ft^2
T	total temperature, degrees Rankine
$\frac{t}{c}$	airfoil thickness ratio
$\frac{x}{c}$	fraction of local chord length
x, y, z	Cartesian coordinates with origin at the wing apex, ft
α	wing angle of attack, degrees
α_{des}	design wing α corresponding to $C_{L_{des}}$, degrees
β	$\sqrt{M^2 - 1}$ for $M > 1$, $\sqrt{1 - M^2}$ for $M < 1$
γ	specific heat ratio = $\frac{c_p}{c_v} \approx 1.4$ for air
ϵ	surface emittance
ΔC_p	wing lifting pressure distribution = $C_{p_l} - C_{p_u}$
η	semispan fraction = $\frac{y}{b/2}$; $0 \leq \eta \leq 1.0$
θ	roll angle, degrees
λ	wing taper ratio = $\frac{c_t}{c_r}$
Λ_{le}	Leading edge sweep angle, degrees
σ	Mach angle = $sin^{-1}\left(\frac{1}{M_\infty}\right)$
μ	kinematic viscosity, $\frac{slug}{ft \cdot sec}$
σ	Stefan-Boltzmann constant = 0.483×10^{-12} $\frac{BTu}{sec \cdot ft \cdot {}^\circ R^4}$

Subscripts:

ad	adiabatic
des	a design value
vor	vortex
W	wall
∞	free stream condition

Abbreviations:

BDAP	Boeing Design and Analysis Program
HLFC	Hybrid Laminar Flow Control
HST	High Speed Transport
LFC	Laminar Flow Control
NLF	Natural Laminar Flow
SCLFC	Super Critical Laminar Flow Control

1 Introduction

The pursuit of enhanced aircraft performance is an ongoing venture for the Air Force, NASA, and the aviation industry. Their efforts, and the efforts of others, are yielding numerous new technologies which are rejuvenating many previously abandoned programs. One such program is the design and development of a profitable High Speed Transport (HST). future HST's. It has been concluded that for such an aircraft to be economically viable, significant performance improvements over those offered by current technologies must be made.

One of the most promising prospects for performance gains on HST's is the skin friction drag reduction associated with obtaining laminar flow over the wing. It has been predicted that laminar flow control (LFC) would provide more dramatic improvements than any of the other possible technological advances in aerodynamics (reference 1). The most encouraging means of doing this is through the use of Hybrid Laminar Flow Control (HLFC) systems. In such a system, the wing is designed to produce a pressure distribution conducive to natural laminar flow (NLF) over its midsection, while in the leading edge area the flow is stabilized by suction through perforated panels or narrow slots. HLFC research has already established an advantage in drag reduction for subsonic aircraft, and if significant amounts of laminar flow can be maintained on HST's, where skin friction typically accounts for more than one-third of the cruise drag, it could greatly enhance range and payload capabilities. The associated reduction in aerodynamic heating would also significantly reduce the structural weight, minimize the required thermal management, and prolong the material life. For these reasons, supersonic laminar flow control has been targeted by NASA as a crucial research area in the development of future High Speed Civil Transport's (reference 2).

There are, however, several adverse effects of designing aircraft to accommodate hybrid laminar flow control systems. These include the added weight and power requirements of the air-suction system, the possible maintenance difficulties associated with the porous suction walls, and the probable aerodynamic performance penalty of sustaining an upper surface pressure distribution which is amenable to HLFC. In this paper, the latter is addressed. A wing which was cambered solely to possess a pressure distribution favorable to HLFC would theoretically have more drag-due-to-lift than would be inherently produced by a wing that was cambered for minimum drag-due-to-lift, disregarding any boundary layer considerations. The intent of this study is to quantify this difference and determine its likely impact on the true benefits of HLFC wing designs.

It was determined that a parametric study of supersonic arrow wings would be useful in assessing these effects. The influence of taper ratio and aspect ratio were examined by including several planforms of varying shape in the study. The investigation was conducted at a Mach number of 2.0, since the effect of camber on minimum drag-due-to-lift decreases at higher Mach numbers. Thickness profiles of the wings are based on NACA 64-series airfoils. Two different design philosophies, a loading optimization method and a method to design HLFC wings, were used to camber each planform. The first, more conventional, design method involves optimizing wing camber and twist for minimum drag-due-to-lift at the design lift coefficient with no consideration for boundary layer type. This method has been used often in the preliminary design process, recent examples of which are described in references 3-5. The second design method involved cambering the wing to produce a given upper surface pressure distribution that had been determined to be desirable for HLFC wings. To achieve this, the same linear theory design program which was used to design the wings for minimum drag-due-to-lift was implemented, since programs which use higher order methods to design a three dimensional wing for a given pressure distribution are still in the development stages. This program has been found to be adequate in many previous preliminary designs, while providing the short computational turn-around times required to conduct a parametric study on several planforms in a limited time period. The current research has resulted in a process by which the program's optimization routine can be used to camber a wing such that it produces a spanwise lift distribution which will help to minimize drag-due-to-lift, while maintaining any given upper surface pressure profile in the streamwise direction, such as that desired for HLFC wings.

2 Prelimenary Evaluation of Supersonic Wings

For the evaluation of aerodynamic performance, the force estimates will be built up through superposition as shown in Figure 2.1. For this study, we will consider the drag components of skin friction drag, zero-lift wave drag, and drag-due-to-lift on the wing only. The drag-due-to-lift will include finite wing and leading edge vortex thrust effects. All of the methods used have been correlated with experimental data in several NASA studies including that of reference 6, which compares three computational methods to wind tunnel test data.

2.1 Zero-Lift Wave Drag

The wave drag of a configuration is typically calculated in one of two ways; either by the far-field (supersonic area rule) method or by the near-field (surface pressure integration) method. Both wave drag estimation methods have been used to evaluate the wings presented, and the results are compared for equivalence.

2.1.1 Far-Field Wave Drag

The zero lift far-field wave drag is computed using the supersonic area rule outlined in reference 7. The supersonic area rule is a derivative of the transonic area rule, which asserts that the wave drag of an aircraft is essentially the same as the wave drag of an equivalent body of revolution having the same cross-sectional area distribution. However, in the supersonic area rule, several equivalent bodies of revolution are produced by passing a series of parallel cutting planes through the configuration, inclined at the Mach angle σ to the aircraft axis (Figure 2.2). Each equivalent body is calculated at a constant azimuth (roll) angle θ. Then the area of the equivalent body at each longitudinal station is the projection of the area intercepted by the Mach plane onto a plane normal to the aircraft axis. The wave drag for each of these equivalent bodies at given free stream conditions is then calculated using the Von Kármán slender-body formula.

$$D(\theta) = \frac{-\rho\, U_\infty^2}{4\pi} \int_0^l \int_0^l A''(x_1)\, A''(x_2)\, log\,|\, x_1 - x_2 \,|\, dx_1\, dx_2 \tag{2.1}$$

where l is the length of the aircraft, A'' is the second derivative of the body area distribution, and x_1 and x_2 are the axial locations of two adjacent Mach planes which enclose the volume element. The total wave drag of the entire configuration is then computed as the integrated average of all of the equivalent-body wave drags.

$$D = \frac{1}{2\pi} \int_0^{2\pi} D(\theta)\, d\theta \tag{2.2}$$

In the program used to perform the calculations, equations 2.1 and 2.2 are integrated numerically over a specified number of intervals along the x-axis and in roll angle θ. The program also assumes the aircraft to be laterally summetric, thus calculations only need to be made for $0 \leq \theta \leq \pi$. For this study, 60 intervals in the x direction and 16 intervals in θ (over a range of π) are used.

2.1.2 Near-Field Wave Drag

The near-field method of computing wave drag is based on the integration of zero-lift thickness pressures over the configuration surface. The velocity potential over the wing is calculated using the familiar linear theory equation

$$\phi(x,y) = -\frac{1}{\pi} \int \int_\tau \frac{\lambda\, d\eta\, d\xi}{\sqrt{(x-\xi)^2 - \beta^2(y-\eta)^2}} \tag{2.3}$$

where

$\phi(x,y)$ = velocity potential at wing field point (x,y)

λ = surface slope $\left(\frac{dz}{dx}\right)$ at integration point

β = $\sqrt{M^2 - 1}$ (supersonic)

ξ = x variable of integration

η = y variable of integration

τ = interval of integration defined by the surface of the wing within the Mach cone from (x,y).

The wing thickness pressure coefficient is calculated using the relationship

$$C_p(x,y) = \frac{p - p_\infty}{q_\infty} = 2\frac{u}{U_\infty} = -2\frac{\partial\phi(x,y)}{\partial x} \qquad (2.4)$$

where

p = local pressure at (x,y)
p_∞ = free stream static pressure
u = x perturbation velocity
U_∞ = free stream velocity
q_∞ = free stream dynamic pressure

The computer programs that were used for the supersonic analysis have this velocity potential integration approximated by a numerical summation on a system of rectangular elements known as a "Mach box" grid system (fig 2.3). A field point is defined by its coordinates $(x, \beta y)$ and an influencing element is defined by the coordinates $(\xi, \beta\eta)$. Note that only the elements ahead of an inverse Mach line originating at the center-rear of the field point (the shaded area) are included in the summation. In the calculation of surface pressures due to thickness, the wing is completely defined by its thickness distribution (to define the surface slopes λ). The near-field wave drag is then calculated by integrating the pressure components in the axial direction.

2.2 Drag-Due-to-Lift

For a first order analysis, the drag-due-to-lift is also computed using linear aerodynamic theory. The wing is evaluated using linear theory solutions (equations 2.3 and 2.4) on the same type of "Mach box" grid used in the near-field wave drag solution. However, the thickness definition is not required, since only the camber surface (defined by the airfoil mean lines) is included in the lifting solution. Since the flow is supersonic, a simple aft-marching solution can be used. The drag-due-to-lift increment is then found by the integration of the pressure force components on the camber surface in the axial direction, and the lift is found by the integration of the component of the lifting pressures in the normal direction.

Attainable vortex (leading edge) thrust coefficient values are estimated and included in the drag-due-to-lift calculation. The method used to estimate the attainable vortex thrust was developed and outlined in reference 8. The authors of reference 8 used simple sweep theory and a study of experimental two-dimensional airfoil data to define an empirically based attainable local thrust factor, K_T, as a function of the airfoil geometry, Mach number normal to the leading edge, and the Reynolds number. K_T is defined as the ratio of the attainable leading edge thrust coefficient to the value corresponding to full vortex thrust (fully attached flow). The values of K_T vary from zero for vortex flow to unity for fully attached flow. The essential ideas of this theory are illustrated in Figure 2.4. To calculate the local attainable thrust factor, K_T, for a given wing section using this procedure the local leading edge radius must first be defined. The leading edge radius of a given airfoil is determined (reference 8) by fitting a square-root function to the thickness distribution using the equation

$$\frac{t}{2c} = K\sqrt{\frac{x}{c}} \tag{2.5}$$

where the constant K can be evaluated by selection of some $\frac{x}{c}$ near the leading edge and the corresponding $\frac{t}{c}$. The equation for a circle of radius $\frac{r}{c}$ which is tangent to the half thickness curve (or the airfoil surface) at the leading edge is

$$\left(\frac{x}{c} - \frac{r}{c}\right)^2 + \left(\frac{t}{2c}\right)^2 = \left(\frac{r}{c}\right)^2 \tag{2.6}$$

and can be solved with equation 2.5 at $\frac{x}{c}$=0 to obtain the leading edge radius ratio.

$$\frac{r}{c} = \frac{K^2}{2} \tag{2.7}$$

Note that this expression gives the leading edge radius in the chordwise direction. Simple sweep theory is used to calculate the $\frac{r}{c}$ and maximum $\frac{t}{c}$ normal to the leading edge, which are used with the Reynolds number and Mach number normal to the leading edge to calculate K_T based on empirically derived equations.

2.3 Friction Drag

Since the primary purpose of HLFC systems is to reduce the friction drag over the wing, this is a critical part of the analysis. To get a single correct value for the drag component due to friction, C_{D_f}, the pressure distribution over the entire wing would be found using an Euler code (or some other high-order method). This pressure (or velocity) distribution would then be used to perform a boundary layer stability analysis using a code such as COSAL (reference 9). Knowing what types of flow exist over various parts of the wing, the corresponding local friction coefficients c_f for various surface regions would then be calculated and the total friction drag coefficient,

C_{D_f}, of the wing could be obtained. An even more accurate but very time consuming method would be to obtain Navier-Stokes solutions over the wing which would include the effects of viscosity.

Performing these calculations on a single configuration is time consuming, and doing so for a large number of configurations, at least in this application, is prohibitive due to time constraints. Therefore, some assumptions will be made as to the type of flow (laminar or turbulent) that should exist over the surfaces of the wings. The wings designed by the camber optimization method will be assumed to have turbulent flow over the entire wing, though they may actually be capable of maintaining small areas of laminar flow under most flight conditions. The wings designed for LFC will be evaluated assuming various amounts of laminar flow over their upper surfaces, giving optimistic, conservative, and most likely estimates for the friction drag.

The friction drag calculations are based primarily on the T' method for the turbulent flow regions, and on Blasius' theory for the areas of laminar flow. Since both of these methods assume flow over a flat plate, the components of the aircraft are represented as strips of appropriate wetted areas and reference lengths. Components like the wing, which vary greatly in chord length, must be divided spanwise into several strips for better approximations of the friction drag. The drag increments on all of the strips are then summed to obtain the total friction drag of the configuration.

2.3.1 Turbulent Boundary Layer Friction Drag

The skin friction drag for turbulent flow is computed using the T' method outlined by Sommer and Short in reference 10. This method assumes that the surface is a smooth flat plate with turbulent boundary layer conditions. Also, transition is assumed to occur at the leading edge of each component or strip.

The T' method is based on the calculation of a compressible skin friction coefficient C_f, from a reference skin friction coefficient, C'_f, for the given Mach number, M_∞, Reynolds number, R_∞, and adiabatic wall temperature, $T_{W_{ad}}$. The atmospheric pressure, p_∞, temperature, T_∞, kinematic viscocity, μ_∞, and Reynolds number per Mach per unit length, $\frac{R_\infty}{M_\infty l}$ are first calculated for the given flight altitude using 1962 standard day atmosphere equations.

The following calculations are then iterated for each component to determine the non-adiabatic wall temperature, T_W, and skin friction coefficient, C_f. For the first iteration, the wall is assumed to be adiabatic, and wall temperature is approximated using the compressible, one-dimensional, adiabatic wall equation

$$\frac{T_{W_{ad}}}{T_\infty} = 1 + r\,\frac{\gamma - 1}{2}\,M_\infty^2 \tag{2.8}$$

If we assume that γ=1.4 for air, and a wall recovery factor r of 0.88, we get

$$\frac{T_{W_{ad}}}{T_\infty} = 1 + 0.176\;M_\infty^2 \tag{2.9}$$

Sommer and Short (reference 10) obtained the key relationship to this theory based on experimental data, which is

$$\frac{T'}{T_\infty} = 1 + 0.035\;M_\infty^2 + 0.45\left(\frac{T_W}{T_\infty} - 1\right) \tag{2.10}$$

The Reynolds number relationship, assuming a constant pressure through the boundary layer and a thermally perfect gas, is

$$\frac{R'}{R_\infty} = \frac{1}{\left(\frac{T'}{T_\infty}\right)\left(\frac{\mu'}{\mu_\infty}\right)} \tag{2.11}$$

in which the dynamic viscosity ratio is given by the Sutherland relationship (with the Sutherland viscosity constant set to 198.72 °R)

$$\frac{\mu'}{\mu_\infty} = \left(\frac{T'}{T_\infty}\right)^{1.5}\left(\frac{T_\infty + 198.72}{T' + 198.72}\right) \tag{2.12}$$

where the T's are expressed in degrees Rankine. The Reynolds number found by equation 2.11 is used to calculate the incompressible skin friction coefficient, given by the Kármán-Schoenherr equation

$$\frac{0.242}{\sqrt{C_{f_i}}} = log_{10}\left(C_{f_i}R_i\right) \tag{2.13}$$

which, using the T' analogy, gives

$$\frac{0.242}{\sqrt{C'_f}} = log_{10}\left(C'_f R'\right) \tag{2.14}$$

This equation must be solved iteratively to obtain C'_f. Then, using the relationships

$$\frac{C'_{f_i}}{C'_f} = \frac{1}{1 + 3.59\sqrt{C'_f}} \tag{2.15}$$

and

$$\frac{C_{f_h}}{C'_{f_h}} = \frac{T_\infty}{T'} \tag{2.16}$$

we can solve for

$$C_{f_h} = \frac{C'_f}{1 + 3.59\sqrt{C'_f}}\,\frac{T_\infty}{T'} \tag{2.17}$$

which is then used in the equation

$$\left(\frac{\varepsilon\ \sigma}{h}\right) = \frac{\varepsilon\ (0.10425 \times 10^{-12})}{\mu\ C_{f_h}\ (R_\infty/l)} \tag{2.18}$$

Now the non-adiabatic wall temperature may be calculated using

$$T_W = \frac{T_{W_{aw}}}{\left[1 + \left(\frac{\varepsilon\sigma}{h}\right)\ T_W^3\right]} \tag{2.19}$$

This value replaces the adiabatic wall temperature as an initial estimate in the next iteration which starts with equation 2.10. Once equation 2.19 has converged (within five iterations), then the compressible skin friction coefficient C_f is found using the value for C'_f from equation 2.14 using the relationship

$$\frac{C_f}{C'_f} = \frac{\rho'}{\rho_\infty} = \frac{T_\infty}{T'} \tag{2.20}$$

2.3.2 Laminar Boundary Layer Friction Drag

For a flat plate, if viscous effects are assumed to be confined to a thin layer over the surface and a uniform velocity is assumed outside the boundary layer, Blasius found that the local skin friction coefficient at a distance x behind the leading edge of the plate could be expressed as

$$c_f = \frac{0.664}{\sqrt{R_x}} \tag{2.21}$$

where the local Reynolds number, $R_x = \rho V x/\mu$. Thus the average skin friction coefficient C_f for one side of the flat plate of unit width and of length l is given by the relationship

$$C_f = \frac{1}{l}\int_0^l c_f\ dx = \frac{1.328}{\sqrt{R_l}} \tag{2.22}$$

where $R_l = \rho V l/\mu$, and l is the characteristic length of the plate (reference 11). Excellent agreement between theoretical and experimental skin friction coefficients has been observed, as long as the boundary layer actually remains laminar.

2.3.3 Mixed Boundary Layer Friction Drag

As previously discussed, the T' method and the Blasius method were used together to obtain friction drag solutions for mixed flows. This mixed type of flow is assumed to be laminar at the leading edge of the strip, then is instantly changed to fully turbulent flow at a specified location downstream (Figure 2.5). Of course, the presence of the laminar region effects a lower friction drag than would be produced by a fully turbulent flow. Following the teaching of L. Prandtl, this reduction in drag can be estimated by assuming that behind the point of transition, the turbulent boundary layer behaves as if it were turbulent from the leading edge. Thus, from the turbulent friction drag of the whole length, we subtract the turbulent friction drag of the part up to the transition and add the laminar friction drag for that same length (reference 12). It is crucial that these drag increments be based on the correct reference lengths in all of the calculations. The drag increment produced by a component (strip), defined by a wetted area, S_{wet}, a reference length, ℓ, and a specified percentage of laminar flow, x_{lam}, can be calculated using the relationship

$$C_{D_f} = C_{f,turb}\frac{S_{wet}}{S_{ref}} - [c_{f_t} - c_{f_\ell}]\frac{x_{crit}}{l}\frac{S_{wet}}{S_{ref}} \tag{2.23}$$

where

$C_{f,turb}$ = turbulent skin friction coefficient of the entire length (based on l)
c_{f_t} = turbulent skin friction coefficient of the laminar part (based on x_{crit})
c_{f_ℓ} = laminar skin friction coefficient of the laminar part (based on x_{crit})
l = the reference length of the strip
x_{crit} = distance from the leading edge at which transition occurs
S_{wet} = wetted area of the strip
S_{ref} = reference area

The turbulent skin friction coefficients $C_{f,turb}$ and c_{f_t} are estimated using the T' method, and the laminar skin friction coefficient c_{f_ℓ} is calculated using the Blasius formula. The total skin friction drag is then the sum of the component drags

$$C_{D_f} = \sum_{n=1}^{N} C_{D_{f,n}} \tag{2.24}$$

where N is the total number of components.

A computer program has been written to calculate the C_{D_f} for mixed flows based on these combined methods. The program was written in Fortran77, and its execution times were very short due to the quick convergence of equations 2.14 and 2.19. The wetted area calculations were made with a code which previously existed in FortranIV, but was converted to Fortran77. This code breaks down a general configuration defined in the Craidon Wave-Drag format into the wetted areas and reference lengths required by the skin friction program. This program was also modified so that it would write a data file in the format required for input to the skin friction program. Flight condition cards are appended to the end of this file (as many as desired) which specify the desired Mach numbers and altitudes for the calculations. Using this file, without further modifications, as input to the skin friction drag program results in the calculation of the configuration's C_{D_f} assuming fully turbulent flow and a surface emittance, ε, of 0.8. If a partially (or fully) laminar solution is desired, the user must also modify the input file to include the desired amount of laminar flow on the upper and lower surfaces of each strip of the wing. This may be defined by either: (1) the percent area (or % chord length) of laminar flow; (2) the specification of a critical Reynolds number, $R_{x,crit}$; or (3) the critical length, ℓ_{crit}, at which the flow is to become turbulent. The specified parameter is used to calculate the other two parameters for each strip at each Mach-altitude combination, and all are included in the output. The program output also includes the average skin friction coefficients, C_f, and skin friction drag coefficients, C_{D_f}, at each Mach-altitude combination for each component (strip) as well as for the entire configuration.

2.4 Validation of Pressure Distribution Estimates

Since the programs used in this study were developed elsewhere, it was felt necessary to evaluate the validity of the predictions given, and the present application of the computer programs. The theories themselves have been previously evaluated in references 13 and 14 and have since been incorporated in several programs.

The Boeing Design and Analysis program (to be discussed in chapter 3) was used to estimate all pressure distributions presented in this paper and is evaluated here for accuracy. Comparisons between theoretical results from BDAP and the experimental data presented in reference 14 were made on two wings of the same planform layout (shown in Figure 2.6). The first wing was not cambered, thus separating the effects of camber in the solution. A second wing had been cambered for minimum drag-due-to-lift, using optimization techniques which were available at the time, at a design lift coefficient of 0.08 (Figure 2.7).

Evaluation of both the uncambered and cambered wings (Figure 2.8[a-g]) shows the theory to be adequate in assessing pressure gradients, and even pressure levels, over most of the wing. Agreement between the predicted and experimental pressure levels appears to be good near the root, but it deteriorates near the wing tips, especially at high lift conditions (Figures 2.8[c] and 2.8[g]). It is believed that this discrepancy may be mostly due to aeroelastic effects on the test wing. However, while these pressure levels near the tip may significantly disagree, the pressure gradients in that region still correspond fairly well. The predictions of the pressure levels and gradients near the leading edge also prove to be inferior, especially at high angles of attack. This suggests the presence of a vortex flow originating at the wing apex, producing areas of separated flow. This type of flow is not predicted by the linear methods used; thus, its effect on the surface pressure is not observed. These pressure differences introduce little error in the prediction of the aerodynamic forces, since the areas affected are small. Indeed, it has been shown in references 13 and 14 and in several other investigations performed since then (such as that of reference 6), that when the force estimates are combined with attainable vortex thrust estimates (section 2.2), the force predictions correlate very well with test data, even for wings with blunt leading edges. The small errors in the predicted pressure levels can, however, introduce significant errors in the moment predictions, and are certainly a concern when pressures, as in the present case, are of importance.

3 Designing Wings for Minimum Drag-Due-to-Lift

To assess the effects of designing wings for laminar flow control, a reference design method must be defined upon which performance comparisons may be based. The baseline design process used in this report is a somewhat standard wing loading optimization scheme that is presently in use at NASA's Langley Research Center. Although other wing optimization methods exist, this method was chosen to develop the optimized set of wings, partially for convenience since it is used by the Boeing Design and Analysis (BDAP) code and enabled the entire parametric analysis to be conducted on the same computer system. Examples of this design method have been illustrated in references 3-5. The technique involves the determination of the lifting load distribution which will produce the minimum drag-due-to-lift, and the definition of the camber surface required to produce such an optimum loading.

3.1 Lifting Load Optimization Theory

The wing optimizations in this paper were performed using the wing design module of the Boeing Design and Analysis Program (BDAP). This code (references 15-18) uses an optimization scheme to combine several basic lifting pressure distributions in an optimum fashion in order to obtain a total wing loading distribution which produces the minimum drag-due-to-lift at the design lift coefficient (and at a design zero-lift moment coefficient if desired). The lifting pressure distribution, often called the lift loading, is simply the difference between the lower and upper surface pressures. In linear theory, this loading is assumed to be entirely independent of the thickness distribution. The equations for the candidate lifting loadings which are considered for the design of the wings in this study are listed in Table 3.1.

The performance of each of the candidate loadings is evaluated by integrating the lifting pressures over the wing to obtain its overall lift, drag-due-to-lift, and zero-lift pitching moment. In addition, the interference drag increments are calculated,

Table 3.1: Candidate Loadings Considered in Wing Designs

#	$\Delta C_p =$	Loading Description
1	k [a]	uniform loading
2	$k\ y$ [b]	linear spanwise
3	$k\ y^2$	quadratic spanwise
4	$k\ \eta^2(\eta - 1)^2$	mid-span loading
5	$k\ \sqrt{1 - \eta}$	elliptical spanwise
6	$k\ x'$ [c]	linear chordwise
7	$k\ x'^{\,2}$	quadratic chordwise
8	$k\ x'(c - x')$	parabolic chordwise
9	$k\ x'^{\,2}(1.5\ c - x')$	cubic chordwise
10	$k\ 2(1 + 5\frac{x}{c})^{-0.5}$	similar to flat wing
11	$k\ \Delta C_{p,conf}$	$\propto$ configuration dependent
12	$\Delta C_{p,conf}$	configuration dependent

---

[a] k's = constants of proportionality.

[b] y=spanwise distance from wing centerline.

[c] x'=longitudinal distance from the leading edge.

representing the drag induced on each loading by each of the other loadings. Each loading is then multiplied by a constant of proportionality, k, such that its resultant theoretical lift coefficient is unity. This eliminates any effect that machine precision might have on the optimization process if the basic loadings were to produce lift varying greatly in magnitude. These aerodynamic characteristics are supplied to the optimization routine where Lagrange's method of undetermined multipliers is used to determine the weighting factors, W_i, of each candidate loading that will minimize the wing axial force (drag-due-to-lift) while producing a specified normal force (lift) and, if requested, a specified zero-lift moment coefficient. During the optimization process, these aerodynamic forces are estimated by

$$C_L = \sum_{i=1}^{n} W_i\ C_{L,i} \tag{3.1}$$

and

$$C_m = \sum_{i=1}^{n} W_i\ C_{m,i} \tag{3.2}$$

where

n = number of candidate loadings fed to the optimization routine

$C_{L,i}$ = lift coefficient of the i^{th} loading

$C_{m,i}$ = moment coefficient of the i^{th} loading

Note that these estimates are calculated using linear theory and therefore include no attainable vortex thrust considerations. For this study moment constraints were not enforced since it would not be possible to apply them in the design method of Chapter 4. During preliminary design it is generally considered to be better to trim the aircraft by movement of the center of gravity anyhow.

Wing loadings which are independent of the wing itself (such as body buoyancy, body upwash, and nacelle buoyancy pressures), may be accounted for as '*configuration dependent*' loadings (candidate loading type 12 in Table 3.1). These configuration dependent loadings are forced to have weighting factors of unity since they are not produced by the wing itself and thus yield no camber surface. They are intended to allow the optimization of the camber surface in the presence of aerodynamic wing loadings caused by entities other than the wing itself. If desired, the configuration dependent loadings may also be used as candidate loadings in the optimization process (loading type 11) to provide a good means of using camber to capitalize on any beneficial effects of an external loading (type 12), or to cancel the lift of the independent effect, if that be the optimum solution. In such an optimization, the configuration dependent loadings may be calculated by the program; or, they may be input by the user in tabular form.

Since linear theory contains no limitations on the surface pressure coefficients, it can predict physically impossible pressures less than vacuum pressure. Experimental data, however, indicates that it is advisable to reject theoretical solutions when predicted suction values exceed 70-80% of vacuum pressure (reference 19). To help insure a physically possible design lifting pressure loading, upper surface pressure constraints are applied during the wing design process. The surface pressure is generally constrained to be greater than $\frac{7}{10}$ of vacuum pressure,or

$$Cp \geq .7\left[\frac{-p_\infty}{q_\infty}\right] = .7\left[\frac{-1}{\frac{1}{2}\gamma M_\infty^2}\right] \tag{3.3}$$

To design with this constraint, the thickness pressures are first evaluated using the near-field wave drag module so that it may be included in the limiting. The program also provides options of adding camber constraints and pressure gradient constraints at given locations on the wing.

3.2 Definition of the Camber Surface

Since the aerodynamic performance evaluations provided in the design mode are actually the linear combinations of several camber surfaces, small numerical errors that are introduced for each surface can accumulate into a larger error. Thus, for an analysis of the final design, the separate loadings are consolidated to define the optimum lifting loading definition, and the lifting pressure at any point on the wing is taken to be

$$\Delta C_p(x, y) = \sum_{i=1}^{n} W_i \, \Delta C_{p,i}(x, y) \tag{3.4}$$

Linearized theory is then used to calculate the wing surface shape required to support the optimized lift distribution (reference 15) by the integral equation

$$\frac{\partial z}{\partial x}(x, y) = -\frac{\beta}{4} \, \Delta C_p(x, y) + \frac{1}{4\pi} \int\int_{\tau} \bar{R}(x - \xi, y - \eta) \, \Delta C_p(\xi, \eta) \; d\beta\eta \; d\xi \tag{3.5}$$

where

$$\bar{R} = \frac{x - \xi}{\beta^2 (y - \eta)^2 \sqrt{(x - \xi)^2 - \beta^2 (y - \eta)^2}} \tag{3.6}$$

where

$\beta = \sqrt{M^2 - 1}$ (supersonic)

$\xi = x$ variable of integration

$\eta = y$ variable of integration

$\tau =$ interval of integration defined by the surface of the wing planform within the Mach cone from (x, y).

The inversion method by which the BDAP uses the lifting pressure distribution to define the corresponding camber surface is known to often predict camber surfaces that are too severe near the plane of symmetry. The designer may either avoid this by imposing camber constraints at the root of the wing during the optimization process, or he can correct it by substituting a milder (or even flat) camber definition at the root of the wing subsequent to the calculation of the camber surface. This camber surface definition may then be combined with the thickness definition and evaluated using whatever methods are at hand. The evaluation techniques used in this paper have already been discussed in detail in Chapter 2.

3.3 Application to a Sample Wing

The design method described in this chapter was applied to a baseline planform with $\lambda = .1$ and AR=2.0 which subsequently will be referred to as the baseline planform. The planform (reference) area of the wing was chosen to be 8000 square feet and the leading edge sweep was chosen to be 67° . The wing was designed for a Mach number of 2.0 at a cruise altitude of 55,000 feet. A NACA-64 series airfoil thickness profile with a maximum thickness ratio of 4% was used for the wing (Figure 3.1). The basis for these selections will be discussed in Chapter 5.

In using the wing design module of BDAP, several inconsistencies were observed. After evaluating camber surfaces created by several design runs, it was found that using all of the candidate loadings (in Table 3.1) in the optimization did not necessarily lead to the best performing wing. In the present analysis, use of the loading similar to a flat plate (# 10) was found to cause quite poor results. It was later discovered that many users have had trouble with this loading, and it is generally recommended that it not be used. This may be related to the fact that this loading is the *only* one for which the difference between the leading edge ΔC_p and the trailing edge ΔC_p is nonzero and in no way a function of the local chord length. It can be easily found that for this loading, lifting pressure at the leading edge is $(\sqrt{6})$ times the lifting pressure at the trailing edge for any value of c. This can result in a very large gradient in ΔC_p for areas where the local chord length is very short, causing highly tapered wings to be excessively twisted at the tips.

It was also found that excluding the chordwise cubic loading (# 9) resulted in wings which performed almost as well as when the loading was included, while producing a much milder camber surface. This paradox is mentioned in reference 16, where it is suggested that the combination of the higher order chordwise loadings tend to produce excessive twist or waviness in the calculated camber surface unless constraints are imposed on the wing's upper surface pressure level and gradient. It was found, through several design calculations involving different combinations of candidate loadings and constraints, that if reasonable pressure gradient constraints were imposed at the root section of the wing, the unwanted waviness in the calculated camber surface was minimized, even when using loadings 5-8 simultaneously in the optimization. An overall pressure minimum constraint of $\frac{7}{10}$ vacuum pressure was also applied during the design process but was found to be unnecessary due to the low design C_L of the wing. Thus, the wing was designed using loadings 1-8 in Table 3.1 with pressure gradient constraints at the root.

The most heavily weighted chordwise loadings from the optimization were found to be the linear (#6) and quadratic (#7) candidates, and the most lightly weighted was the parabolic candidate (#8). It was also observed that the elliptical loading (#5) was the most heavily weighted spanwise loading, and the mid-span loading (#4) was the most lightly weighted. The uniform loading (#1) was also among the most heavily weighted loadings.

The baseline planform, designed in such a way, is shown in Figure 3.2 and its corresponding pressure distribution in Figure 3.3. As previously discussed in this chapter, the inverse solution in the BDAP program often yields excessive camber at the root of the wing (as seen in Figure 3.2). This was corrected here by linearly extrapolating the camber values from the next two span stations to obtain a new root camber definition. Softening the camber actually improved the performance of the wing as evaluated by the methods described in Chapter 2. This is probably because the evaluation methods are of a slightly higher order than the design methods, including attainable leading edge thrust. The resulting wing, for our baseline planform is shown in Figure 3.4, and its airfoil sections are shown more clearly in Figure 3.5. As shown in Figure 3.6, this wing design possesses a much flatter upper surface pressure distribution than before the root modification, though this was not a goal in the design process.

4 An Inverse Design Method for HLFC Wings

4.1 Design Goals

The objective of this design procedure is to camber the wing such that it produces an upper surface pressure distribution which promotes natural laminar flow over the mid-section of the upper surface, thus making the wing amenable to a hybrid laminar flow control (HLFC) system. In references 20 and 21, the authors discuss the type of upper surface pressure distribution which maximizes the design Mach number of supercritical laminar flow control (SC LFC) airfoils while maintaining attached flow. A pressure distribution with a low supersonic flat rooftop, preceded by a supersonic front pressure minimum, has shown itself to be superior. Since linear potential methods are to be employed in this design process, the pressure rise near the trailing edge will not be noticed. Also, since this method was shown (in Section 2.4) to be somewhat deficient in estimating the pressures near the leading edge, the small front pressure minimum will not be sought. With these approximations, the pressure distribution that we seek on the upper surface simplifies to a constant in the chordwise direction, often called a '*flat-roof-top*' pressure distribution.

To design the camber surfaces of the laminar flow wings, the Boeing Design and Analysis Program (BDAP) described in Chapter 3 is incorporated. This program is not intended to directly design a wing for any given upper surface pressure distribution since it bases the camber surface designs on the lifting pressure distribution. This necessitates a somewhat unconventional use of the code, but as will be shown, it allows the design process to include an optimization of the spanwise lifting distribution for minimum drag-due-to-lift.

4.2 Inverse Design Procedure

This method takes advantage of the linear theory assumption that if a camber surface can be expressed as a linear combination of two or more camber portions, then the aerodynamic characteristics of the camber surface may evaluated as the sum of the aerodynamic characteristics of these camber portions. The lifting loading of the HLFC wing will be considered to be made up of two portions which will be linearly combined to define the design wing loading. The first portion will be referred to as the flat-roof-top loading. This loading is one which will combine with the thickness pressures to produce a flat chordwise upper surface pressure distribution, while producing little or no lift across the span. In other words, it is desired that the section lift coefficient at each span station and the total lift both be zero. This type of lifting pressure distribution is illustrated in Figure 4.1 for a wing, and in Figure 4.3[a] for a given span station on the wing.

The second portion of the total lifting loading, which is responsible for producing the wing lift, will be called the span-optimized loading. This name was chosen since this loading is to have a spanwise lifting distribution which is optimized for minimum drag-due-to-lift, while having a constant chordwise lifting pressure at each span station (i.e. pure aerodynamic twist). The optimization is performed in the presence of the flat-roof-top loading. The span-optimized loading is illustrated in Figure 4.2 for a wing, and in Figure 4.3[b] for a given span station on the wing.

These two pressure distributions will combine with the thickness distribution (Figure 4.3[c]) to define a wing surface pressure distribution which possesses a flat-roof-top in the chordwise direction and a spanwise lifting distribution optimized for minimum drag-due-to-lift (Figure 4.3[d]). The camber surface corresponding to each of these loadings is calculated using linear theory. Once these camber surface descriptions are defined, they are combined with the thickness description and evaluated to see how well the total upper surface pressure gradients correspond with those desired. If these are satisfactory, the wing is ready to be evaluated for its overall aerodynamic characteristics using the methods described in Chapter 2.

4.2.1 Determination of the Flat-Roof-Top Loading Distribution

Since the BDAP code uses lifting pressures (loadings) as a basis for the optimization of the design, it is necessary to determine the loading distribution which would combine with the thickness pressures to produce the desired upper surface pressure distribution. This loading distribution is dependent on the planform shape as well as the thickness profile of the wing.

The lifting pressure coefficient is defined as the difference between the lower and upper surface pressures, or:

$$\Delta C_p = C_{p_l} - C_{p_u} \tag{4.1}$$

In linear theory, the upper and lower surface pressures are assumed to be a linear combination of the effects of thickness and camber,or

$$C_{p_u} = C_{p_{u,t}} + C_{p_{u,c}} \tag{4.2}$$

and

$$C_{p_l} = C_{p_{l,t}} + C_{p_{l,c}} \tag{4.3}$$

where

$C_{p_{l,c}}$ = lower surface pressure coefficient due to camber
$C_{p_{u,c}}$ = upper surface pressure coefficient due to camber
$C_{p_{l,t}}$ = lower surface pressure coefficient due to thickness
$C_{p_{u,t}}$ = upper surface pressure coefficient due to thickness

Due also to the linearity of the solution, the pressures due to camber follow the relationship

$$C_{p_{u,c}} = -C_{p_{l,c}} \tag{4.4}$$

and the pressure due to thickness is the same on the top surface as on the bottom, or

$$C_{p_t} = C_{p_{u,t}} = C_{p_{l,t}} \tag{4.5}$$

so

$$\Delta C_p = C_{p_{l,t}} + C_{p_{l,c}} - C_{p_{u,t}} - C_{p_{u,c}} = -2\ C_{p_{u,c}} \tag{4.6}$$

This also means that, for a design case :

$$C_{p_{u,des}} = C_{p_{u,t}} + C_{p_{u,c,des}} \tag{4.7}$$

From linear theory, the surface pressure due to thickness on the wing is simply the average of the upper and lower surface pressures, or

$$C_{p_{u,t}} = \frac{C_{p_u} + C_{p_l}}{2} \tag{4.8}$$

so

$$C_{p_{u,c,des}} = -\frac{C_{p_u} + C_{p_l}}{2} + C_{p_{u,des}} \tag{4.9}$$

and using equation 4.6

$$\Delta C_{p_{des}} = 2\left(\frac{C_{p_u} + C_{p_l}}{2} - C_{p_{u,des}}\right) \tag{4.10}$$

For a given wing planform, with a given thickness distribution, the upper and lower surface pressures (C_{p_u} and C_{p_l}) are calculated at any lift condition for the uncambered wing. These pressures are then used in Equation 4.10 to determine the loading distribution ($\Delta C_{p_{des}}$) required to sustain any given pressure distribution over the upper surface of the wing ($C_{p_{u,des}}$).

For our case, we are not really interested in maintaining a specific upper surface pressure distribution, but rather a specific upper surface pressure profile, or gradient distribution. The profile we seek has been simplified to be a flat one (flat-roof-top). Thus, any chordwise constant $C_{p_{u,des}}$ may be used in equation 4.10 to give an equally suitable upper surface pressure distribution. To design the flat-roof-top camber portion, a constant $C_{p_{u,des}}$ is found at each span station such that the average lifting pressure loading (ΔC_p) is nearly zero, or

$$\int_0^1 \Delta C_{p_{des}}\, d\left(\frac{x}{c}\right) \approx 0 \tag{4.11}$$

This is done in an attempt to maintain a spanwise loading distribution and overall lift coefficient of nearly zero for this camber portion. A computerized spreadsheet was found to be very useful in finding the $C_{p_{u,des}}$ required to do this, and in creating the input data records for the wing design program.

4.2.2 Determination of the Span- Optimized Loading and Camber Surface

In the design of this surface portion, the optimization capabilities of the BDAP code are utilized. The flat-roof-top loading distribution is included in the optimization as a configuration dependent loading (loading type 12 in Table 3.1). The BDAP program is used to determine the optimum combination of the candidate lifting loadings which were constant in the chordwise direction (loadings 1-5 in Table 3.1) in the presence of the flat-roof-top loading. Since the flat-roof-top loading is not considered by the program to be a camber-dependent loading, its weighting factor is forced to be equal to unity in the optimization process and is not included in the camber surface calculation. Linear theory is then used to calculate the span-optimized portion of the camber surface from the span-optimized portion of the loading distribution. When the span-optimized portion of the lifting surface is evaluated alone, its loading distribution is seen to be constant in the chordwise direction and somewhat elliptical in the spanwise direction.

4.2.3 Determination of the Flat-Roof-Top Camber Surface

The portion of the camber surface required to produce the flat-roof-top loading distribution is obtained using BDAP by bypassing its optimization routine. The program is used to find the weighting factor, W_i, which is required to enable a single candidate loading, proportional to the flat-roof-top loading (input as loading 11 in Table 3.1), to meet a specified lift coefficient criterion. When such a non-optimized solution is requested, the program will calculate the camber surface required to support even a configuration-dependent loading.

To know what the design lift coefficient should be in this computation, the results obtained during the calculation of the span-optimized loading must be used. During this process each candidate loading was evaluated for its aerodynamic properties before being submitted to the optimization routine. This was also true for the flat-roof-top loading, since its lift increment, denoted by $C_{L_{f.r.t.}}$, had to be accounted for in the total lift. When $C_{L_{f.r.t.}}$ is used as our design lift coefficient and the optimization routine is bypassed, the weighting factor, W_i, required to meet this criterion should be near unity since this loading alone is expected to meet the design lift condition. The camber definition required to support the input loading distribution times this weighting factor is then calculated by the program using linearized theory (equation 3.5).

4.2.4 Total Camber Surface

Using the linear theory assumptions made at the beginning of this chapter the flat-roof-top portion and the spanwise-optimized portion of the camber surface. are combined to define the design camber surface. This camber surface will produce a spanwise lift distribution designed for minimum drag-due-to-lift, and produce a chordwise lifting pressure distribution which will combine with the thickness pressures to yield a flat-roof-top pressure distribution. As discussed in Chapter 3, the linear theory inversion method used by BDAP calculates camber surfaces that are usually too severe near the plane of symmetry. In a typical optimization design process, the designer has two options to correct this. He may either impose camber constraints at the root of the wing during the optimization process, or he can substitute a milder camber definition at the root of the wing subsequent to the calculation of the camber surface. Since our solution to the flat-roof-top portion of the design already has one constraint (lift coefficient) and only one loading distribution to satisfy it with, no further constraints are possible. For this reason, after the design camber surface is obtained using the methods previously outlined, the root section should be replaced with a much milder definition. It was felt that, for this use of the program, it would be best to rotate the root airfoil until the three inboard trailing edge camber values formed a straight line. That is, the three inboard sections would have a linear relationship in twist. In this way, the calculated camber definition of the inboard airfoil section would be maintained.

4.2.5 Summary of Inverse Design Procedure for HLFC Wings

(a) Define the wing planform geometry and thickness distributions.

(b) Evaluate the flat wing for pressure distribution.

(c) Use the flat wing pressures in the equation

$$\Delta C_{p_{des}} = 2\left(\frac{C_{p_u} + C_{p_l}}{2} - C_{p_{u,des}}\right) \tag{4.10}$$

adjusting $C_{p_{u,des}}$ at each span station such that

$$\int_0^1 \Delta C_{p_{des}} \, d\left(\frac{x}{c}\right) \approx 0 \tag{4.11}$$

to define the flat-roof-top loading distribution.

(d) Calculate the span-optimized loading distribution, using only the chordwise-constant candidate loadings in BDAP's wing design module, in the presence of the flat-roof-top loading. This procedure also yields the calculated lift increment produced by the flat-roof-top loading, $C_{L_{f.r.t.}}$.

(e) Determine the camber surface required to produce the flat-roof-top loading using BDAP's wing design module. This is done by using the flat-roof-top loading as the only candidate loading, bypassing the optimization routines, and designing at $C_{L_{f.r.t.}}$.

(f) Combine the flat-roof-top and span-optimized camber surface definitions to define the design HLFC camber surface.

(g) Adjust the twist definition at the root to provide a more continuous spanwise camber definition.

4.3 Application to a Sample Wing

The design procedure described in this chapter was used to develop an HLFC wing having the same planform and thickness distribution as the wing which was designed for minimum drag-due-to-lift using the method of Chapter 3.

As discussed previously, this design procedure involves the definition of the design camber surface in two portions. The uncambered wing was first evaluated to determine its upper and lower surface pressure distribution. This distribution is shown in Figure 4.4 at the design lift coefficient of 0.08 for the baseline planform. This pressure distribution was then used in equation 4.10 to find the flat-roof-top loading distribution. This is the loading that combines with the thickness pressures to create a constant chordwise upper surface pressure distribution. The design upper surface pressure, $C_{p_{u,des}}$, in equation 4.10 was specified to be a constant value at each span station and was varied until the average ΔC_p was nearly zero, thus approximating the zero lift condition.

The wing design module of the BDAP program was then used to calculate the span-optimized loading distribution and the corresponding camber surface. This was achieved by optimizing the candidate loading distributions which are constant in the chordwise direction (loadings 1-5) in the presence of the flat-roof-top loading. As was the case for the wing designed for minimum-drag-due-to-lift (Section 3.3), it was observed that the elliptical loading (#5) was the most heavily weighted, and the mid-span loading (#4) was the most lightly weighted.

Next, the flat-roof-top camber surface was determined by bypassing the optimization routine of BDAP and simply finding the surface required to obtain the flat-roof-top loading distribution. In this procedure, the lift coefficient increment produced by the flat-roof-top loading, $C_{L_{f.r.t.}}$, was used as the design lift coefficient.

Table 4.1: Lift Contributions of Surface Portions for Wings in Parametric Study

Wing ID	λ	AR	$C_{L_{f.r.t.}}$ flat-roof-top portion	$C_{L_{span-opt}}$ span-optimized portion
W015	0.0	1.5	-0.00836	0.08836
W020	0.0	2.0	-0.00756	0.08756
W025	0.0	2.5	-0.00746	0.08746
W115	0.1	1.5	-0.00831	0.08831
W120	0.1	2.0	-0.00761	0.08761
W125	0.1	2.5	-0.00765	0.08765
W215	0.2	1.5	-0.00841	0.08841
W220	0.2	2.0	-0.00777	0.08777
W225	0.2	2.5	-0.00777	0.08777
W315	0.3	1.5	-0.00858	0.08858
W320	0.3	2.0	-0.00812	0.08812
W325	0.3	2.5	-0.00816	0.08816

$C_{L_{f.r.t.}}$ had been identified by the design program in the spanwise-optimization process and should be near zero.

The pressure distributions exhibited by the two wing portions, including the thickness pressures, are shown in Figures 4.5 and 4.6 for the baseline planform. In these figures, the two are evaluated at their respective lift coefficient increments, which are defined by the relationship

$$C_{L_{des}} = C_{L_{span-opt}} + C_{L_{f.r.t.}}$$

Thus, the sum of the lift coefficients in Figures 4.5 and 4.6 is equal to the design lift coefficient 0.08. The lift increments of the two camber surface portions for all of the wings presented in this paper are listed in Table 4.1.

Once the two portions of the camber surface were determined, they were combined linearly with the thickness distribution to define the final flat-roof-top spanwise-optimized wing (Figure 4.7). This wing was then evaluated and the total pressure distribution is shown in Figure 4.8.

As previously suggested, the airfoil section at the root of each wing designed by this procedure was rotated such that the the three most inboard sections would have a linear relationship in twist. The baseline HLFC wing, after being modified in such a way, is shown in Figure 4.9, and the airfoil sections are illustrated in Figure 4.10. The wing with the modified twist at the root was then re-evaluated, and as shown in Figure 4.11, the pressure distribution was not significantly degraded by this modification.

5 Parametric Study of the Wing Design Methods

A parametric analysis involving several arrow-wing planforms was conducted in an attempt to identify the effects that aspect ratio, AR, and taper ratio, λ, may have on the desirability of designing wings for HLFC. The study was conducted at a Mach number of 2.0, since the effect of camber on minimum drag-due-to-lift decreases at higher Mach numbers. A family of twelve wings of varying planform shape was developed with a common reference area, leading edge sweep, and airfoil thickness profile. As in the baseline example of Chapters 4 and 5, the reference planform area was chosen to be 8000 ft^2 for all of the wings. The leading edge sweep was chosen to be 67°, placing the entire wing at least 7° behind the Mach cone. This results in a subsonic Mach number of 0.78 normal to the leading edge. In this study, the same NACA-64 series airfoil thickness profile with a maximum thickness ratio of 4% that was employed in the baseline design was used on all of the wings. Aspect ratio was varied from 1.5 to 2.5 and taper ratio was varied from 0.0 to 0.3. This variation was selected to envelop the range of simple arrow-wing shapes of interest for supersonic HLFC. The resulting family of planforms is shown in Figure 5.1 and their dimensions are listed in Table 5.1.

Each of these planforms was cambered, as the baseline wing was, using both the minimum drag-due-to-lift method described in Chapter 3, and the HLFC design procedure of Chapter 4. The aerodynamic performances of the wings were then calculated using the methods outlined in Chapter 2, and the results of these evaluations follow.

5.1 Zero Lift Wave Drag

The wave drag of each wing was, as discussed in Chapter 2, assumed to be independent of the camber definition. Thus, the wave drag of each cambered wing could be approximated by the value for an uncambered wing of the same thickness distribution,

Table 5.1: Dimensions of Planforms in Parametric Study[a]

Wing ID	λ	AR	b	c_r	c_t	$\bar{c}$	$y_{\bar{c}}$	$x_{\bar{c}}$
W015	0.0	1.5	109.54	146.06	0.00	97.37	18.26	67.35
W020	0.0	2.0	126.49	126.49	0.00	84.33	21.08	70.75
W025	0.0	2.5	141.42	113.14	0.00	75.42	23.57	74.38
W115	0.1	1.5	109.54	132.78	13.28	89.33	19.92	69.25
W120	0.1	2.0	126.49	114.99	11.50	77.36	23.00	73.52
W125	0.1	2.5	141.42	102.85	10.29	69.19	25.71	77.87
W215	0.2	1.5	109.54	121.72	24.34	83.85	21.30	71.14
W220	0.2	2.0	126.49	105.41	21.08	72.62	24.60	76.10
W225	0.2	2.5	141.42	94.28	18.85	64.95	27.50	81.02
W315	0.3	1.5	109.54	112.35	33.71	80.09	22.47	72.96
W320	0.3	2.0	126.49	97.30	29.19	69.36	25.95	78.47
W325	0.3	2.5	141.42	87.03	26.11	62.04	29.01	83.85

---

[a] All dimensions in feet.

Common Dimensions for All Wings:

$S = 8000\ ft^2$, $\Lambda_{le} = 67°$, $\frac{t}{c} = 4\%$, $\frac{r}{c} = .1136\%$.

allowing for the wave drag to be calculated for only twelve wings (shown in Figure 5.1).

Analysis showed that the wave drag decreased with increases of both taper ratio and aspect ratio (Figure 5.2). This is attributed mostly to the reduced volume of the wings with higher λ and AR. The reduction in near-field wave drag associated with increasing λ from 0.0 to 0.3 varied from 7-14% at AR's of 1.5 and 2.5, respectively. The reduction in wave drag associated with increasing AR from 1.5 to 2.5 also varied from 7-14% at λ's of 0.0 and 0.3, respectively. The maximum difference in wave drag seen between any two wings was about 20%. All of the values that have been quoted here were obtained from the near-field analysis, but as shown in Figure 5.3, the far-field method provided very similar results.

5.2 Skin Friction Drag

The turbulent skin friction drag was also assumed to have no *direct* dependence on the camber definition, thus the small effect that camber has on the wetted area of the wing is neglected. However, for wings which are not assumed to have fully turbulent boundary layers (i.e. those designed for HLFC), the friction drag is very dependent on the camber definition by means of its influence over the boundary layer type (laminar, turbulent, or mixed). In this study, the wings which had been optimized for minimum drag-due-to-lift with no boundary layer considerations were assumed to possess fully turbulent boundary layers. The wings that were designed by the HLFC design method to produce flat-roof-top pressure distributions were evaluated assuming varying amounts of laminar flow on the upper surface and fully turbulent flow on the lower surface.

On a simple HLFC wing, suction panels could extend along the entire span of the wing for some given ranges in percent chord length. For example, an HLFC wing might incorporate one suction panel from the leading edge to 10% chord length and then another panel between 30% and 40% chord length. The flow would then be stabilized for the first 10% by suction and a region of natural laminar flow would follow until the flow was again stabilized by the second suction strip at 30% of the local chord length. Another region of natural laminar flow would then extend for some length behind the second strip. If it is assumed that the local mass flow rate through a suction panel is proportional to its width, and that the degree of stabilization accomplished is proportional to this mass flow, then the increase of the local critical

Reynolds number due to the suction could be assumed to be proportional to the local panel width. On an HLFC wing such as the one described above, the local width of each suction panel is proportional to the local chord length, so the degree of stabilization, or length of natural laminar flow following a given suction panel is proportional to the local chord length. On this basis, a study was conducted in which the fraction of the chord length which was laminar was assumed to be constant over the entire span of the HLFC wings. The results of this study are discussed in Section 5.2.1. Calculations were also made assuming a constant upper surface critical Reynolds number over the span of the wing, which will be discussed in Section 5.2.2.

5.2.1 C_{D_f} Based on Critical $\frac{x}{c}$

Friction drag estimates for the baseline wing (as calculated by the method of Section 2.3) are shown in Figure 5.4 assuming several quantities of laminar flow on the upper surface in percent chord length, where the skin friction drag is plotted as a function of Mach number. The results indicate that at this flight condition, if laminar flow could be maintained over the entire upper surface, there would be approximately a 45% reduction in skin friction drag as compared to a fully turbulent wing. It can also be seen that the relationship between the amount of laminar flow and the friction drag is nearly linear for any given Mach number. This is also true for the other wings in the study.

Figures 5.5 and 5.6 show the skin friction drag at cruise for both fully turbulent wings and wings having upper surfaces which are entirely laminar. The figures show that for the fully laminar and fully turbulent wings friction drag increases with taper ratio and also with aspect ratio. The increase with taper ratio appears to be relatively small, having a maximum effect on friction drag of less than 2.5% for any given aspect ratio. Increasing the aspect ratio from 1.5 to 2.5 has slightly more influence, increasing the friction drag by only 3.5-4.2%. A more prominent feature of this figure is that the difference in the drag coefficient values caused by a change in AR is constant for all of the wings with a given λ. The difference between the $AR = 1.5$ and $AR = 2.5$ curves is about .00011 for the turbulent wings, and .00007 for the wings with fully laminar upper surfaces.

Laminar flow can probably be induced over no more than 75% of the chord length on the upper surface without requiring a very high mass flow through the suction panels. In any case, beyond this point several physical disturbances such as flap hinge lines would probably exist on an HST and would surely trip the boundary layer unless further stabilization methods were employed. This assumed value corresponds to a friction drag reduction of about 34%. However, it will also be assumed that a 7° turbulent wedge exists at the wing-fuselage abutment. This value is based on extrapolated subsonic data, as given by Fisher in reference 22. If there were any wing leading-edge discontinuities, the area bounded by a 14° wedge with its apex at the discontinuity would also be assumed turbulent due to the spanwise disturbance. This assumption was applied to all of the wings, and new friction drag estimates were obtained. A wing with a higher λ will have less of its surface area submerged in the turbulent wedge than a wing having a low λ (holding aspect ratio constant). The introduction of the wing root turbulent wedge into the calculations greatly reduced the influence of taper ratio on friction drag (Figure 5.7). The reduction in turbulent wedge area is even more pronounced with an increase in AR. The upper series of curves in Figure 5.7 represent the wings with 75% laminar flow on the upper surface and a 7° turbulent wedge originating at the apex. The figure shows that the turbulent wedge assumption actually reverses the effect of λ and reduces the combined effects of λ and AR on skin friction drag to less than 2%. For the planforms with low λs, the influence of AR is essentially eliminated altogether. When this case is compared to the fully turbulent wings, friction drag reductions of about 28-32% are observed.

5.2.2 C_{D_f} Based on Critical *Re*

If it were assumed that the flow were to transition from laminar to turbulent at some specified critical Reynolds number as is assumed on many *natural* LFC applications, instead of at a given percent $\frac{x}{c}$, it would surely change the predicted dependence of friction drag on AR. A given Re_{crit} would translate into a much smaller area of laminar flow on a low AR (short span) wing than on a high AR wing, resulting in a higher friction drag. Taper ratio, λ, would also show a greater influence on the friction drag calculations, since on highly tapered wings much of the potential area of laminar flow may lie behind the trailing edge on the outboard part of the wing. Thus, if Re_{crit} were to be increased, the calculated drag would decrease until it reached a minimum at the Re which corresponds to a critical length equal to the root chord length.

Figure 5.8 shows the effect that the assumed critical Reynolds number, Re_{crit}, has on the calculated friction drag for the baseline wing. The friction drag coefficient, C_{D_f}, is shown to decrease as Re_{crit} is increased to a value of about 213 million, beyond which the upper surface is fully laminar and C_{D_f} remains constant. This is because, at the cruise conditions, an Re_{crit} of 213 million corresponds to a critical length of 115 feet (the root chord length). Using Figure 5.8, it was found that an Re_{crit} of about 82 million was required for the calculated C_{D_f} of the baseline wing to be the same as when 75% laminar flow and a 7° turbulent wedge were assumed. This Re_{crit} was assumed for all of wings, and the corresponding C_{D_f}'s were calculated.

Figure 5.9 shows the friction drag coefficients as they were calculated using this assumption, along with those (from Figure 5.7) calculated using the previous section's assumptions. It shows that calculating C_{D_f} based on a critical Reynolds number predicts a markedly greater dependence on both AR and λ. It may also be noted that the trends are nearly equal and opposite to those predicted assuming a critical $\frac{x}{c}$ with no turbulent wedge.

5.3 Drag-Due-to-Lift

The drag-due-to-lift was evaluated using the lift analysis module of the BDAP program. This is the only drag increment that is affected directly by the camber of the wing, thus it is the only drag increment other than the friction drag which is affected by the method of wing design.

Figure 5.10 illustrates the differences in the drag polars of the baseline planform cambered using the two design methodologies. This figure includes the wave drag increment, which is the same for both wings, and the drag-due-to-lift increment, which of course varies with the camber definition. As indicated by the shapes of the drag polars, the wing designed for minimum drag-due-to lift has been cambered in such a way as to give it an advantage at nearly all positive lift conditions, as well as at the design lift coefficient of 0.08.

The drag-due-to-lift increments at cruise ($C_L = .08$) for all of the wings are shown in Figure 5.11 and also in Table 5.2.

From Figure 5.11, the influence of taper ratio, λ, and aspect ratio, AR, on the drag-due-to-lift can be seen. As expected, the wings with a higher AR have a definite aerodynamic advantage. The HLFC wings are seen to gain very little by increasing the taper ratio above about 0.15. This may suggest that there is a penalty involved with attempting to maintain a flat-roof-top pressure distribution over longer lengths at the wing tips.

From an analysis of this data, it was found that the differences in drag-due-to-lift caused by the design method are primarily dependent on taper ratio. At taper

Table 5.2: Drag-Due-to-Lift at Cruise of Wings in Parametric Study

Planform ID	$C_{D_{HLFC}}$	$C_{D_{min-ddtl}}$	$\frac{C_{D_{min-ddtl}}}{C_{D_{HLFC}}}$
W015	0.00299	0.00274	0.9164
W020	0.00263	0.00238	0.9005
W025	0.00231	0.00212	0.9177
W115	0.00285	0.00256	0.8982
W120	0.00246	0.00222	0.9002
W125	0.00222	0.00199	0.8964
W215	0.00234	0.00249	0.8755
W220	0.00242	0.00211	0.8719
W225	0.00216	0.00190	0.8796
W315	0.00287	0.00243	0.8467
W320	0.00240	0.00206	0.8583
W325	0.00211	0.00180	0.8531

ratios of 0.0 (a pointed wing tip), the optimized wings have about 9% less drag-due-to-lift than the HLFC wings; and, at taper ratios of 0.3, the optimized wings have over 17% less drag-due-to-lift than their HLFC counterparts. The percent difference in drag-due-to-lift was found to have a nearly linear relationship with the λ values between 0.0 and 0.3.

5.4 Total Drag

The total drag, as explained in Chapter 2, was taken to be the sum of the wave drag, skin friction drag, and the drag-due-to-lift. Figure 5.12 shows the total drag estimates for all of the wings at the cruise conditions. The estimates for the HLFC wings are shown using each of the assumptions of sections 5.2.1 and 5.2.2. It may be observed from these curves that, in the analysis of the total drag, the differences between using a critical $\frac{x}{c}$ and a critical Re in the C_{D_f} calculations for the HLFC wings were greatly diluted.

Of interest to this study was the effect that aspect ratio and taper ratio had on the drag reductions that could be obtained by the HLFC system. Figure 5.13 shows this effect as a percent drag reduction as compared to the turbulent wings designed for minimum drag-due-to-lift. The results are shown assuming an Re_{crit} of 82 million and a critical $\frac{x}{c}$ of 75% with a 7° turbulent wedge. From this, we see that the assumption of an Re_{crit} predicts a greater effect of both AR and λ on total drag reduction.

With the assumption of a critical $\frac{x}{c}$, it was found that the taper ratio had little effect on the percent drag reduction. In other words, the ratio of the total drag coefficients was nearly constant for a given aspect ratio. However, this ratio was found to be dependent on the aspect ratio. The drag reductions range from slightly less than 6% to nearly 9% for aspect ratios of 1.5 to 2.5, respectively. Assuming an Re_{crit} of 82 million, the drag reductions ranged from slightly less than $5\frac{1}{2}$% up to $8\frac{1}{2}$ - 10% for aspect ratios of 1.5 to 2.5, respectively. That is, higher aspect ratio wings are likely to realize greater benefits from HLFC systems than low aspect ratio wings. Thus, they are more receptive to such a design method. In general, wings with an AR of 2.5 can realize up to twice the drag reduction through the use of an HLFC system as a wing with an AR of 1.5.

6 Concluding Remarks

This study was undertaken in an attempt to quantify the aerodynamic benefits and penalties involved in designing wings to accommodate hybrid laminar flow control (HLFC) systems. To do this, it was first necessary to establish a feasible process for the preliminary design of such wings. For this study, an upper surface pressure distribution favorable to laminar flow was investigated, and a slightly simplified one was developed to accommodate the limitations of the linear theory used in the pressure calculations and wing design. An existing design program was used to calculate the wing lifting load distribution which would combine with the thickness pressures to produce this desired upper surface pressure profile while maintaining a spanwise lifting distribution designed to minimize drag-due-to-lift. Linear theory was then used to define the camber definition required for the lifting load distribution.

This design methodology and a method used to camber wings for minimum drag-due-to-lift were applied to several planform shapes in an attempt to evaluate the effects of aspect ratio and taper ratio on the potential performance benefits of HLFC wings. The skin friction drag was shown to be almost independent of AR and λ for the HLFC wings at about 30% lower values than those for the turbulent wings, if it were assumed that 75% of the chord length on the upper surface were laminar except for a 7° wedge at the root. The friction drag was also calculated for all of the wings assuming a critical Reynolds number of 82 million. With this assumption, C_{D_f} was predicted to decrease with increases in either AR or λ. The differences in C_{D_f} between the HLFC wings and their turbulent counterparts were also predicted to be much greater for the high AR and high λ wings.

It was also calculated that the wings designed for HLFC had 9-$17\frac{1}{2}$% more drag-due-to-lift than the corresponding wings designed for minimum drag-due-to-lift. This percentage was found to linearly increase with λ and to be relatively independent of AR. However, when this drag increment was combined with the wave drag and friction drag increments, the total drag benefit of the HLFC wings was mostly dependent upon the wing AR. This is because the unfavorable effects on drag-due-to-lift increase with λ at about the same rate as the beneficial effects on the skin friction drag (assuming 75% laminar flow) for the HLFC wings.

In conclusion, it is predicted that the total drag reductions accomplished by designing wings for HLFC, as opposed to designing them for minimum drag-due-to-lift, vary from $5\frac{1}{2}\%$ to nearly 9% based on a critical $\frac{x}{c}$ of 75% and from 5% to nearly 10% based on Re_{crit}=82 million depending on the wing λ and AR. Experimental investigation is required to resolve which of these assumptions pertaining to the location of transition to turbulence is more correct. It was also found that this relationship was primarily dependent on AR and, in general, wings with higher aspect ratios are likely to realize greater benefits from HLFC systems than low aspect ratio wings.

The next logical step in this study would be to implement higher order methods in the inverse design process. But until such methods are made available, progress must be made with the tools at hand. The present research is not intended as a substitute for higher order methods; it is hoped instead that it will augment interest in the advancement of such methods so that they may be used in future studies and to verify the present results.

7 References

1. Coen, Peter G. : *Technology Sensitivity Studies for a Mach 3.0 Civil Transport.* AIAA-88-4469, Sep. 1988.

2. Jackson, Charlie M. ; Morris, Charles M. : *Unique Research Challenges for High-Speed Civil Transports.* NASA TM 100490, Aug. 1987.

3. Walkley, Kenneth B. ; Martin, Glen L. : *Aerodynamic Design and Analysis of the AST-200 Supersonic Transport Configuration Concept.* NASA CR 159051, 1977.

4. Martin, Glen L. ; Walkley, Kenneth B. : *Aerodynamic Design and Analysis of the AST-202, -204, and -206 Blended Wing-Fuselage Supersonic Transport Configuration Concepts.* NASA CR 159223, 1978.

5. Robins, A. Warner ; Dollyhigh, Samuel M. ; Beisner, Fred L. ; Geiselhart, Karl ; Martin, Glen L. ; Shields, E. W. ; Swanson, E.E. ; Coen, Peter G. ; Morris, Shelby J. Jr. : *Concept Development of a Mach 3.0 High Speed Civil Transport.* NASA TM-4058, Sep. 1988.

6. Dollyhigh, S. M. : *Theoretical Evaluation of High-Speed Aerodynamics for Arrow-Wing Configurations.* NASA TP-1358, Jan. 1979.

7. Harris, Roy V., Jr. : *An Analysis and Correlation of Aircraft Wave Drag.* NASA TM X-947, 1964.

8. Carlson, Harry W.; Mack, Robert J.; Barger, Raymond L. : *Estimation of Attainable Leading-Edge Thrust for Wings at Subsonic and Supersonic Speeds.* NASA TP-1500, Oct. 1979

9. Malik, M. R. : *COSAL - A Black-Box Compressible Stability Analysis Code for Transition Prediction in Three-Dimensional Boundary Layers.* NASA CR-165925, 1982.

10. Sommer, Simon C. ; Short, Barbara J. : *Free-Flight Measurements of Turbulent-Boundary-Layer Skin Friction in the Presence of Severe Aerodynamic Heating at Mach Numbers from 2.8 to 7.0.* NACA TN 3391, 1955.

11. Kuethe, Arnold M. : Chow, Chuen-Yen : *Foundations of Aerodynamics.* Fourth Edition, ©1986, by John Wiley & Sons, Inc.

12. Schlichting, Herman : *Boundary-Layer Theory.* Seventh Edition, ©1979, by McGraw-Hill, Inc.

13. Carlson, Harry W. : *Aerodynamic Characteristics at Mach Number 2.05 of a Series of Highly Swept Arrow Wings Employing Various Degrees of Twist and Camber.* NASA TM X-332, Oct. 1960.

14. Carlson, Harry W. : *Pressure Distributions at Mach Number 2.05 of a Series of Highly Swept Arrow Wings Employing Various Degrees of Twist and Camber.* NASA TN-D-1264, May 1962.

15. Middleton, W. D. ; Lundry, J. L. : *A System for Aerodynamic Design and Analysis of Supersonic Aircraft. Part 1 - General Description and Theoretical Development.* NASA CR-3351, Dec. 1980.

16. Middleton, W. D. ; Lundry, J. L.; Coleman, R. G. : *A System for Aerodynamic Design and Analysis of Supersonic Aircraft. Part 2 - User's Manual.* NASA CR-3352, Dec. 1980.

17. Middleton, W. D. ; Lundry, J. L.; Coleman, R. G. : *A System for Aerodynamic Design and Analysis of Supersonic Aircraft. Part 3 - Computer Program Description.* NASA CR-3353, Dec. 1980.

18. Middleton, W. D. ; Lundry, J. L.; Coleman, R. G. : *A System for Aerodynamic Design and Analysis of Supersonic Aircraft. Part 4 - Test Cases.* NASA CR-3354, Dec. 1980.

19 Kulfan, R. M. ; Sigalla, A. : *Real Flow Limitations in Supersonic Airplane Design.* AIAA 16th Aerospace Sciences Meeting, Huntsville, Alabama, Jan. 1987

20. Pfenninger, Werner ; Viken, Jeffrey K. ; Vemuru, Chandra S. ; Volpe, Gruseppe : *All Laminar SC LFC Airfoils with Natural Laminar Flow in the Region of the Main Wing Structure.* AIAA-86-2625, Oct. 1986.

21. Pfenninger, Werner ; Vemuru, Chandra S. : *Suction Laminarization of Highly Swept Supersonic Laminar Flow Control Wings.* AIAA/AHS/ASEE Aircraft Design, Systems and Operations Meeting. Atlanta, Georgia, Sept 7-9, 1988.

22. Fisher, M. C. : *Spreading of a Turbulent Disturbance.* AIAA Journal, Vol.10, No. 7, pp.957-959, Jul. 1972.

23. *Research in Natural Laminar Flow and Laminar-Flow Control.* NASA Conference Publication 2487, Mar. 1987.

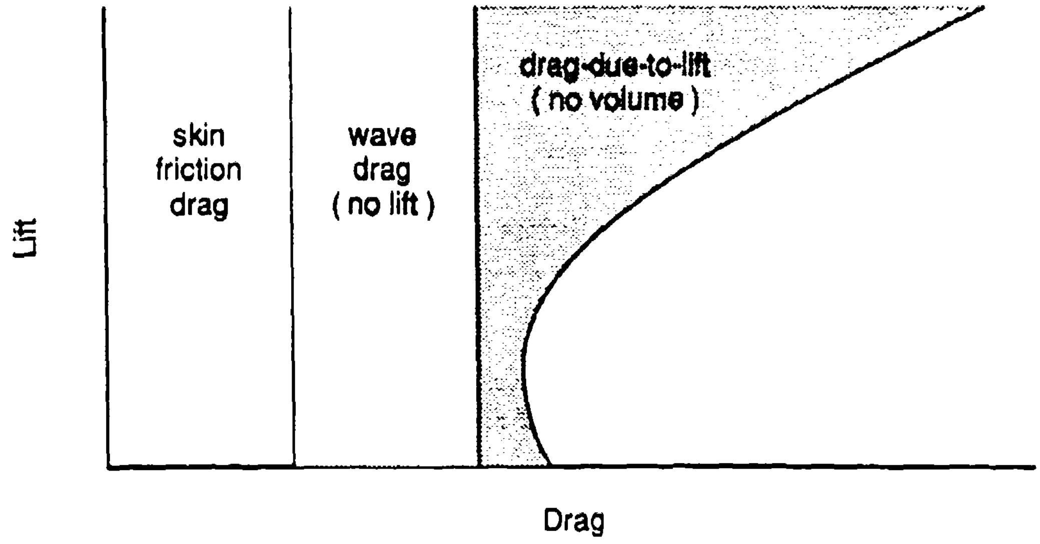

Figure 2.1 - Superposition Method of Drag Analysis

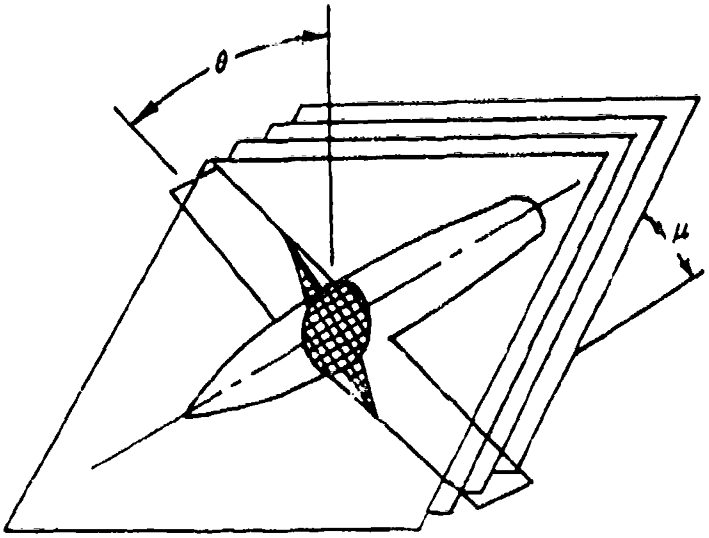

(a) series of Mach plane cuts used in the calculation of a single equivalent body

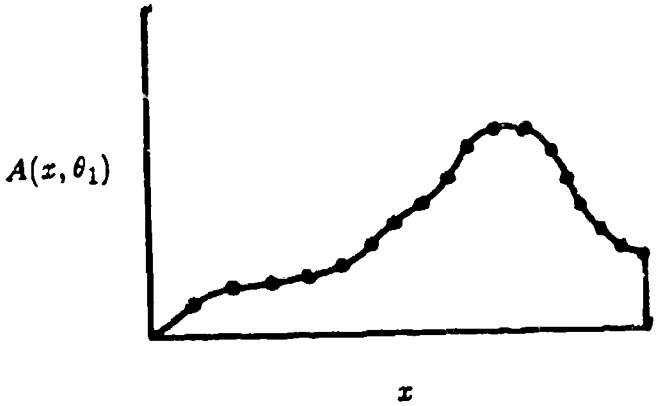

(b) equivalent-body area distribution for a sample $\theta = \theta_1$

Figure 2.2 - Far-Field Wave Drag Calculations

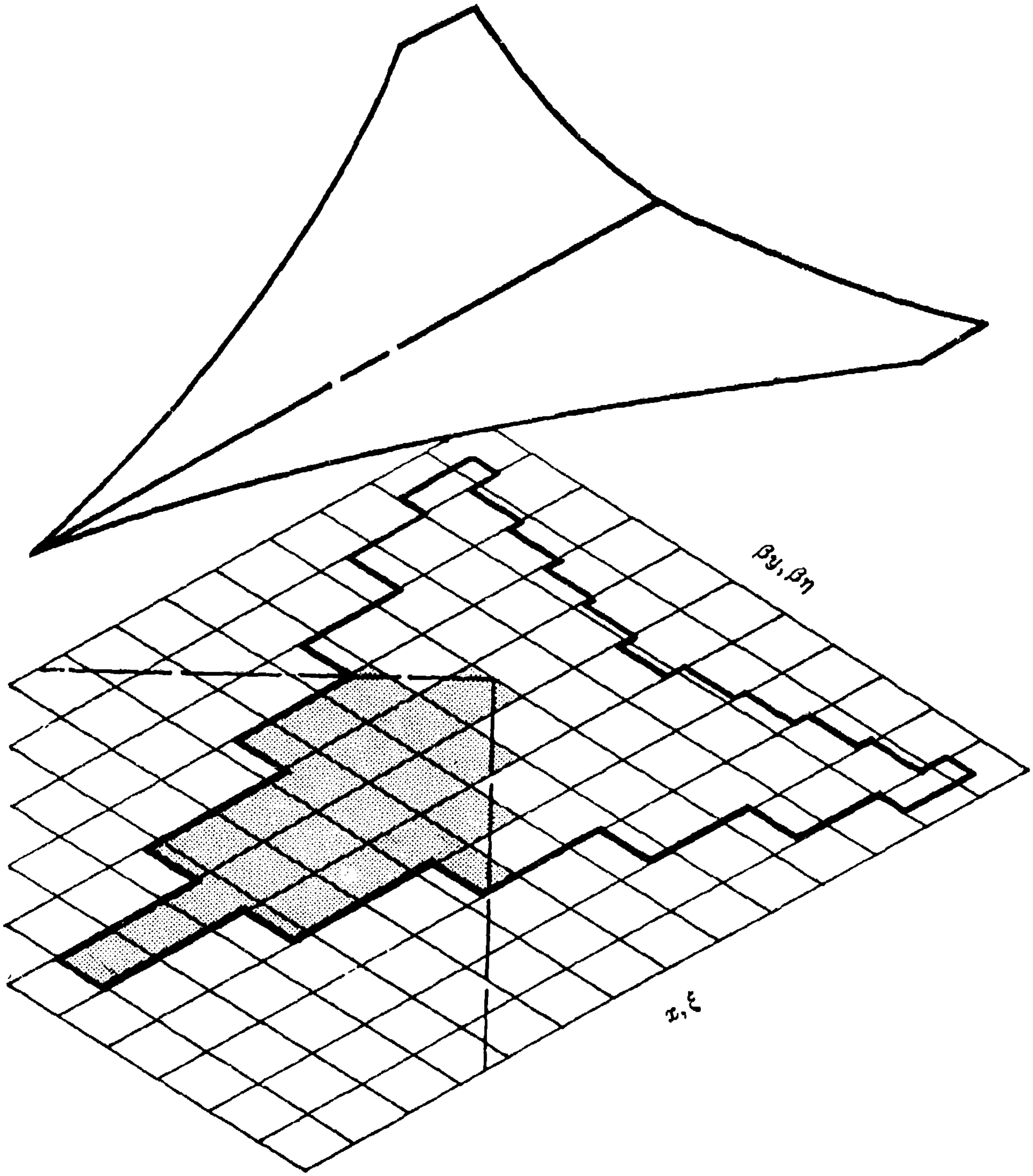

Figure 2.3 - Mach Box Computational Grid for Supersonic Aerodynamics

- K_T is a function of :
  - -Airfoil geometry
  - -Normal Mach number
  - -Reynolds number

- Attainable thrust factor, $K_T = \frac{c_t^*}{c_t}$
  - $K_T = 1.0 \rightarrow$ Attached flow
  - $K_T = 0.0 \rightarrow$ Vortex flow

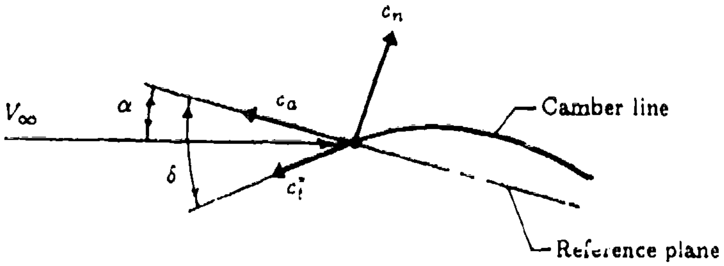

$$c_n = \frac{c_t}{\cos\Lambda_{le}} \sin(\cos^{-1}K_T - \delta)$$

$$c_a = -c_t \cos(\cos^{-1}K_T - \delta)$$

Figure 2.4 - Theory of Attainable Vortex Thrust

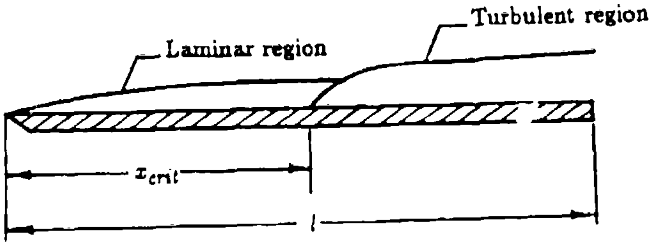

Figure 2.5 - Mixed Boundary Layer Schematic

$AR = 2.24$

$\Lambda_{le} = 70°$

$\frac{t}{c} = 3\% \ (circular\ arc)$

$S = 212.94\ in^2$

$\frac{b}{2} = 65.4\ in$

$\bar{c} = 13.0\ in$

* All dimensions in inches.

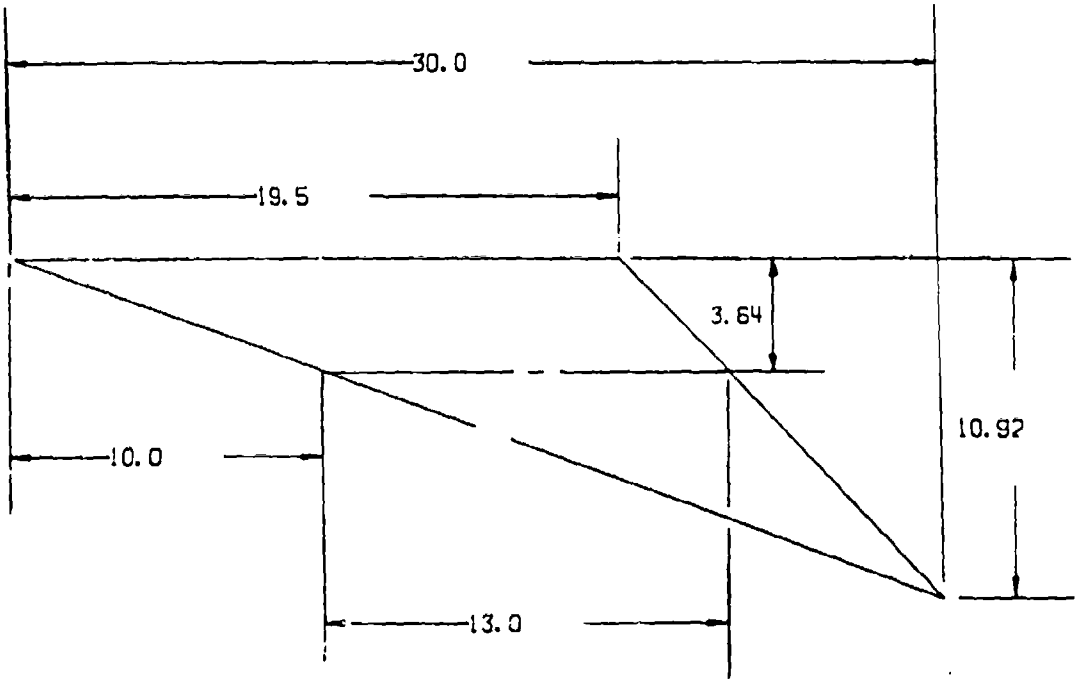

Figure 2.6 - Test Wing Planform Description

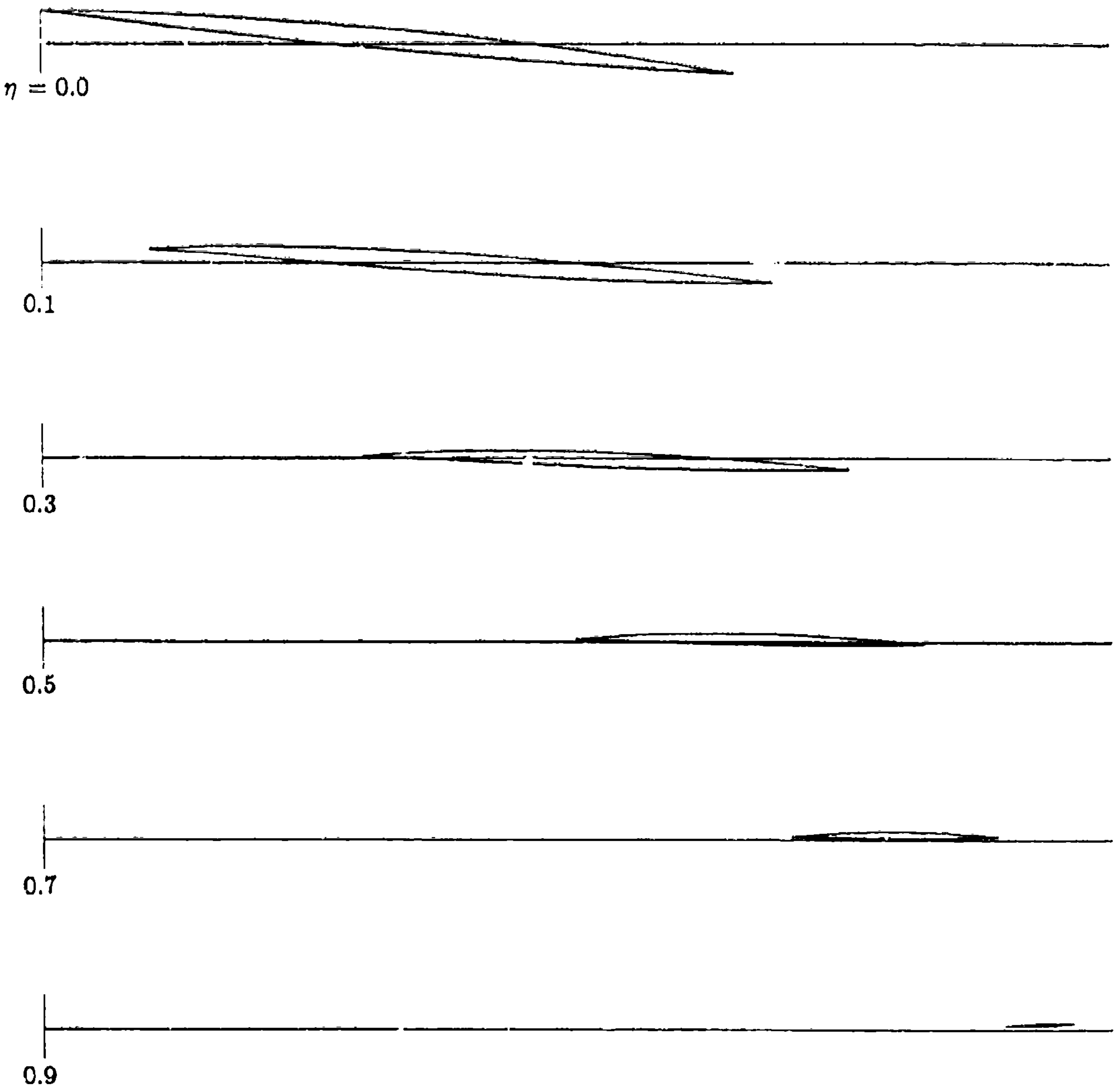

Figure 2.7 - Airfoil Sections for Test Wing

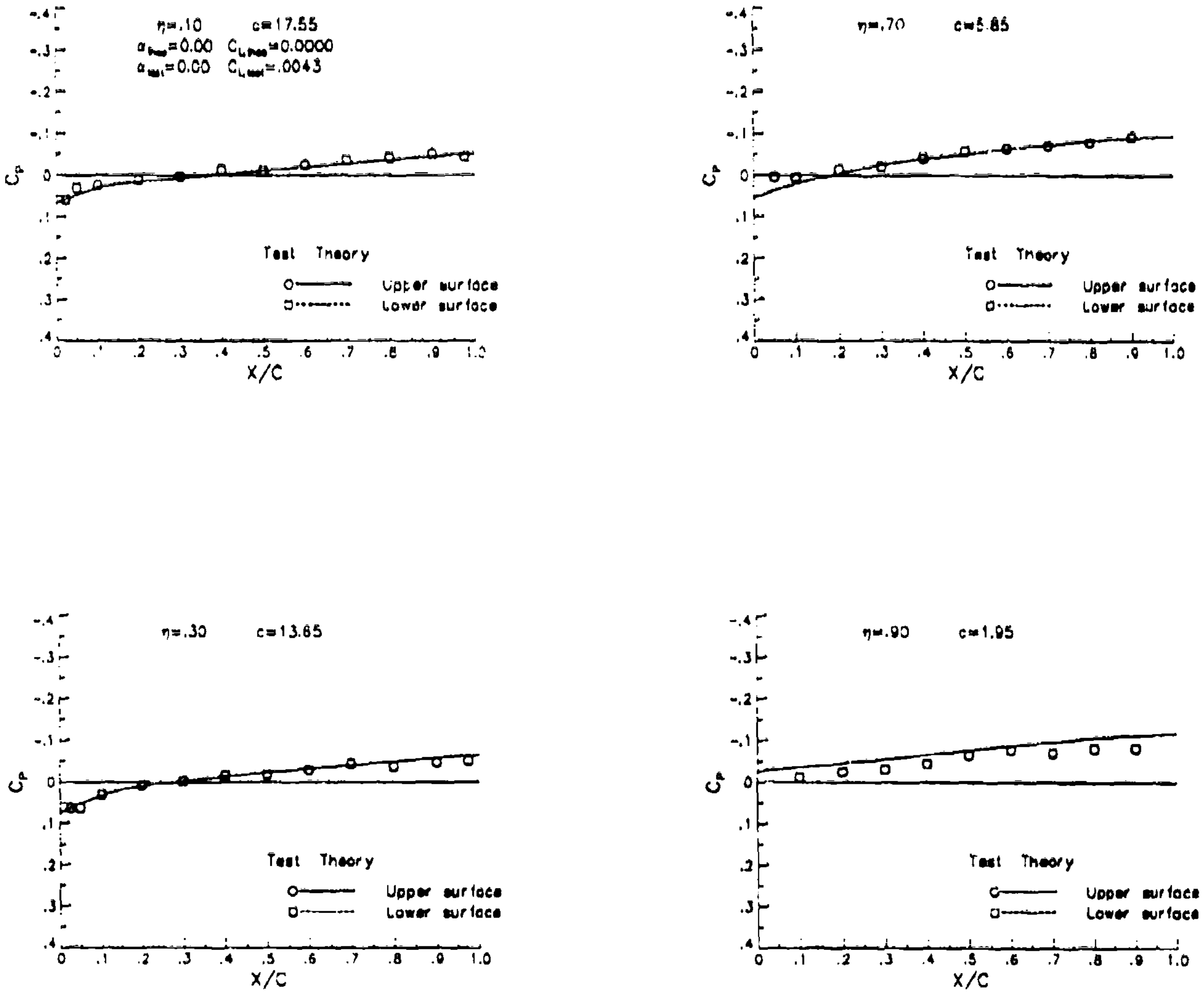

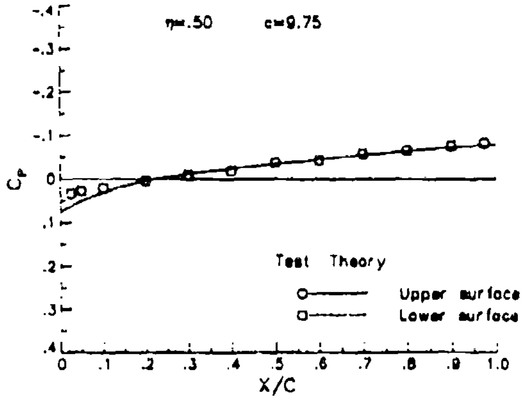

(a) Uncambered Wing : $\alpha = 0°$

Figure 2.8 - Comparison of Theoretical and Experimental Pressure Distributions

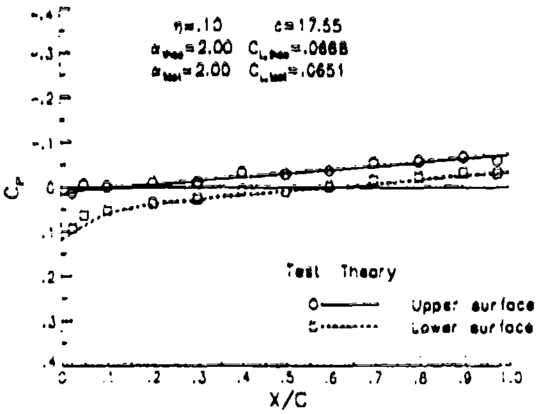

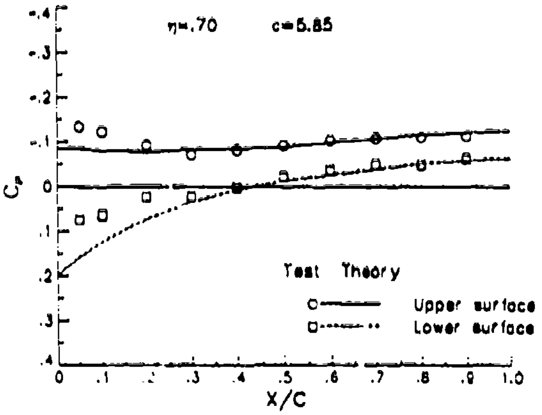

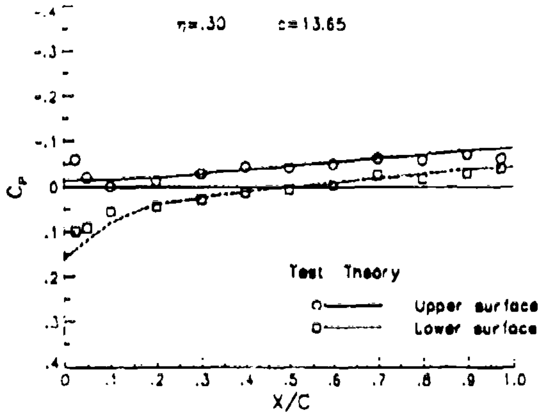

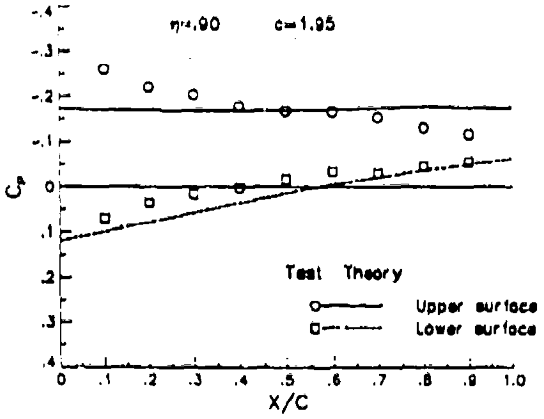

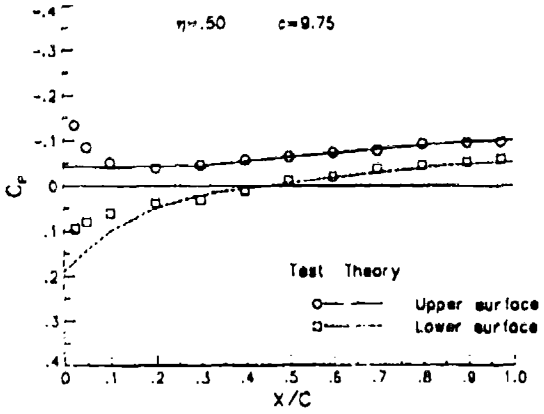

(b) Uncambered Wing : $\alpha = 2°$

Figure 2.8 - Continued

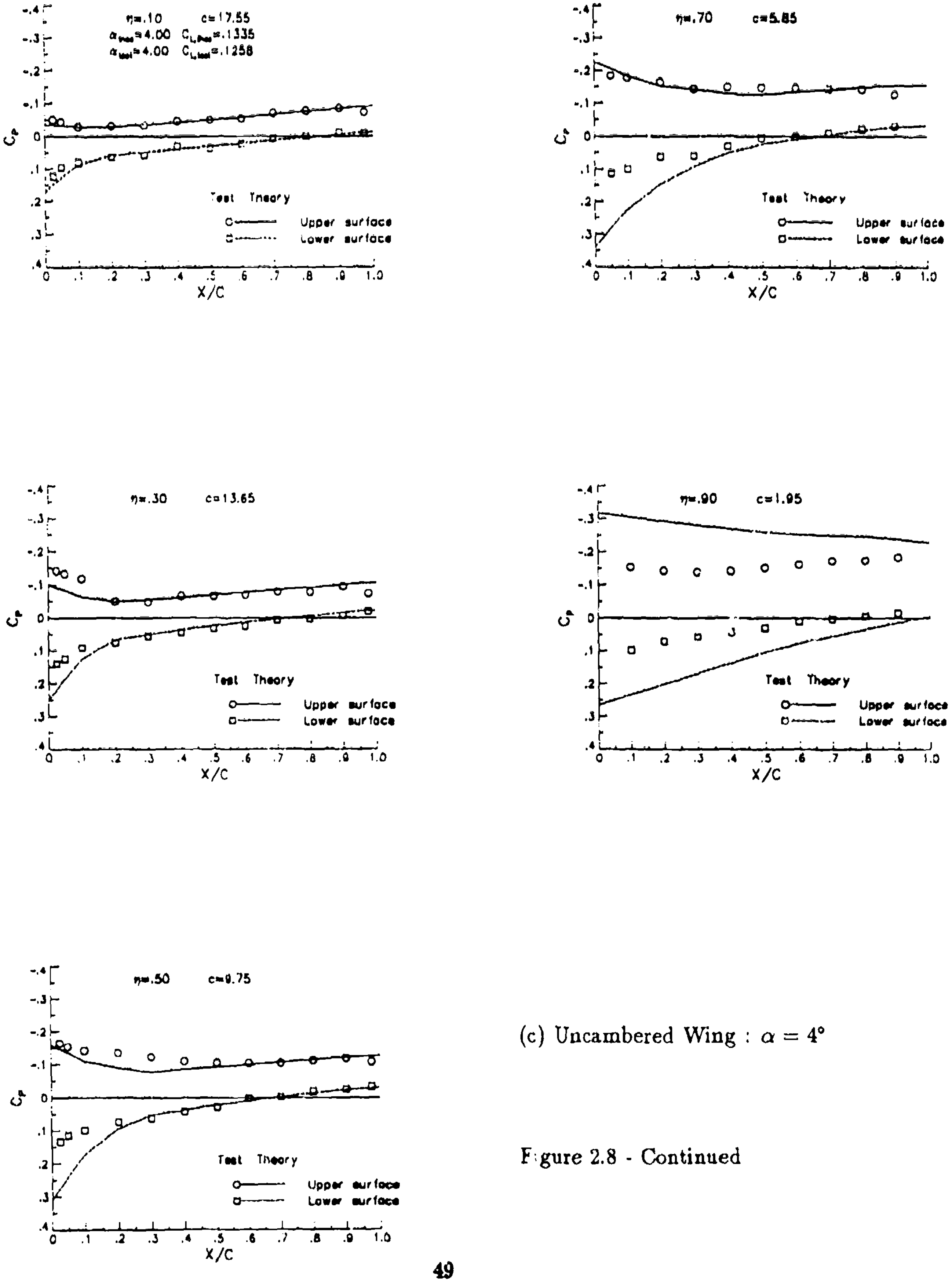

(c) Uncambered Wing : $\alpha = 4°$

Figure 2.8 - Continued

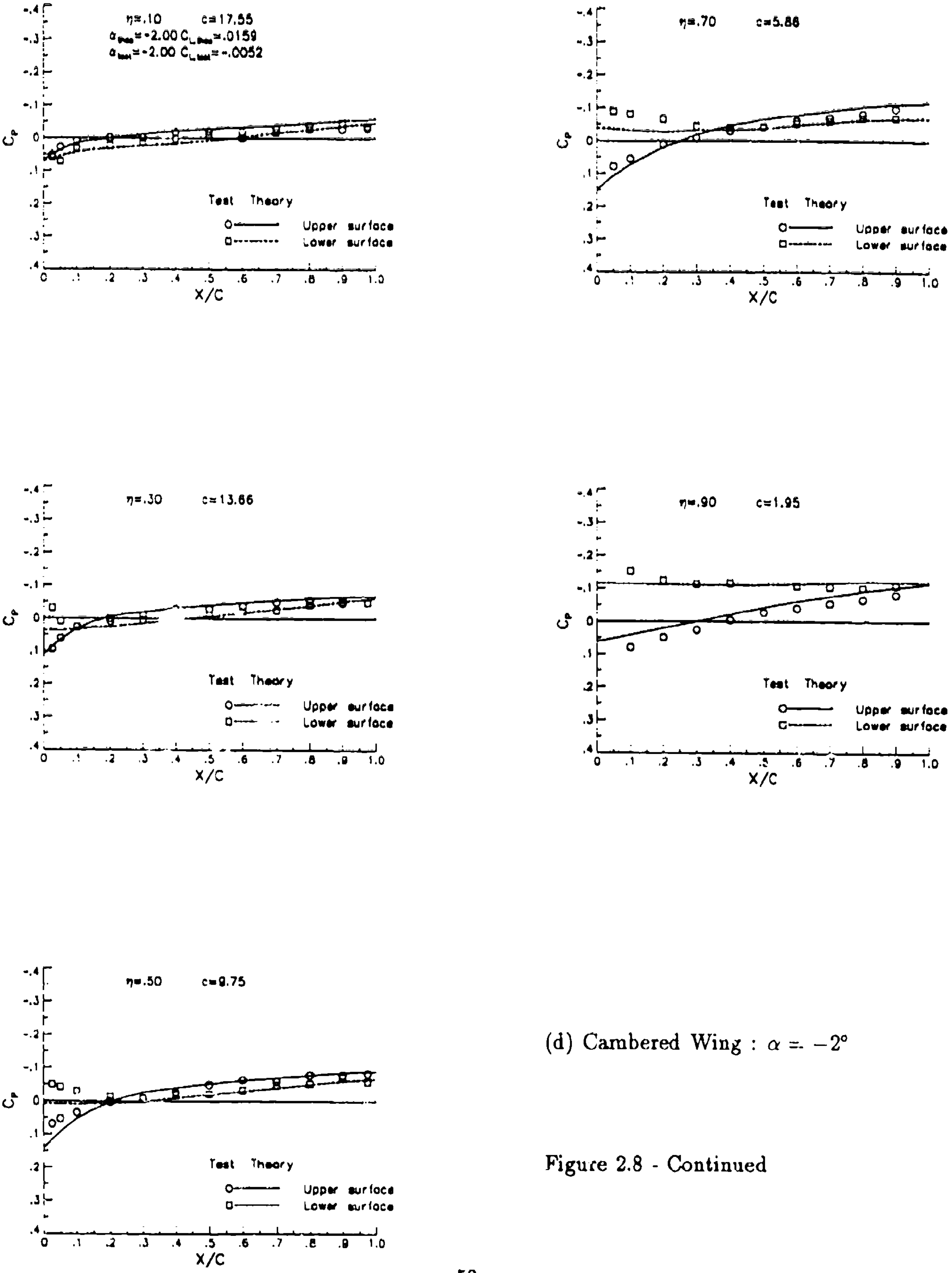

(d) Cambered Wing : $\alpha = -2°$

Figure 2.8 - Continued

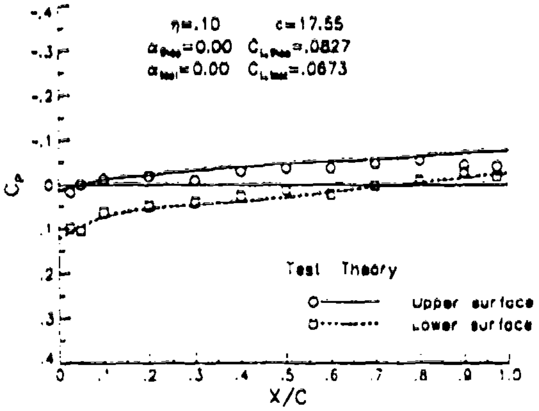

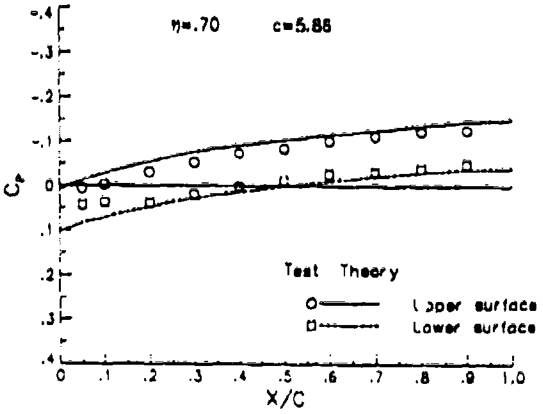

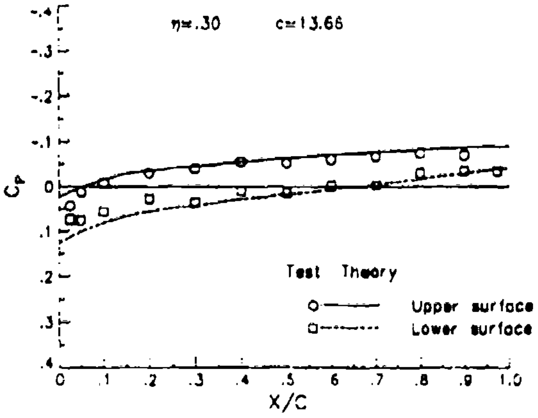

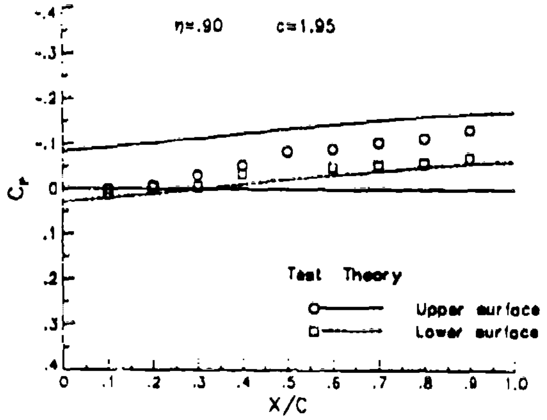

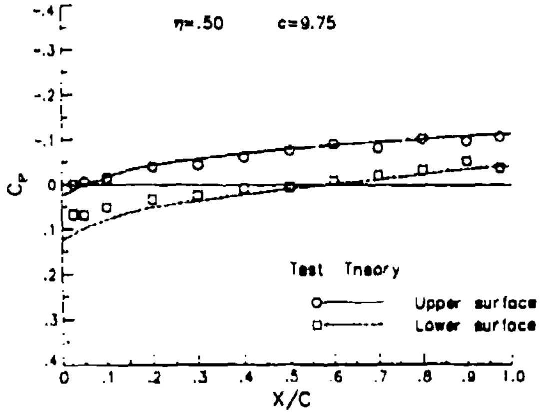

(e) Cambered Wing : $\alpha = 0°$

Figure 2.8 - Continued

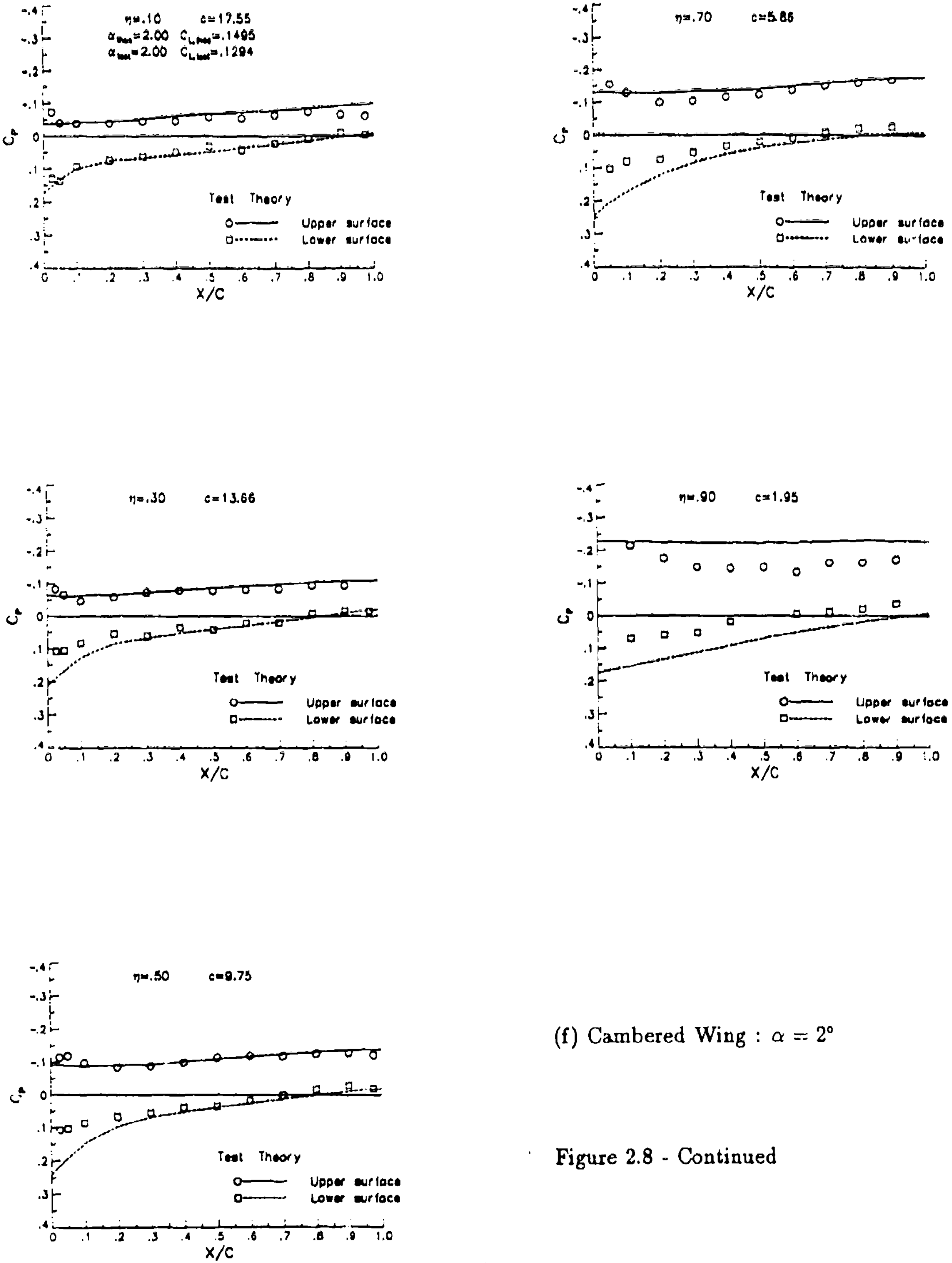

(f) Cambered Wing : $\alpha = 2°$

Figure 2.8 - Continued

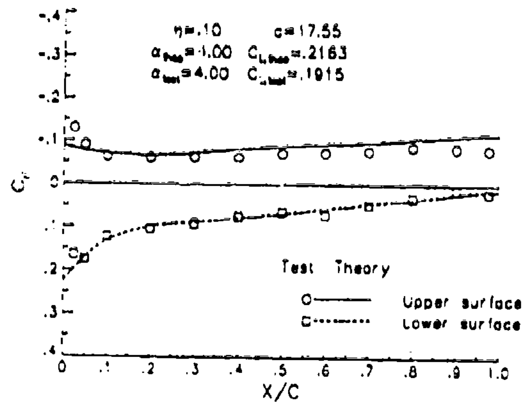

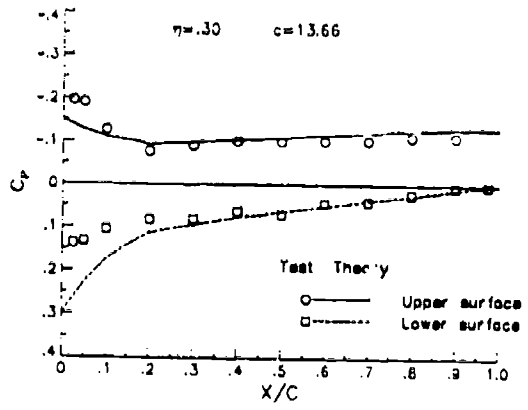

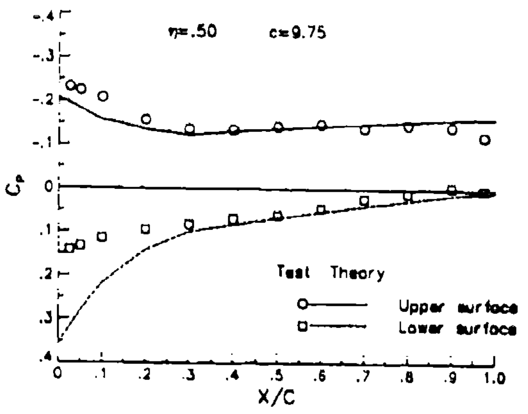

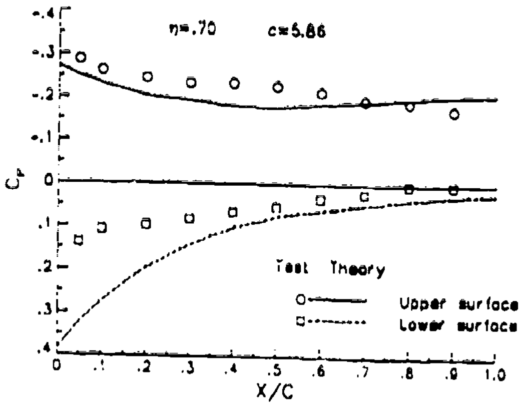

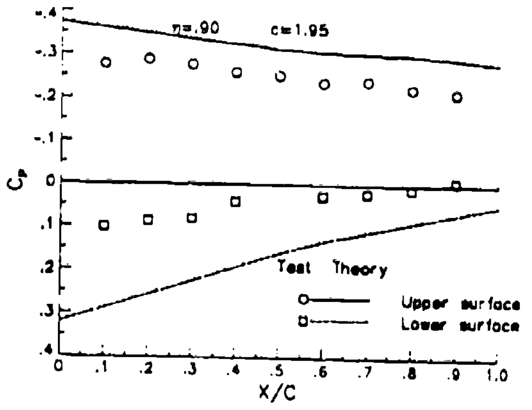

(g) Cambered Wing : $\alpha = 4°$

Figure 2.8 - Concluded

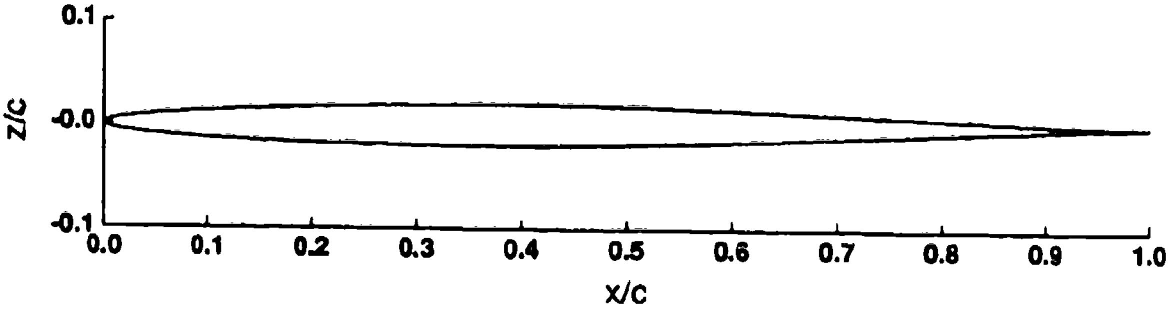

Figure 3.1 - NACA 64-004 Airfoil Thickness Profile

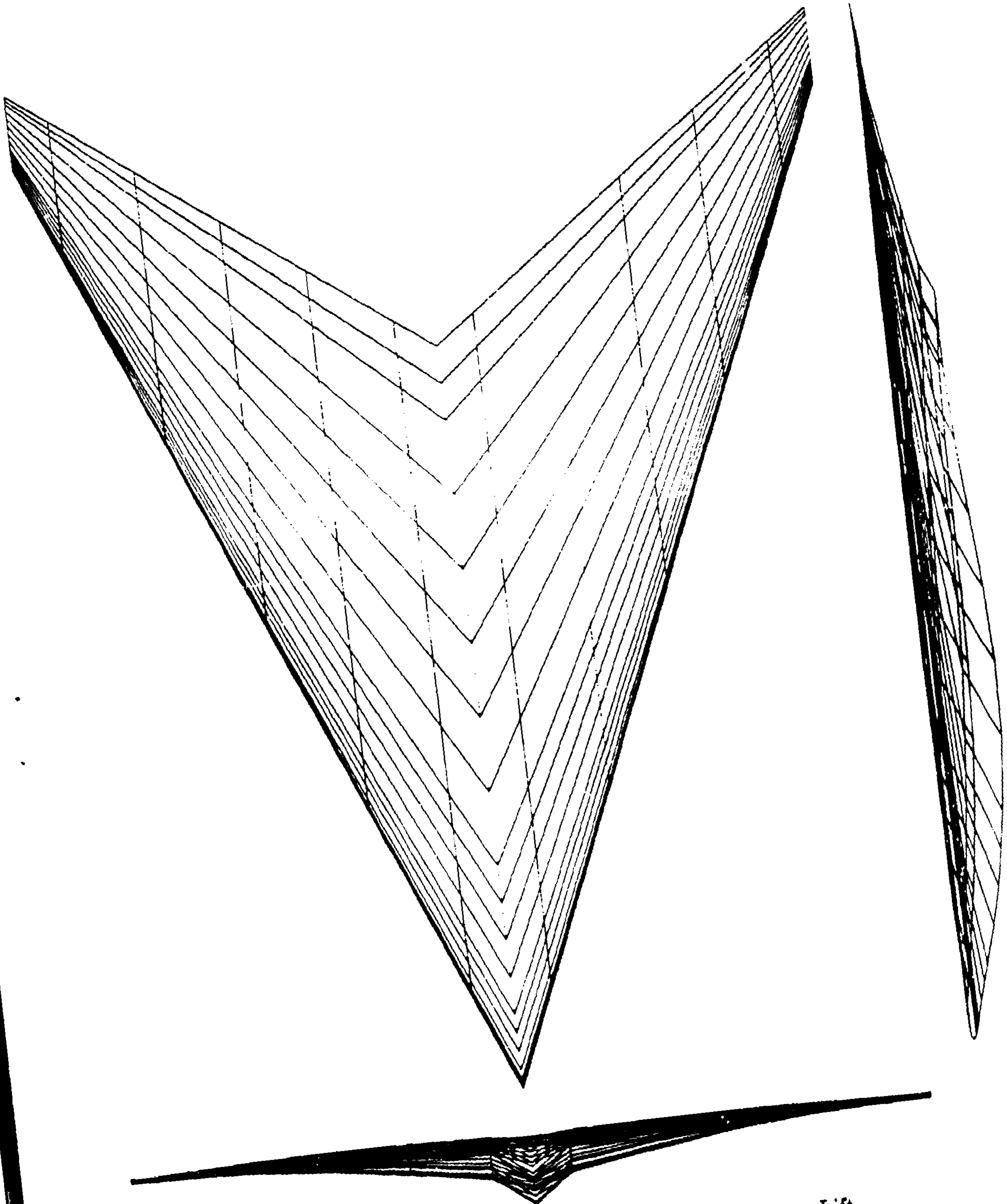

Figure 3.2 - Baseline Wing Designed for Minimum Drag-Due-to-Lift

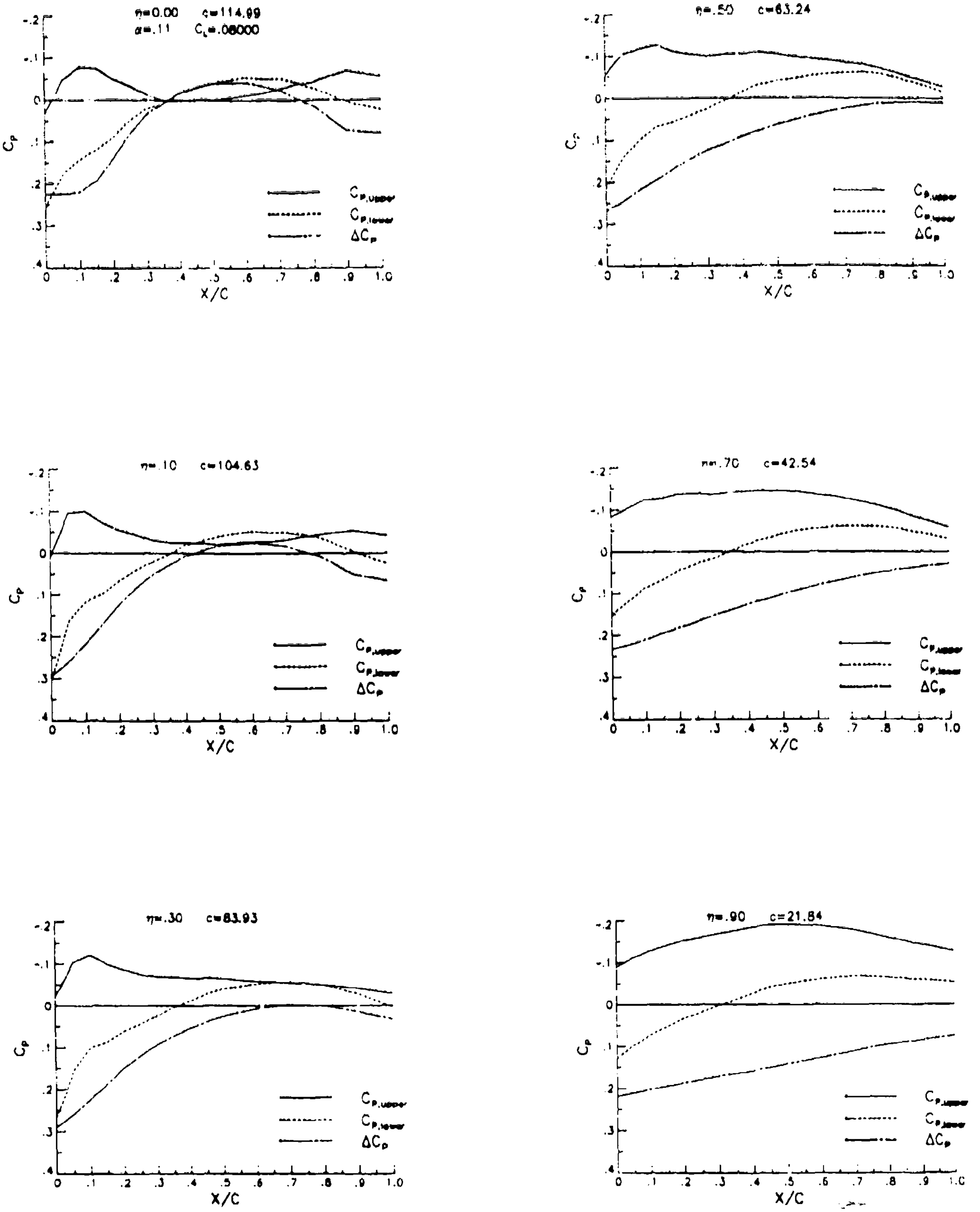

Figure 3.3 - Pressure Distribution on Baseline Wing Designed for Minimum Drag-Due-to-Lift

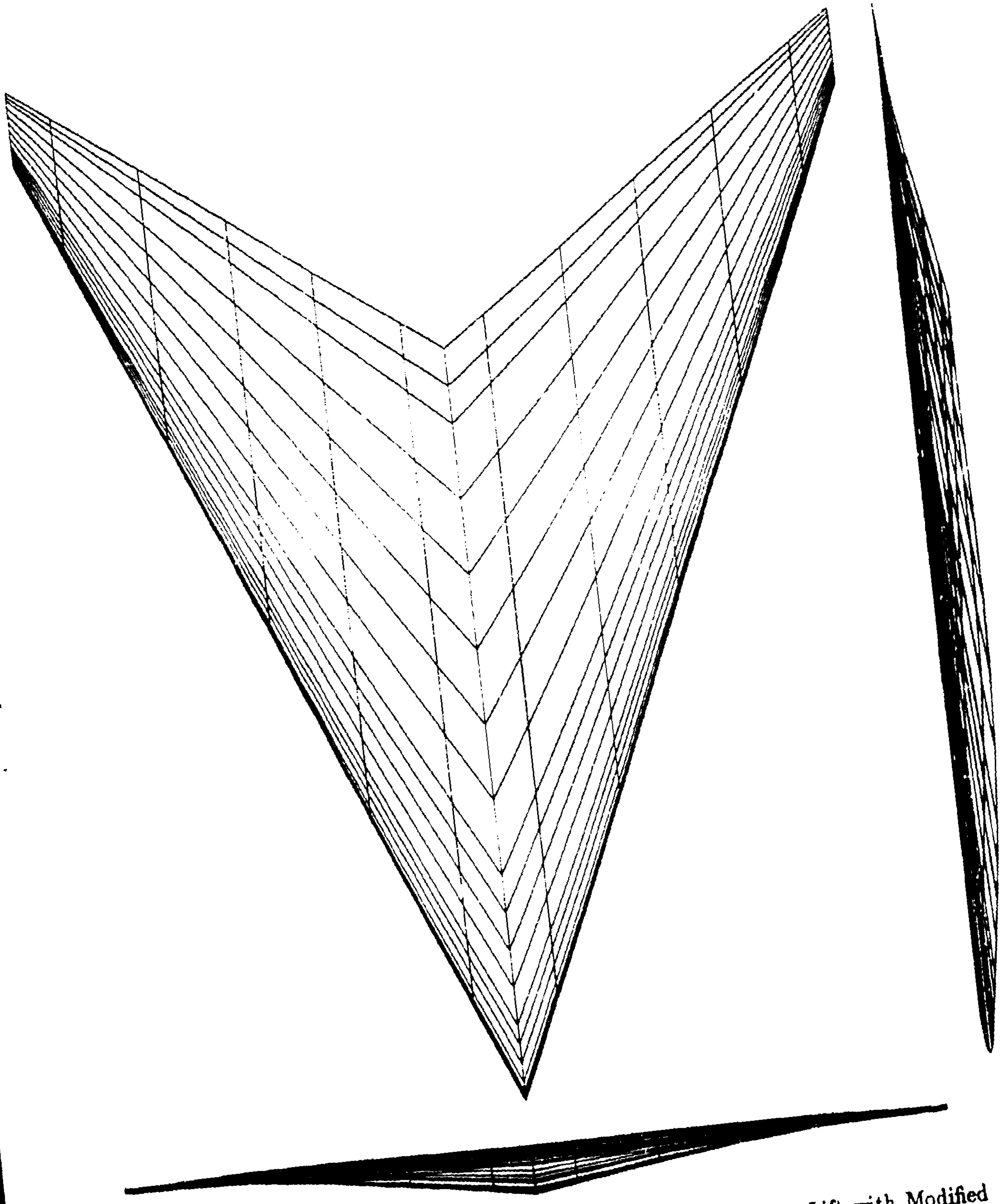

Figure 3.4 - Baseline Wing Designed for Minimum Drag-Due-to-Lift with Modified Root

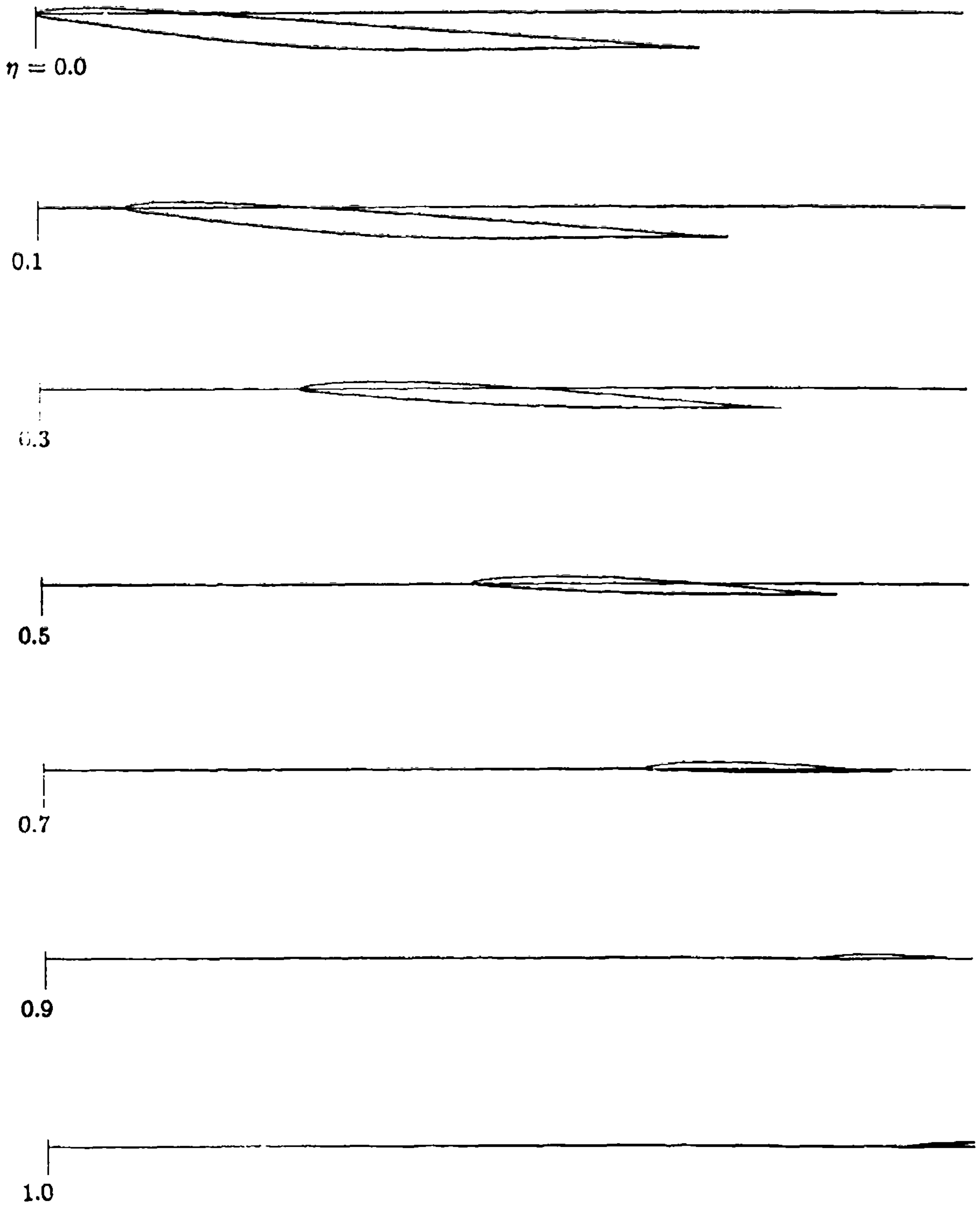

Figure 3.5 - Airfoil Sections for Baseline Wing Designed for Minimum D-D-T-L

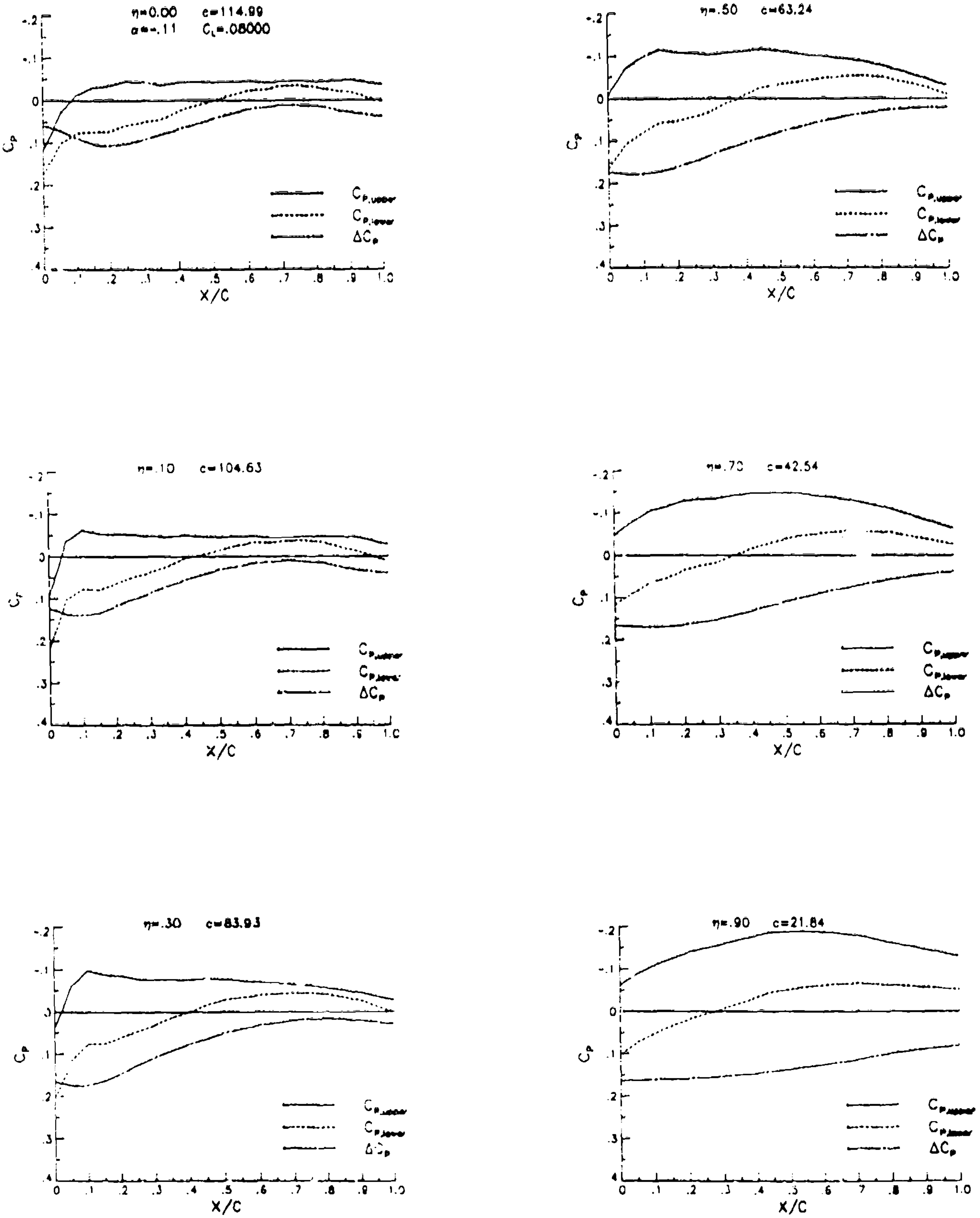

Figure 3.6 - Pressure Distribution on Baseline Minimum D-D-T-L Wing with Modified Root

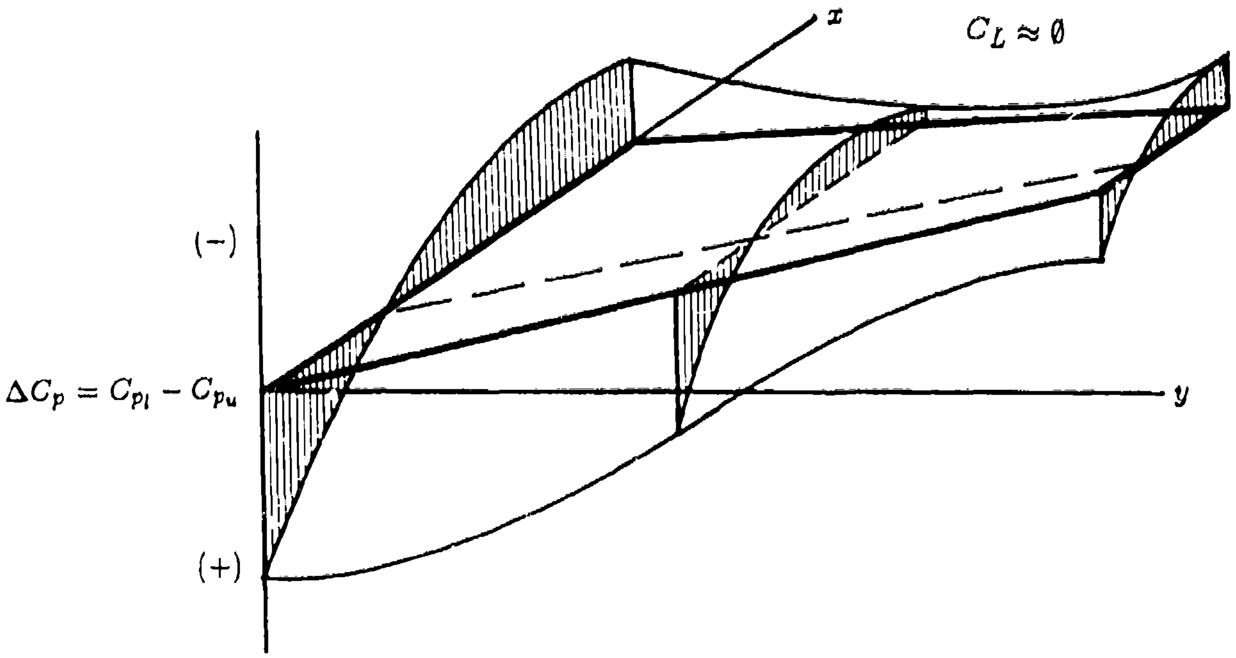

Figure 4.1 - Lifting Pressure Distribution on Flat-Roof-Top Camber Surface
(combines with thickness pressures to give a flat-roof-top C_p distribution)

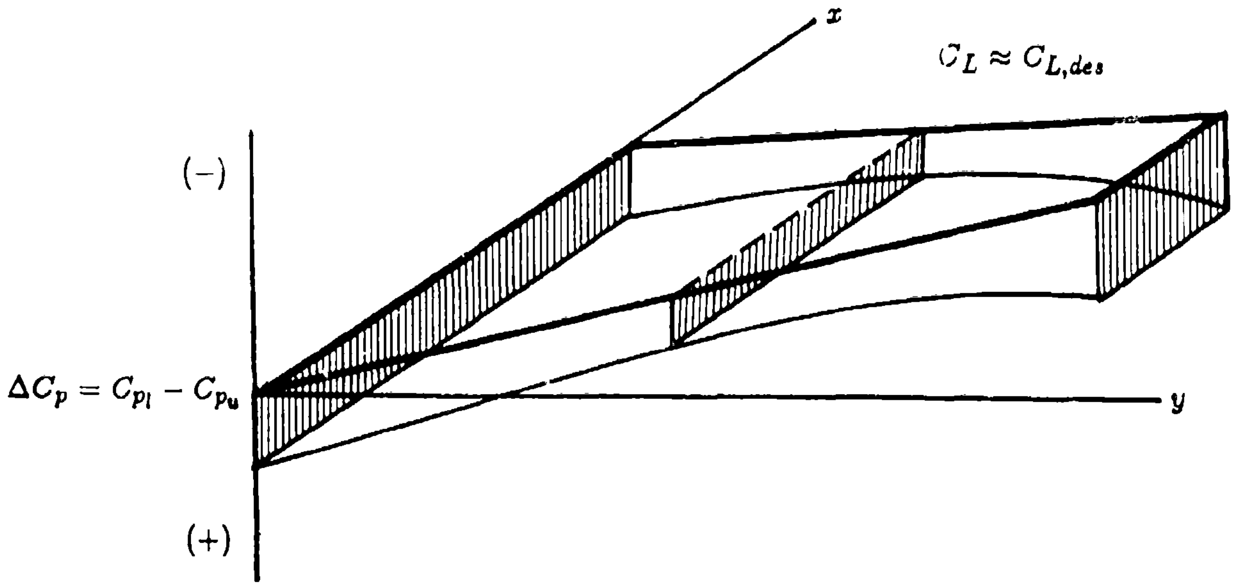

Figure 4.2 - Lifting Pressure Distribution on Span-Optimized Camber Surface
(optimized in the presence of the loading of figure 4.1)

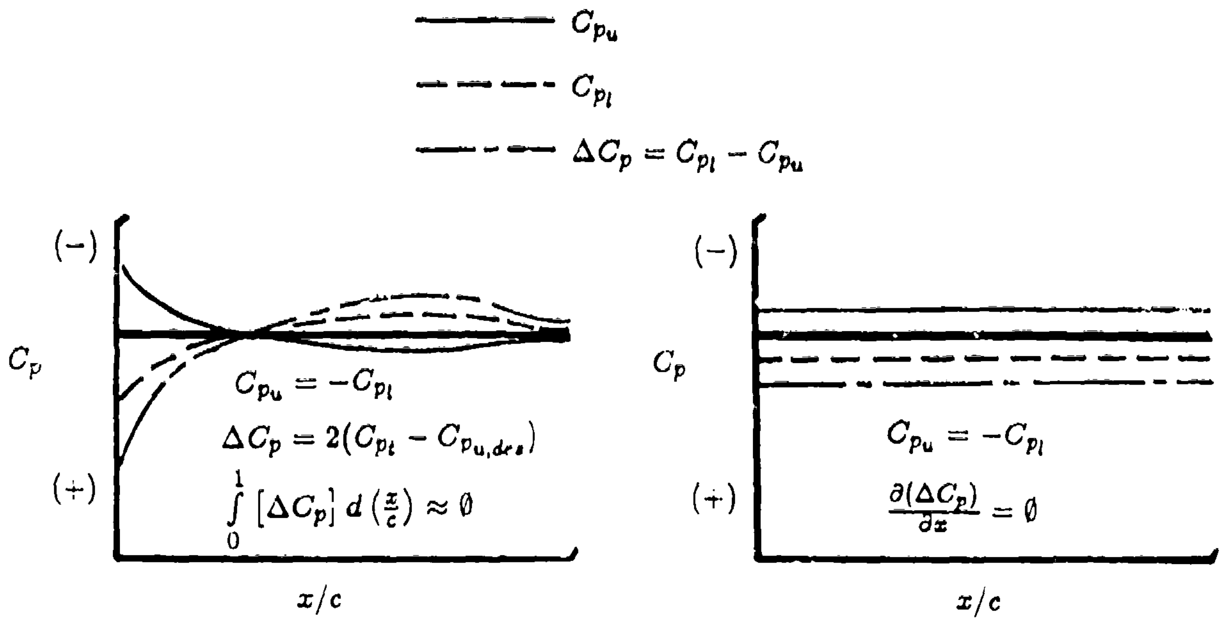

(a) Flat-Roof-Top Camber Surface

(b) Spanwise-Optimized Camber Surface

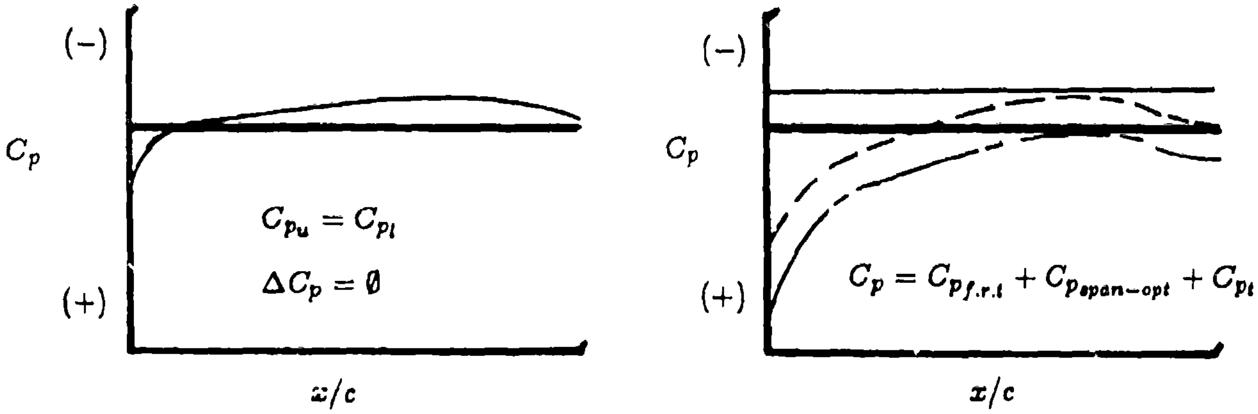

(c) Flat Wing with Thickness

(d) Final Flat-Roof-Top Wing Design

Figure 4.3 - Pressure Distributions on Inverse Design Portions and on the Final Flat-Roof-Top Wing

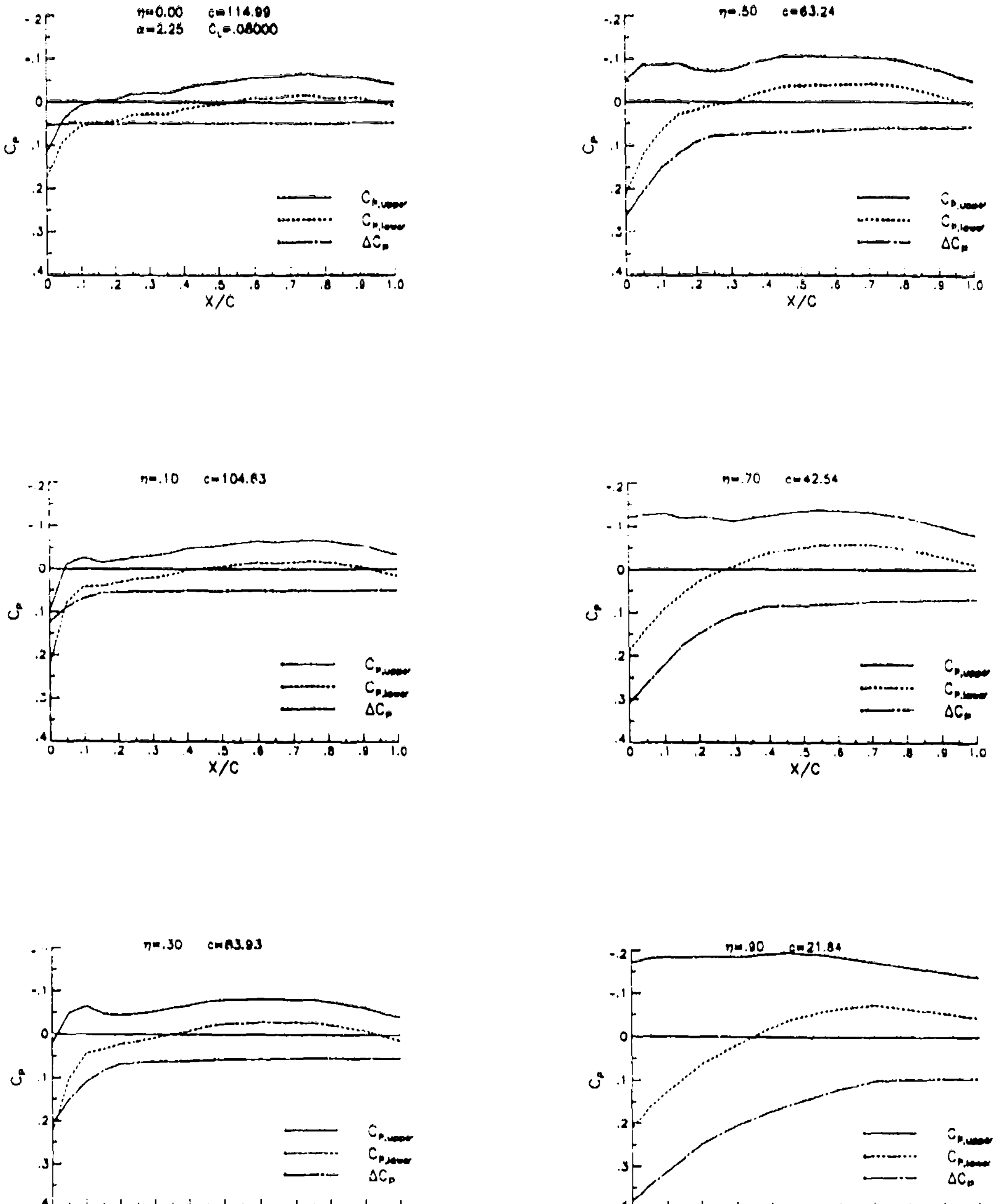

Figure 4.4 - Pressure Distribution on Uncambered Baseline Wing at Design Lift

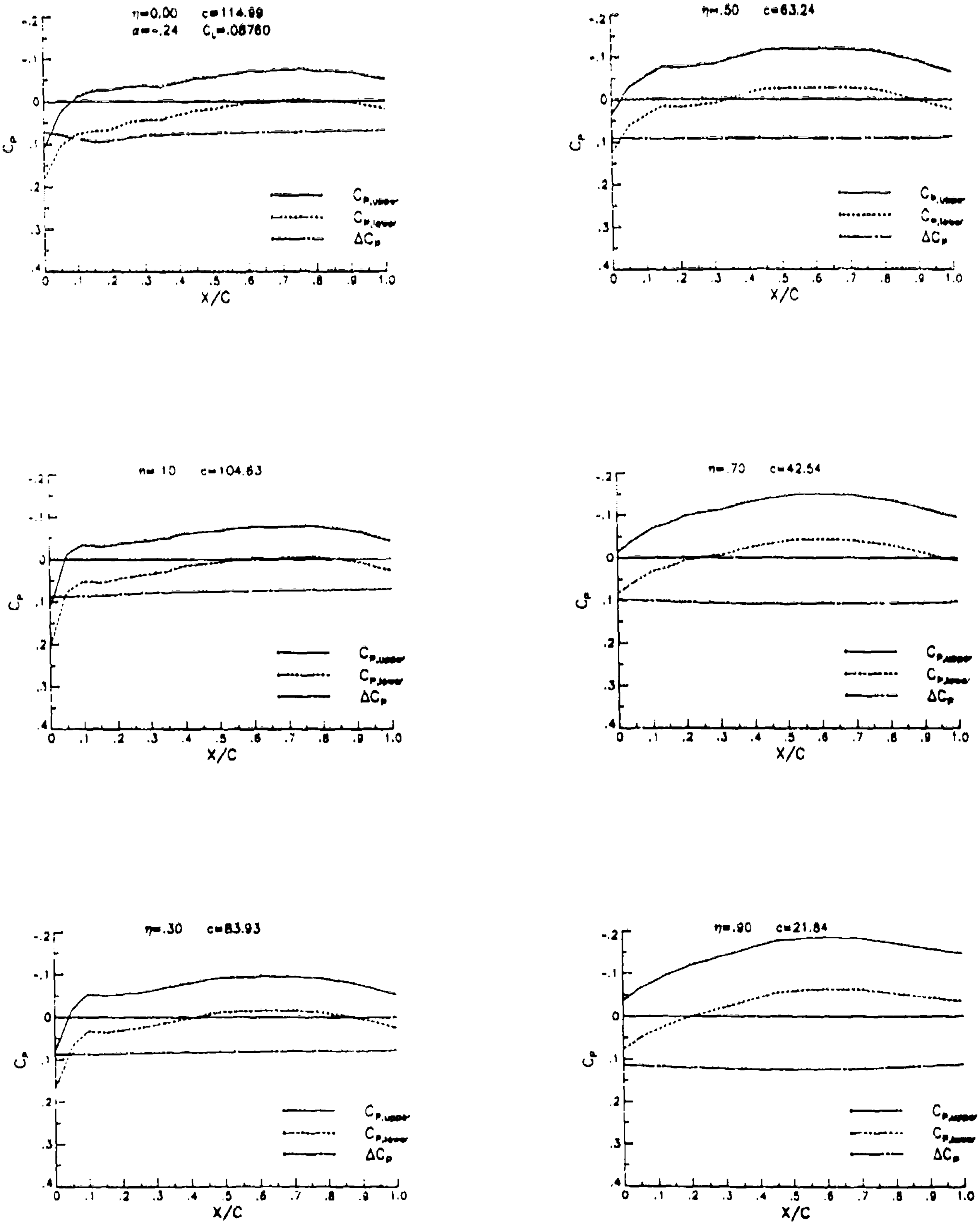

Figure 4.5 - Pressure Distribution on Span Optimized Portion of Baseline Wing

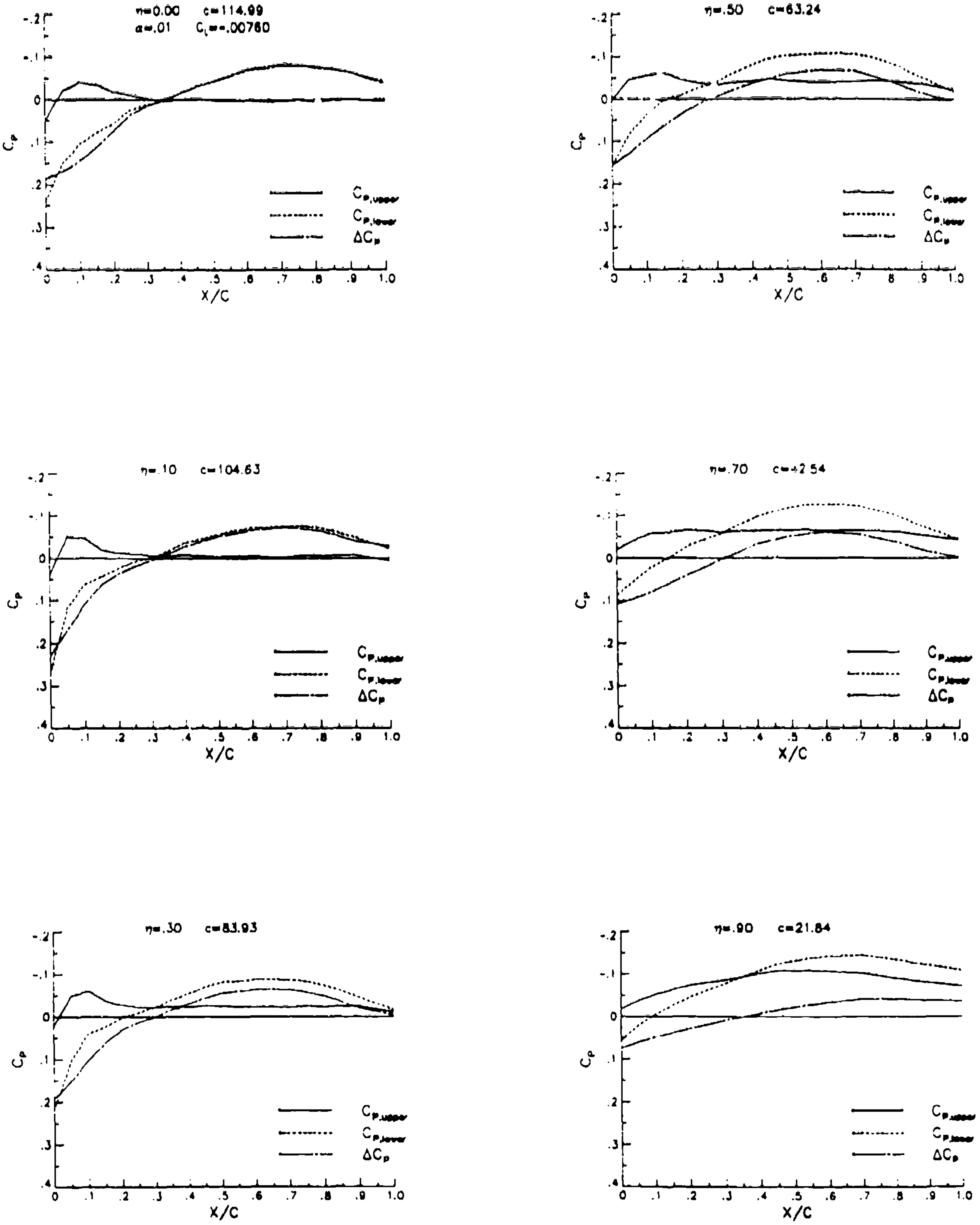

Figure 4.6 - Pressure Distribution on Flat-Roof-Top Portion of Baseline Wing

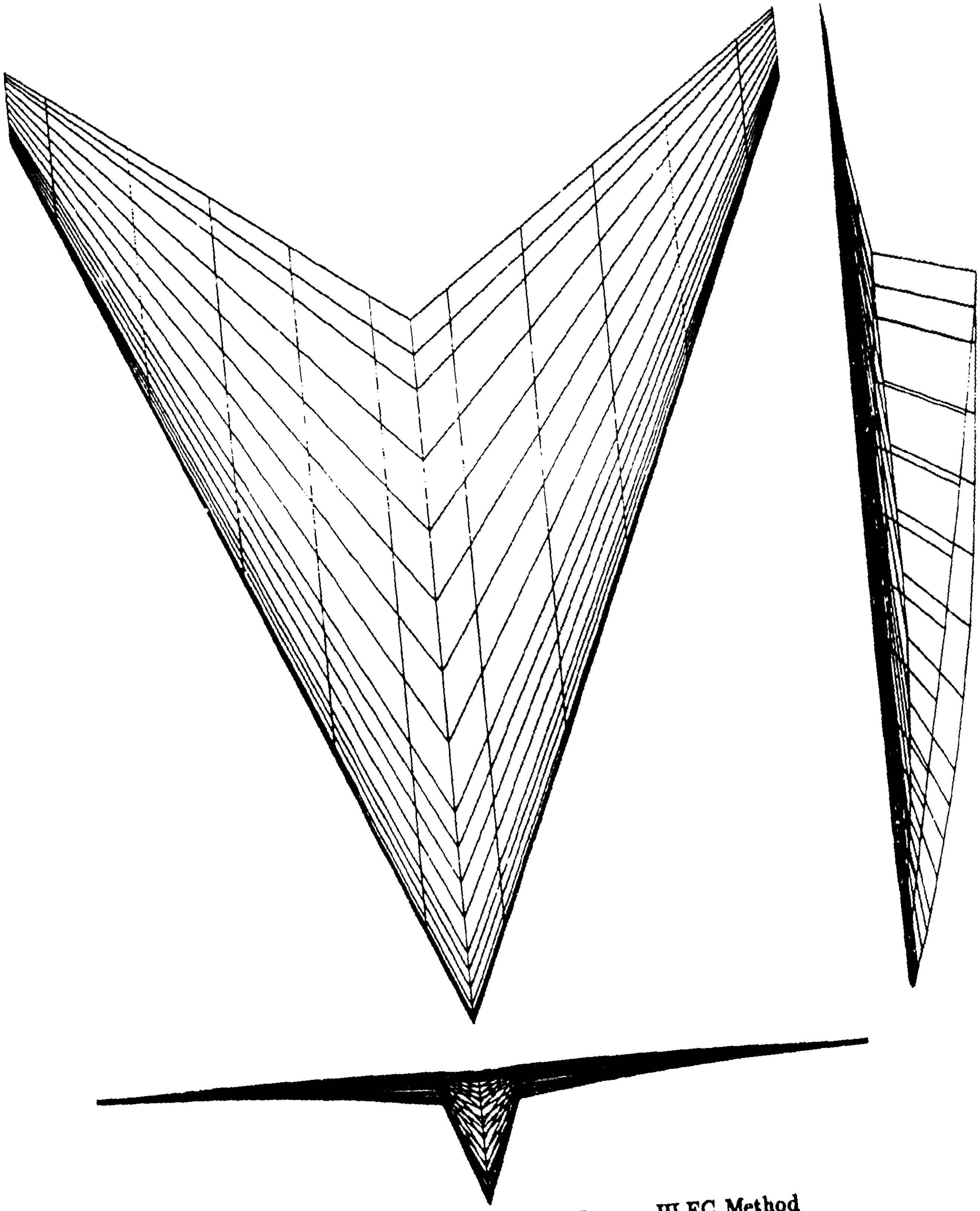

Figure 4.7 - Baseline Wing Designed by Inverse HLFC Method

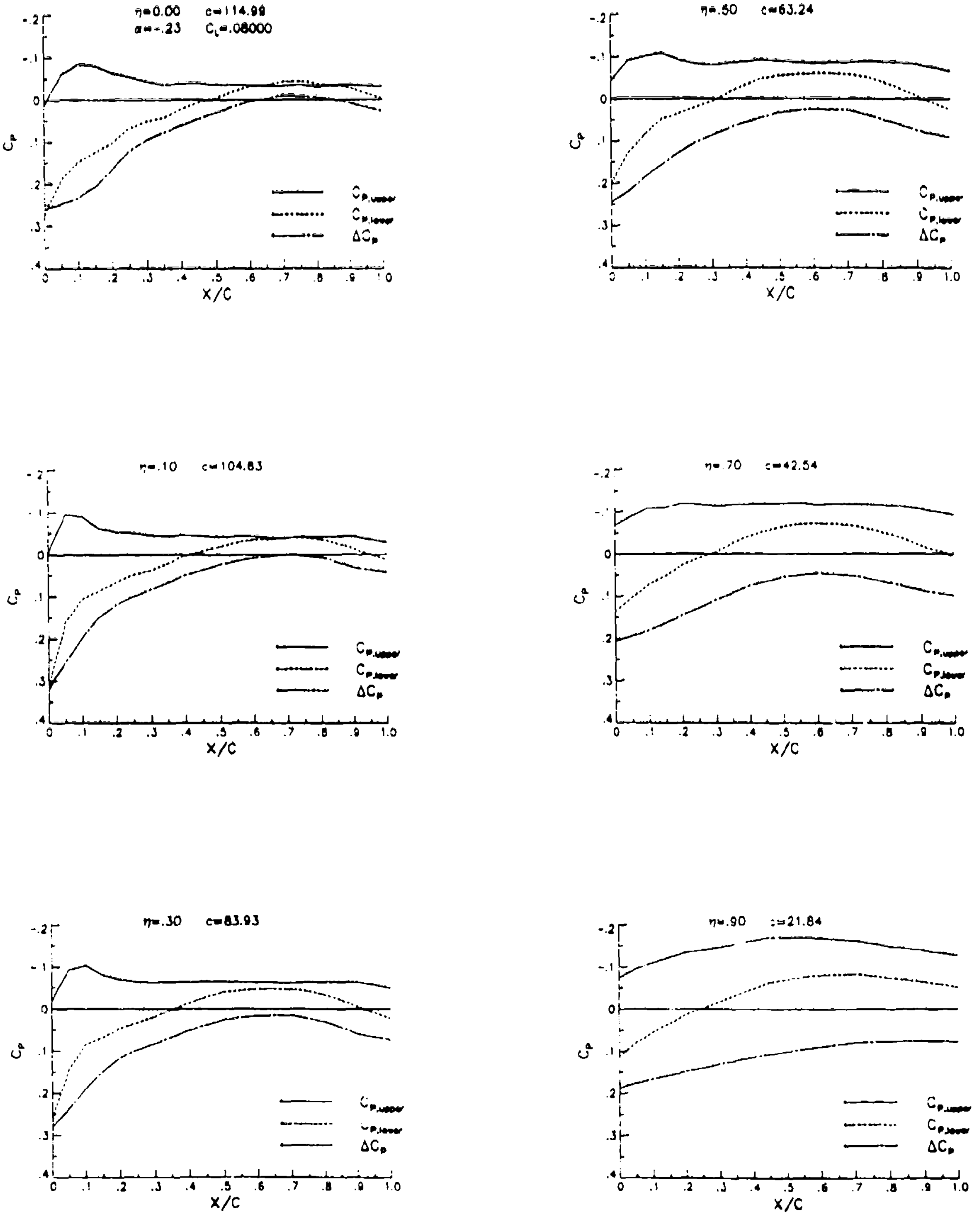

Figure 4.8 - Flat-Roof-Top Baseline Wing with Spanwise Loading Distribution Optimized

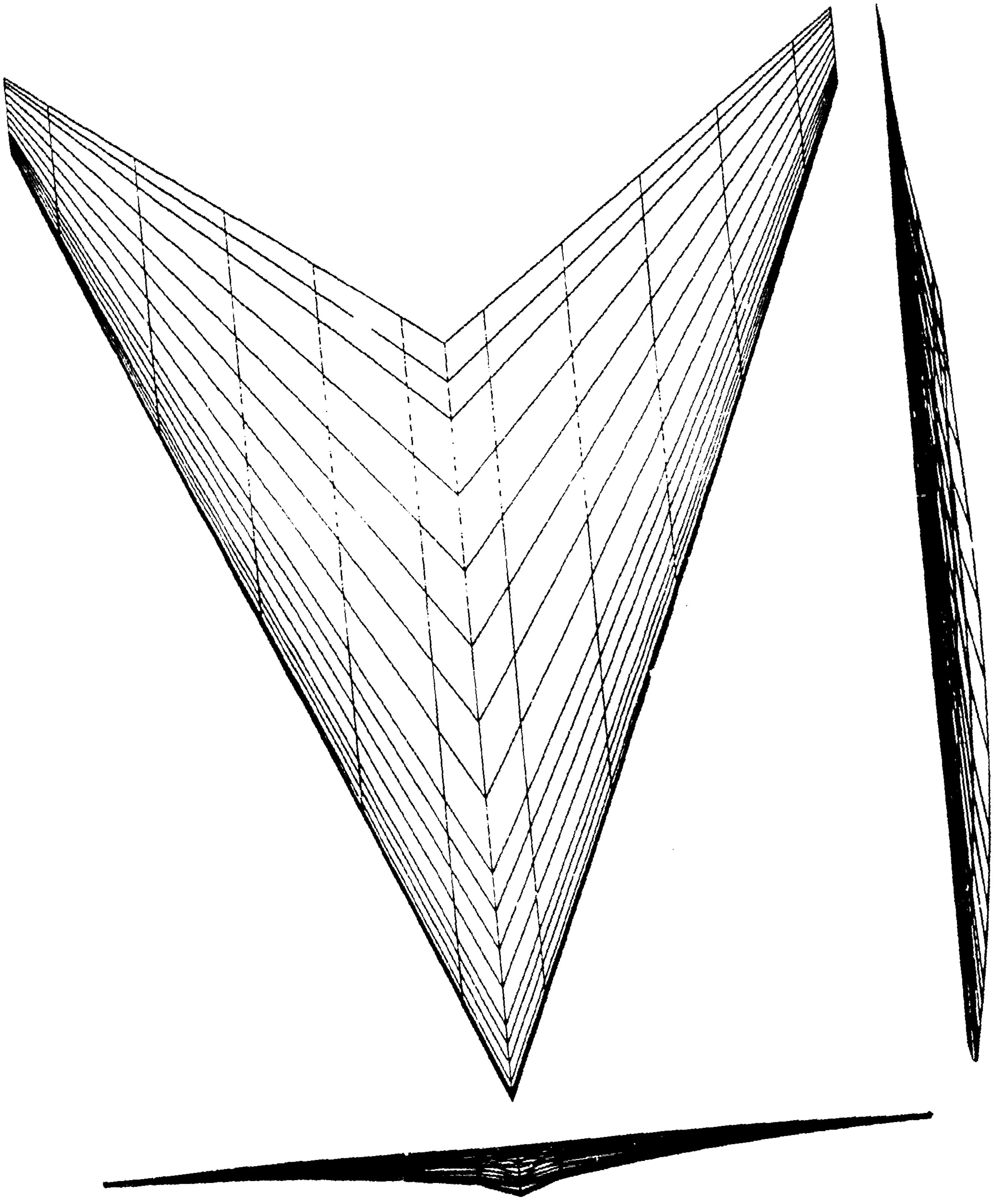

Figure 4.9 - Inverse HLFC Design of Baseline Wing After Root Modification

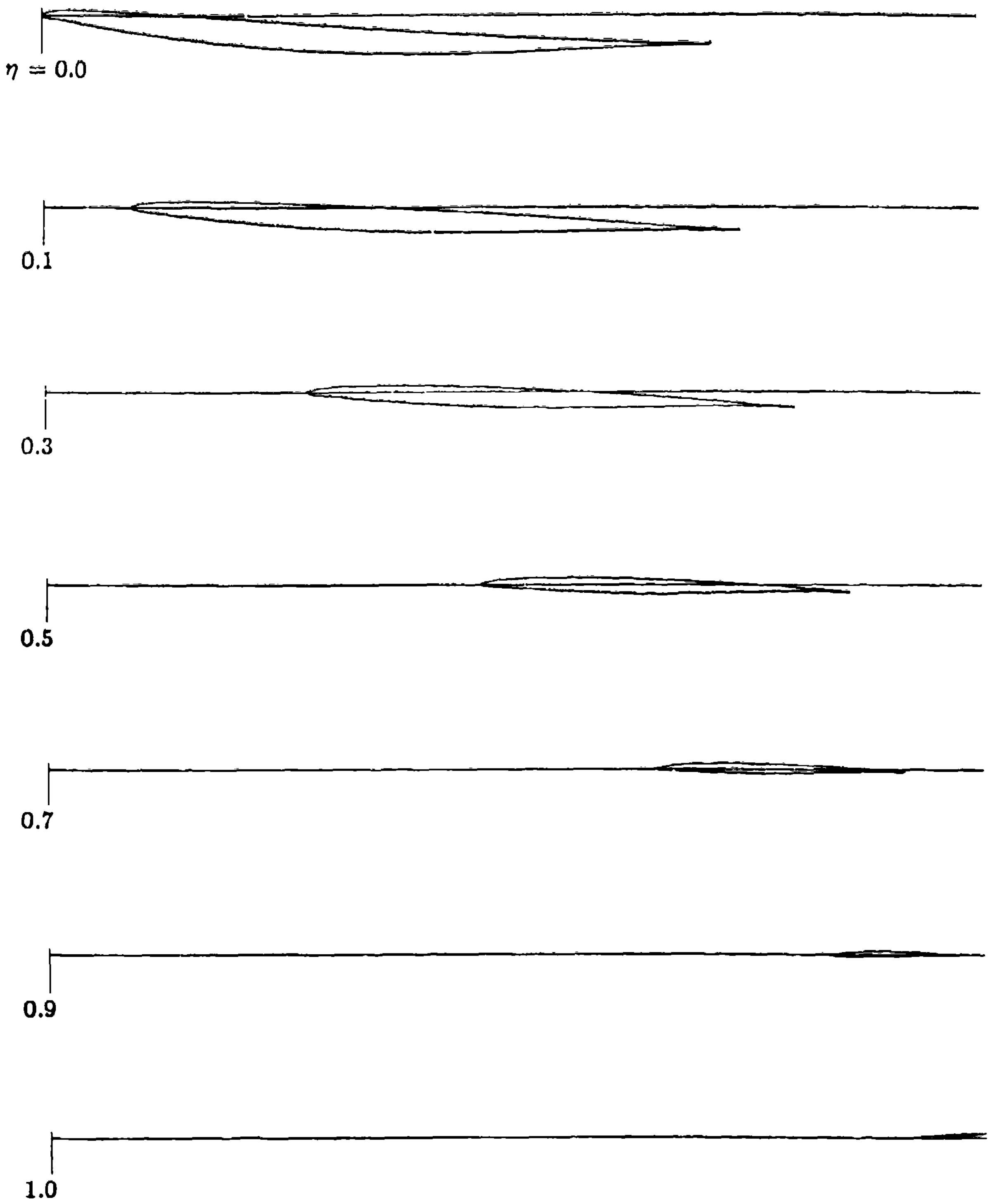

Figure 4.10 - Airfoil Sections for Baseline Inverse HLFC Design

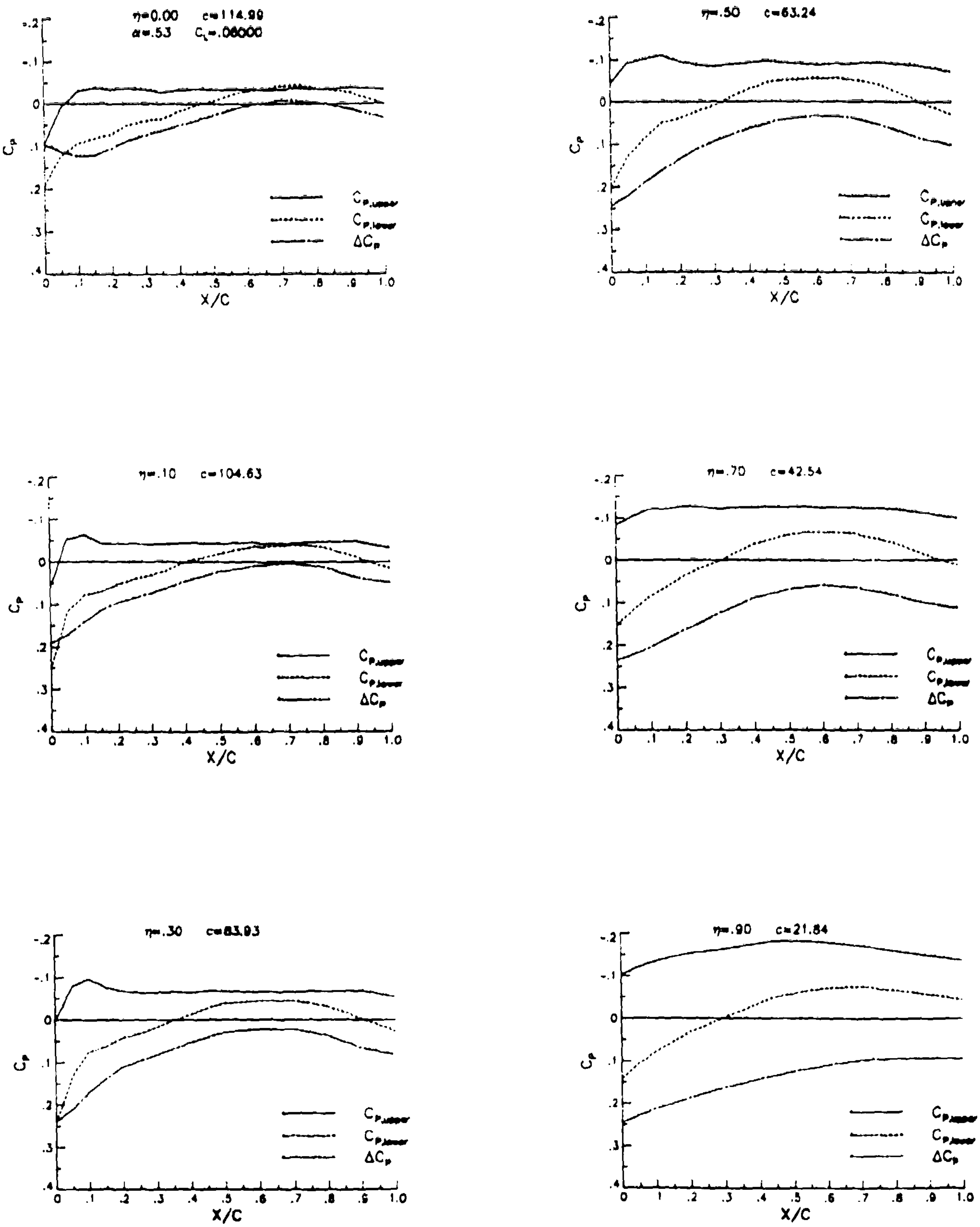

Figure 4.11 - Pressure Distribution on Baseline HLFC Wing with Root Section Rotated

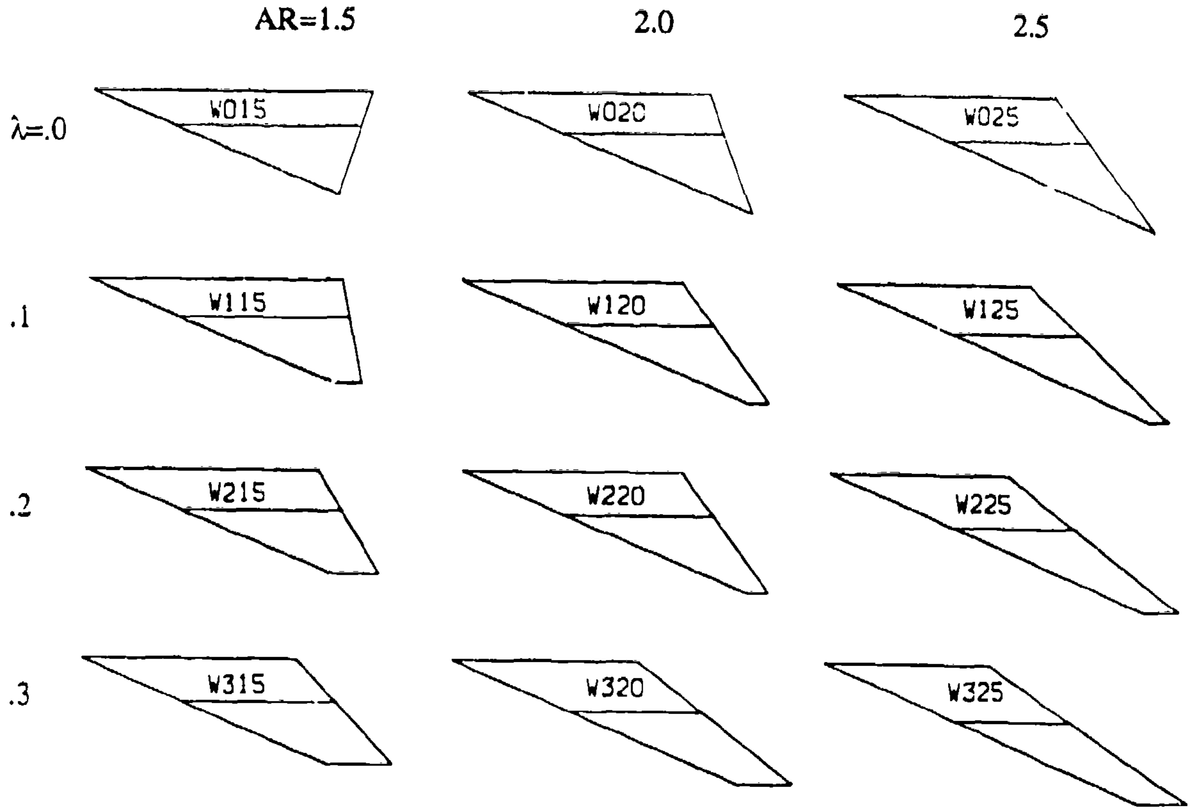

Figure 5.1 - Set of Planforms Used in Parametric Study

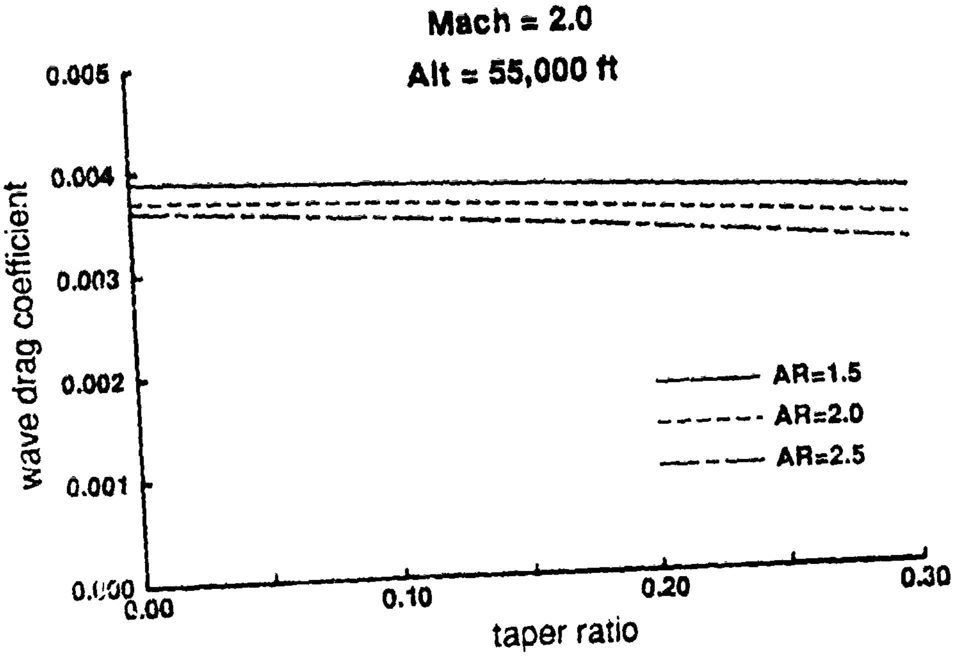

Figure 5.2 - Effect of AR and taper ratio on Near-Field Wave Drag at Cruise

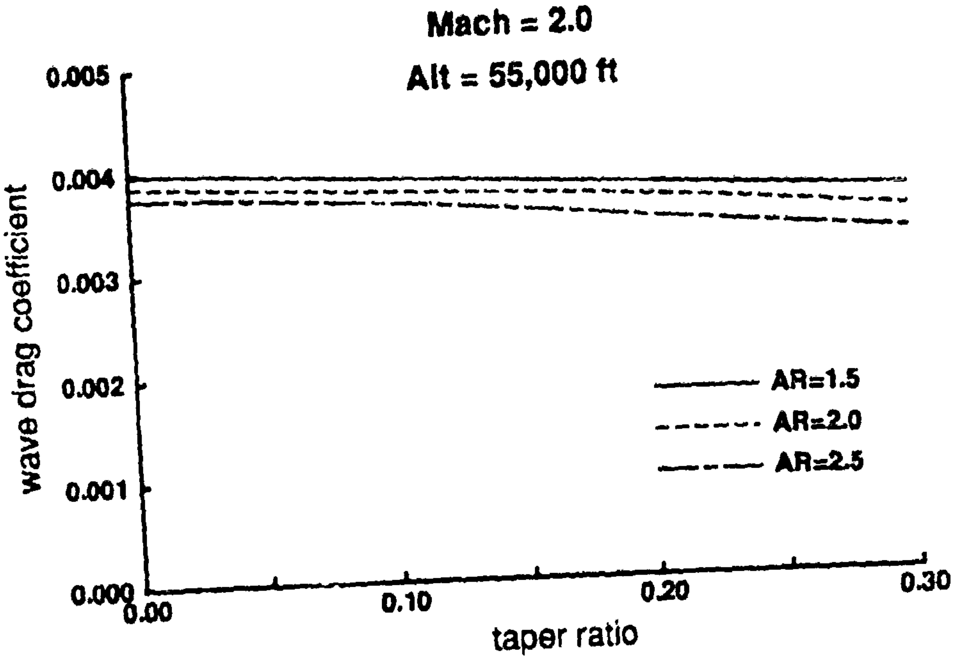

Figure 5.3 - Effect of AR and taper ratio on Far-Field Wave Drag at Cruise

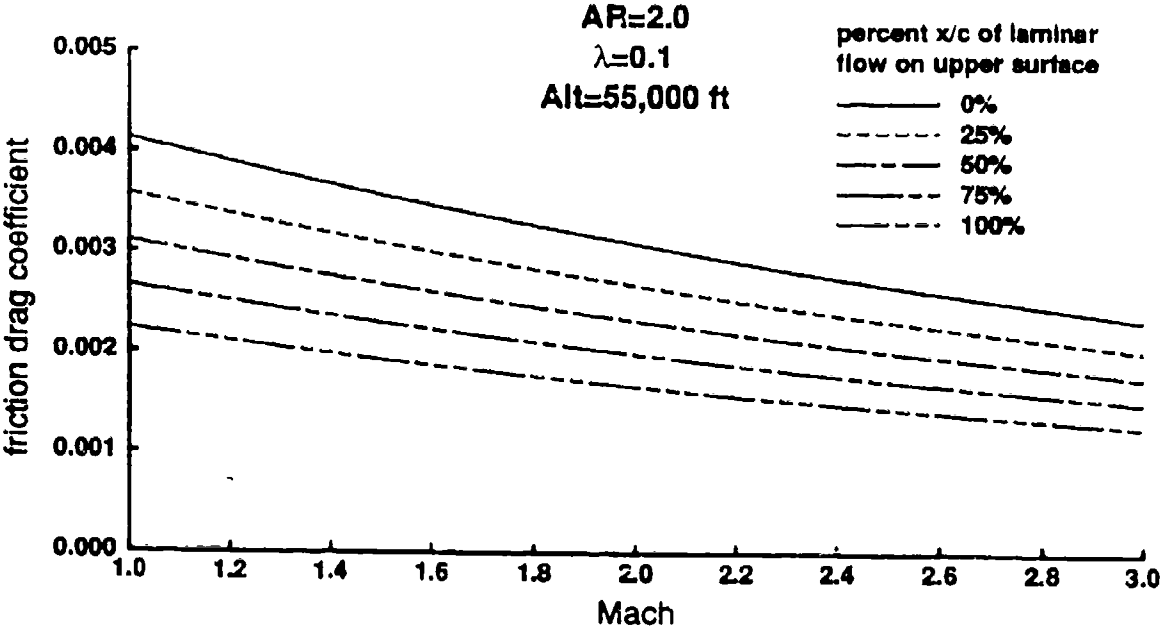

Figure 5.4 - Effect of Laminar Flow on Friction Drag of Baseline Wing

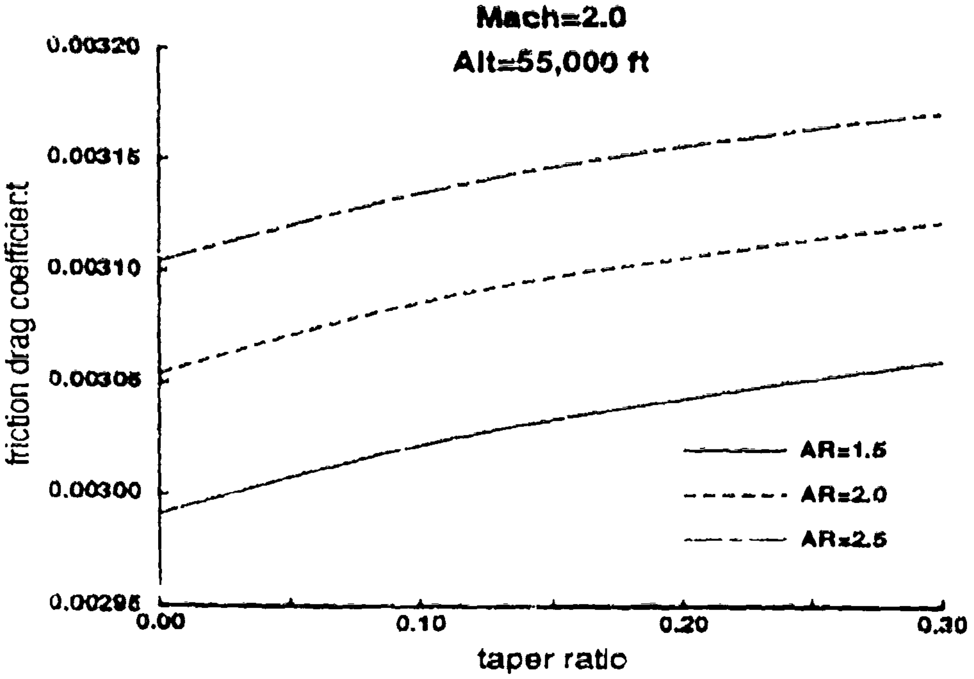

Figure 5.5 - Effect of AR and taper ratio on Skin Friction Drag of Fully Turbulent Wing

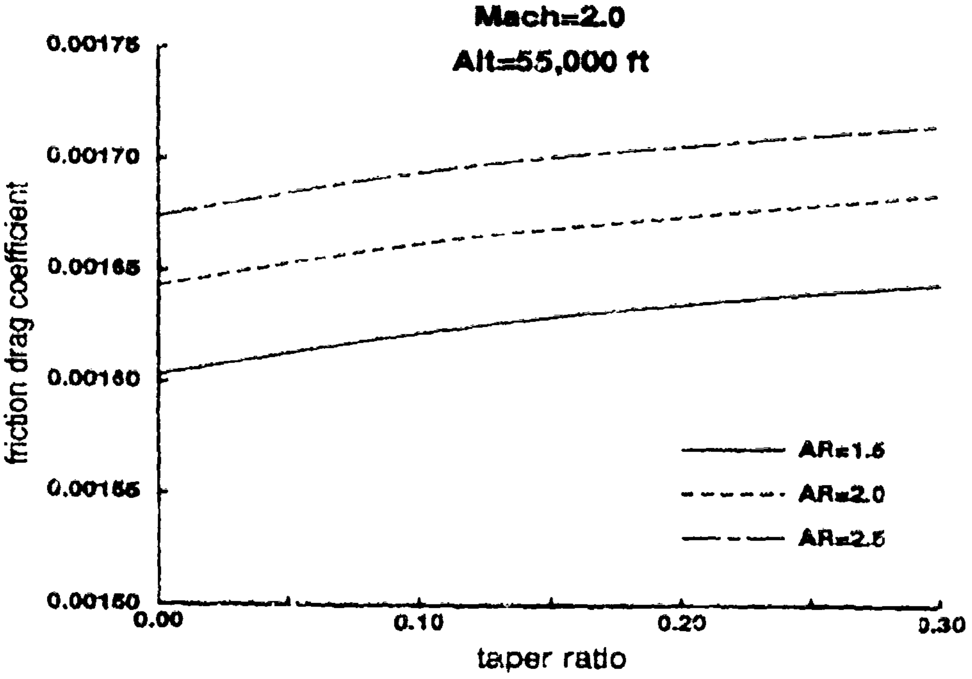

Figure 5.6 - Effect of AR and taper ratio on Skin Frictione Drag of Fully Laminar Wing

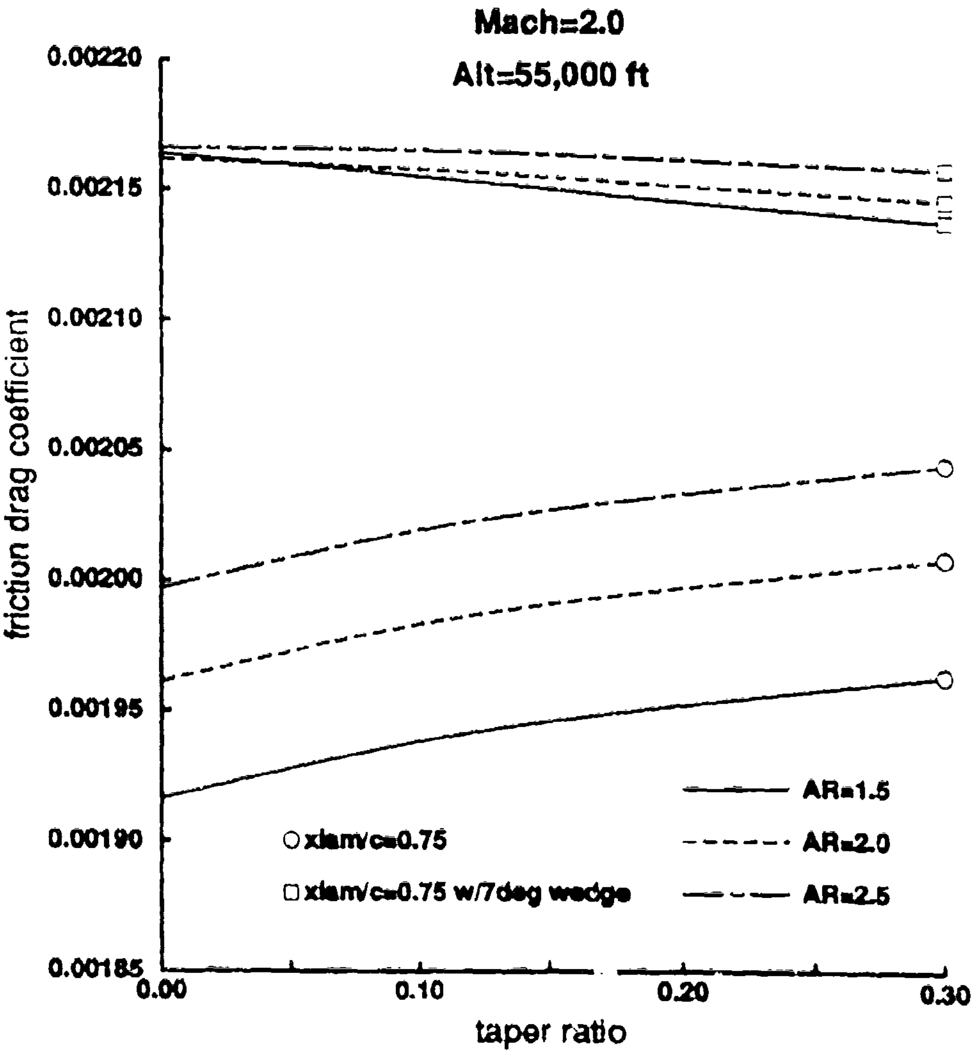

Figure 5.7 - Effect of Turbulent Wedge at Root on Friction Drag

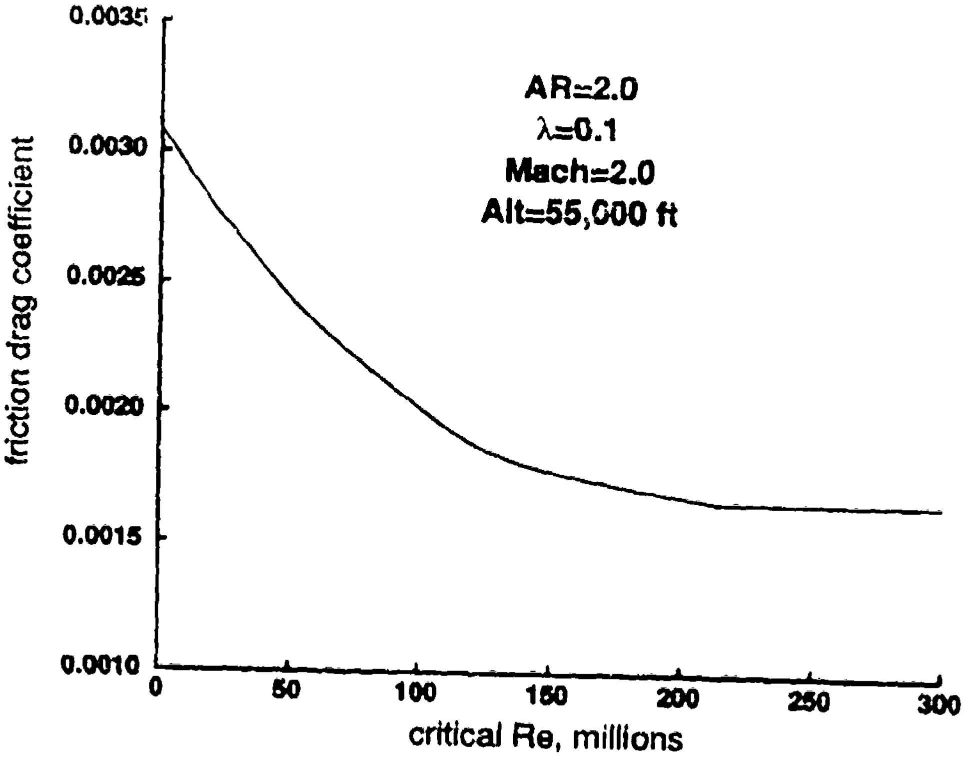

Figure 5.8 - Effect of Critical Reynolds Number on Friction Drag of Baseline Wing

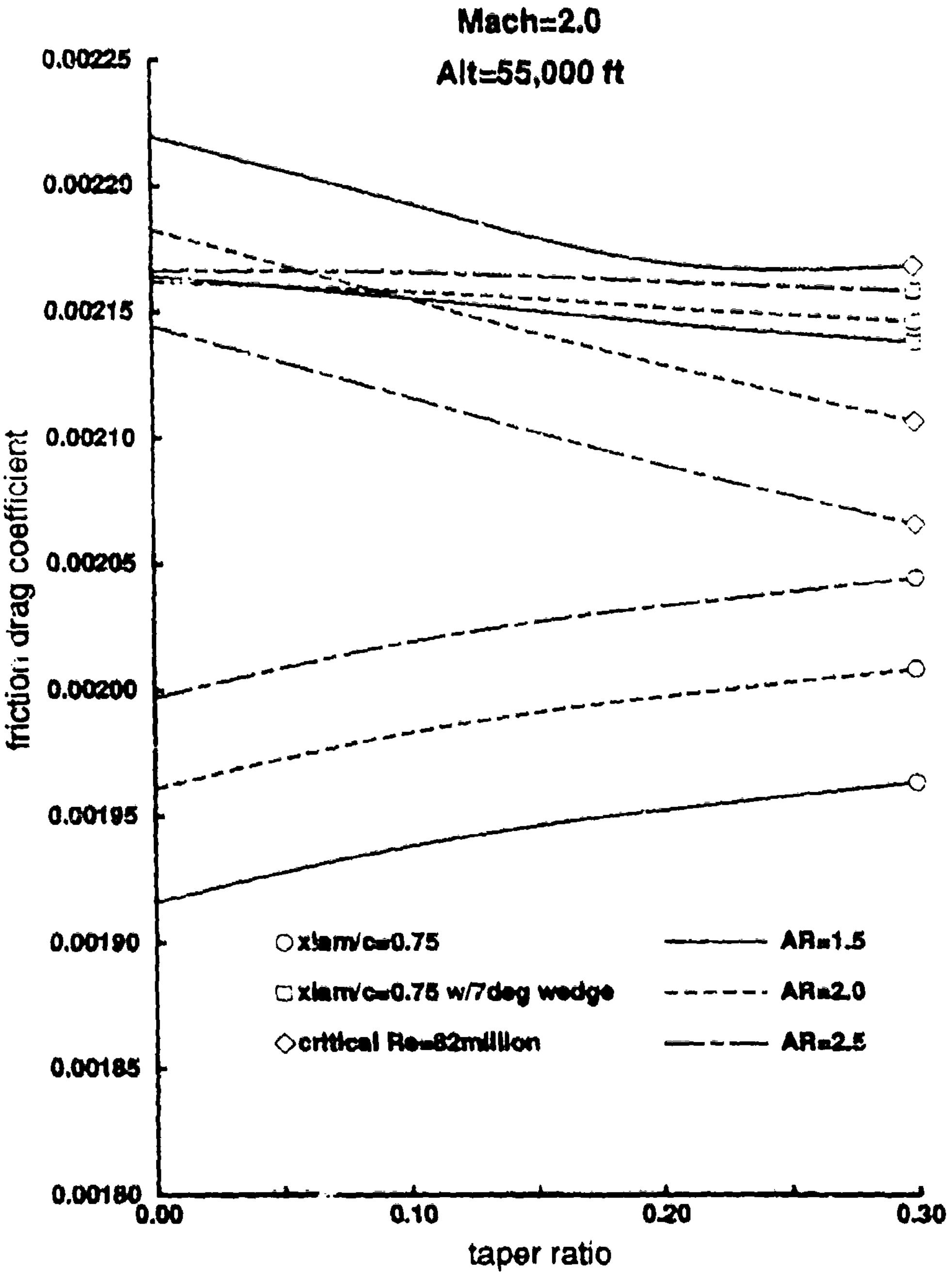

Figure 5.9 - Effect of Critical Reynolds Number Assumption on Calculated Skin Friction Drag

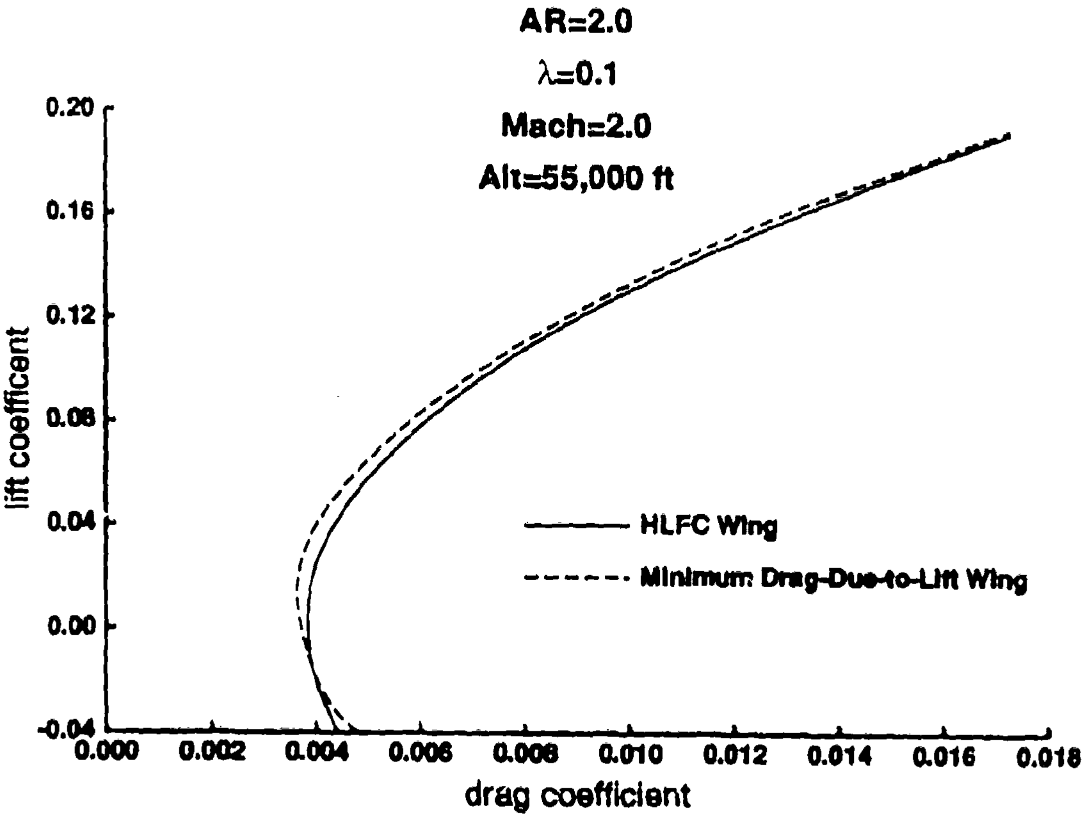

Figure 5.10 - Near-Field Wave Drag Plus Drag-Due-to-Lift on Baseline Planform

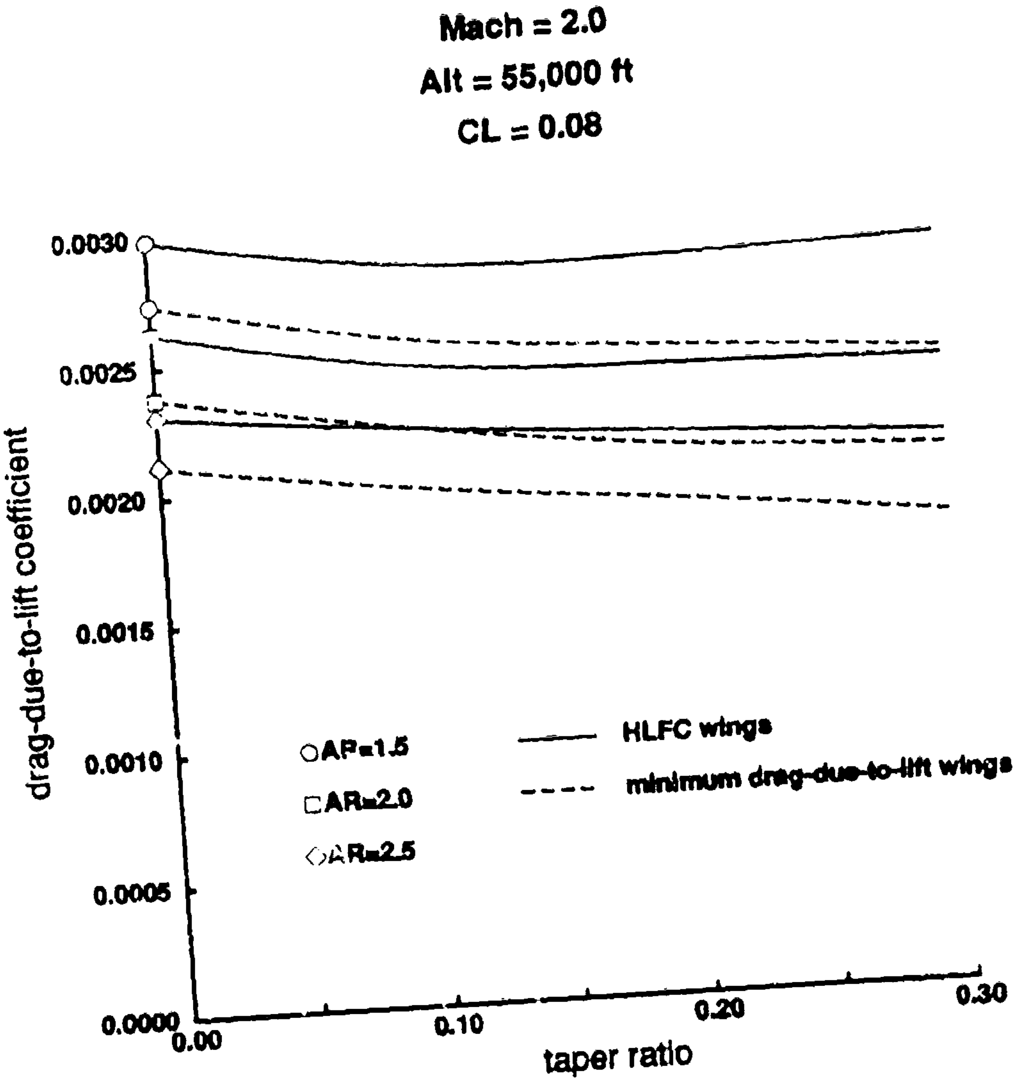

Figure 5.11 - Cruise Drag-Due-to-Lift of Parametric Wings

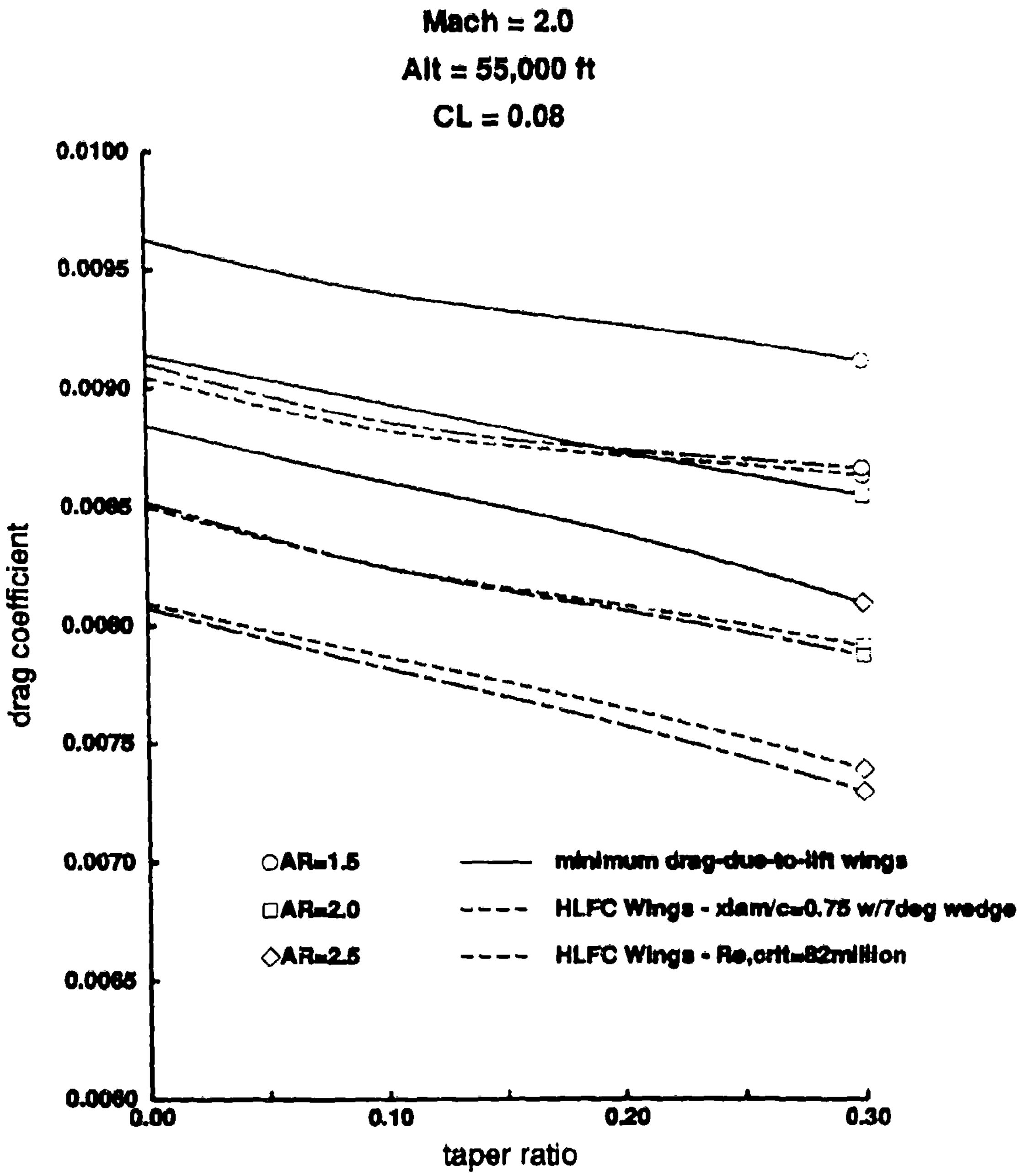

Figure 5.12 - Total Drag of Parametric Wings

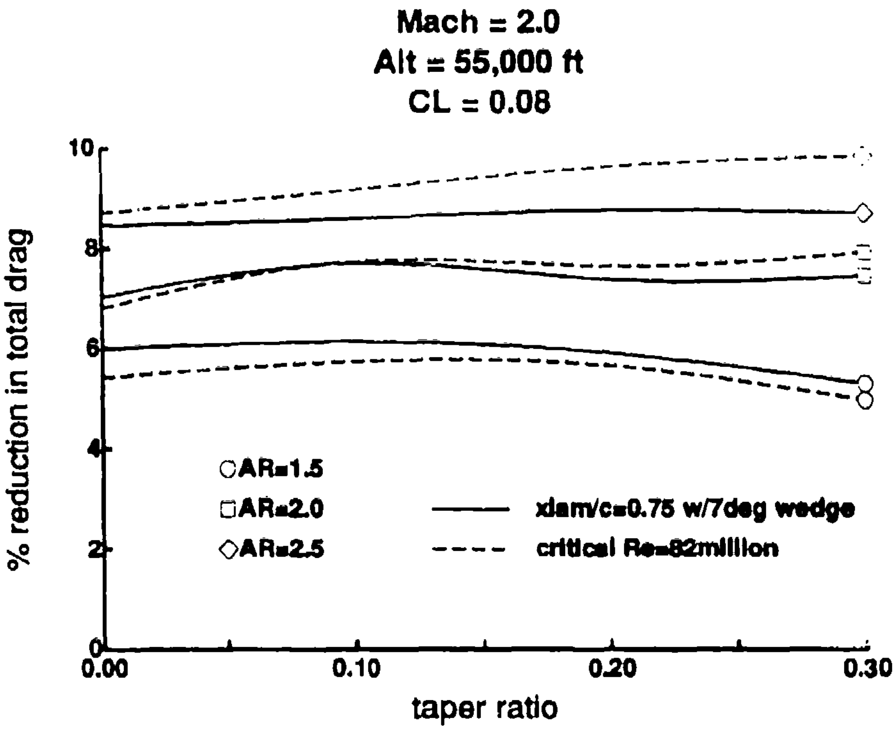

Figure 5.13 - Total Drag Benefit of HLFC Wings